Brian Patton

Non-linear Optical Spectroscopy of Single Quantum Dots

Non-linear Optical Spectroscopy of Single Quantum Dots

Thesis presented to the Institute of Physics of the University of Dortmund, Germany
in partial fulfilment of the requirements for the degree of Doctor rer. nat.

presented by

Brian Patton

Dortmund 2004

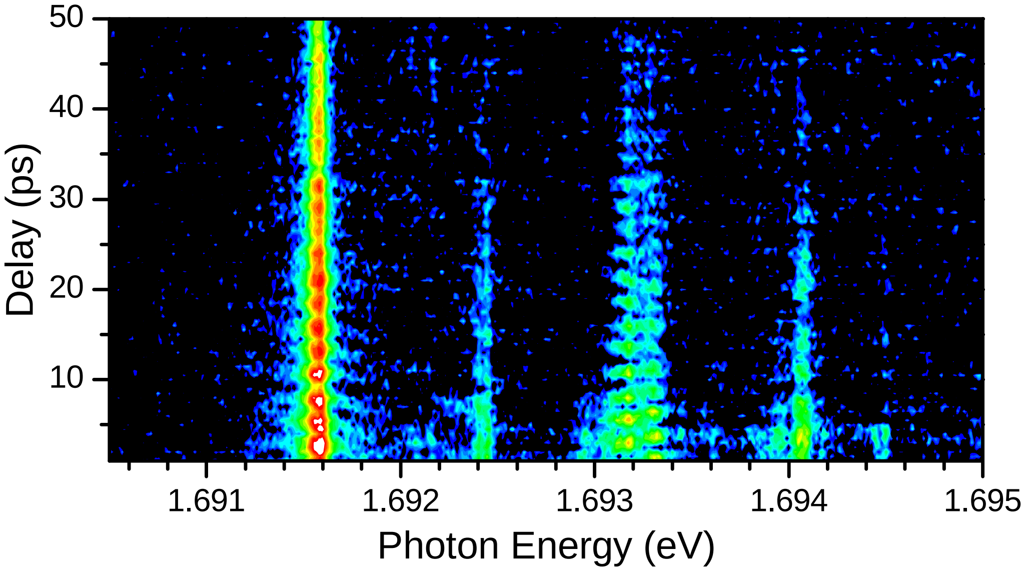

Accepted by the faculty of the Institute of Physics at the University of Dortmund,
Germany

Date of oral exam: 12th of November 2004

Board of examiners:
Prof. Dr. Ulrike Woggon
Prof. Dr. Dietmar Fröhlich
Prof. Dr. Werner Weber
PD Dr. Heinz Hövel

Contents

1 **Introduction** 1

I **Semiconductors and Quantum-Confined Carriers** 5

2 **Semiconductors** 6

2.1 Excitons 8

2.2 Heterostructures 10

2.3 Dots and confined excitonic states 12

2.3.1 Self-assembled quantum dots 13

2.3.2 Excitonic confinement through interface disorder 13

II **Non-Coherent Spectroscopy of Single Dots** 16

3 **Micro-Photoluminescence from Single Dots** 17

3.1 Experimental techniques and apparatus 17

3.1.1 High-resolution detection with the IRIS spectrometer 19

3.2 Mesa-etched CdSe/ZnSe sample 20

3.3 Identifying single dots: spectral wandering 21

3.4 Anisotropy in the dots: polarised emission 23

3.5 Time-resolved photoluminescence 27

3.5.1 Temperature dependent photoluminescence of excitons 30

3.6 Non-Lorentzian emission lineshape 32

III Coherent Spectroscopy of Single Excitonic States 41

4 Heterodyne Four-Wave Mixing: Theory and Experimental Details 42

4.1 Theory . . . 42

4.1.1 Optical Bloch equations . . . 42

4.1.2 Vector model of the Bloch equations . . . 46

4.1.3 Heterodyne four-wave mixing . . . 48

4.1.4 Signal to noise ratio . . . 48

4.2 Experimental setup . . . 49

4.2.1 The acousto-optical modulator . . . 49

4.2.2 Beam preparation . . . 51

4.2.3 Coupling to sample and collection of signal . . . 52

4.2.4 Imaging and spectral interferometry at the AOM . . . 54

4.2.5 Signal detection . . . 59

4.2.6 Data pre-processing . . . 60

4.2.7 Phase-correction . . . 62

5 Heterodyne Four-Wave Mixing: Experimental Results 67

5.1 The sample under investigation . . . 67

5.2 Initial characterisation of the FWM signal . . . 69

5.3 Time-resolved FWM: Polarisation decay and photon echo . . . 72

5.4 Rabi-oscillations of single excitonic states . . . 78

5.5 Coherent coupling between excitonic states . . . 84

IV Conclusions 88

6 Summary 89

7 Outlook 92

Appendix 93

Bibliography **95**

Symbols and abbreviations **102**

Acknowledgements **107**

Chapter 1

Introduction

It is now nearly a century since Einstein's *annus mirabilis*, 1905, in which he published three seminal papers which, in many respects, could be thought to have laid the groundwork for much of 20^{th} century physics. Particularly relevant here is his paper on the photoelectric effect[Ein05], in which he uses Planck's quantisation hypothesis to explain the emission of photoelectrons from metals as being due to the intrinsic quantisation of the electromagnetic field. As we know now, this led to the development of quantum mechanics, perhaps the crowning glory of physics in the last century. The investigation of the interaction of light with matter did not stop with this paper though and the work presented here is but one piece of research in a hugely varied field which can trace its roots to these early experiments.

Also of great importance to the work presented here is the massive amount of research performed on semiconductors in their various guises during the last century. The development of the transistor in Bell Labs in 1947 promoted the investigation of semiconductors as electronic devices, while the developments in semiconductor lasers in the 1960's provided an impetus for the study of the interaction of semiconductors with an optical field.

More recently, the ability to grow extremely high-quality semiconductor *heterostructures* incorporating two or more different materials, and with control over the composition down to the sub-monolayer scale, through techniques such as molecular-beam epitaxy (MBE) and metal-organic chemical vapour deposition (MOCVD), along with advances in the ability to pattern these materials at sub-micron scales, has lead to exploration of systems with reduced dimensionality. Examples of such systems, in which there is a confinement of the charge carriers in one or more directions in length scales comparable to the De Broglie wavelength, are quantum wells and quantum dots and show an effective dimensionality of two and zero, respectively. This work focusses on the examination of the properties of quantum dots. By choosing the right growth conditions, quantum wells can spontaneously form quantum dots through processes referred to generically as self-assembly. The details of the formation usually involve a combination of enhanced interdiffusion of one species in the other and strain relaxation through the formation of features (the dots themselves) which lower the energy state of the crystal as a whole. As such, dots are characterised both by their geometry and their stoichiometric composition. Interest in the optical properties of dots arises primarily from their atom-like density of states, leading to their description as "artificial-atoms". However, the fact that the dots being investigated here consist of many (typically $> 10^4$) atoms and are embedded in a matrix of another material means that this analogy should not be taken too far. This is no bad thing, for the variety of phenomena exhibited by these structures leads to a rich array of physics to investigate. A good introductory review article on the optical properties of quantum dots may be found in Reference [Yof01] while References [Wog97, BGL99] are also worth reading, if somewhat more thorough. Part I gives a brief introduction to the physics of semiconductors and quantum confined systems.

Of particular interest, and forming the core of the work presented here, is the relaxation of the quantum dot from excited states back to the crystal ground state. The dynamics governing such processes are given by timescales ranging from $10^{-15}\,s$ to $10^{-9}\,s$, thus requiring ultrafast spectroscopic techniques. Such techniques are often limited in temporal resolution to the pulse duration of the excitation and the development of lasers with pulse lengths of a few optical cycles has allowed access to the femtosecond regime.

Part II details the investigations into the non-coherent spectroscopy of single quantum dots performed during the course of my PhD. In these experiments the charge-carriers were excited non-resonantly at energies above the dot levels. Subsequent trapping by the dot and relaxation to the ground-state in the dot (distinct from the *crystal ground state*), primarily through phonon-mediated processes, leads to a loss of phase-coherence between the excitation field and the optically-excited carriers. However, such spectroscopy still represents a powerful tool to obtain insight into both the structure of the energy levels within the dots and into the processes wherein the recombination of an electron-hole pair results in the emission of a photon. The techniques described here include both spectrally and temporally resolved measurements. It is worth noting that, through the Fourier transform from the time-domain to the frequency-domain and vice-versa, it is possible to obtain energy-level spacings from time-resolved data and information on the dynamics of the system from the spectrally-resolved emission. An example of this is given in Section 3.6, where analysis of the lineshape of the emission leads to insight into the dynamics of the recombination.

The loss of coherence with the excitation field, referred to as *dephasing*, has taken on a particular importance since the realisation that the simulation of quantum systems is imperfect in a Turing machine, but requires the use of a machine that is itself quantum-mechanical in nature[Fey82]; a quantum-computer. The power of such a machine comes from the superposition principle of quantum mechanics; processes that destroy this superposition or, from the point of view of obtaining a correct answer in a calculation, perturb the system in an adverse way are referred to as providing a source of *decoherence*. Reference [PSE96] provides an interesting introduction to the role of decoherence in quantum-information processing. If we were to use quantum dots as components in a quantum computer the dephasing mentioned above would be a prime source of decoherence. Part III details the manner in which the technique of *four-wave mixing* (FWM) was applied to the investigation of dephasing in quantum dots. As performed on ensembles, FWM often assumes that the ensemble can be approximated as consisting of multiple, non-interacting two-level systems, an approach first applied to the theoretical modelling of masers[FVH57], the microwave equivalent of lasers. Rather than measure the properties of an ensemble, a novel technique has been developed which combines high spatial-resolution with a heterodyne detection method to enable the FWM signal from both small ensembles and even individual quantum dots be measured. The build-up of a phenomenon known as the *photon-echo*, an ensemble effect, could then be measured as a function of ensemble size. A further advantage of this method is that it uses spectral interferometry of the signal with a reference pulse to recover the full FWM signal in both amplitude and phase. The measurement of the phase, in particular, opens up a number of options when analysing the data. The evolution of the system state with increasing pulse area (a quantity proportional to the square root of the time-integrated intensity per pulse) shows Rabi oscillations of single excitonic states. Finally, a method to determine the coherent coupling between different states is developed. Since any practical quantum computer will require more than one *qubit* (the quantum equivalent of a bit in classical computing) and these qubits will need to be linked in some manner, an understanding of coherent coupling is of particular importance.

Part I

Semiconductors and Quantum-Confined Carriers

Chapter 2

Semiconductors

This chapter provides a brief introduction to some of the concepts which are essential to the work described in this thesis. However, any details of theory which are specific to the experiments I performed will be either recounted or introduced at the relevant section of the thesis and so readers familiar with semiconductor physics may safely skip this chapter and continue to Part II of the thesis.

The periodicity of the underlying lattice of atoms in a solid state material leads to solutions of the Schrödinger equation which describe bands in the electronic structure of the material which, in reciprocal, or **k**-space, are equivalent for points separated by a reciprocal lattice vector. The classification of the material as metal, semiconductor or insulator is tied directly to the band structure. For metals, the energetically highest band is either partially filled or overlaps in **k**-space with other, unfilled bands. In contrast, both semiconductors and insulators have a fully-filled band, called the *valence* band, as their highest occupied band. The valence band is separated from the next band, the *conduction* band, by an energy gap, E_g. It is the size of this gap that determines the classification of the material as a semiconductor or an insulator. However, there is no hard-and-fast rule, leading to cases like diamond, with $E_g = 5.48\,eV$, being classed as a semiconductor (compare to silicon, $E_g = 1.12\,eV$). A further classification of semiconductors is possible depending on the position of the valence band maximum and the conduction band minimum. In the case where both occur at the same point in **k**-space, the semiconductor is referred to as a direct-gap material. Conversely, indirect gap materials have an offset in the position of the extrema. To good approximation, transitions involving photons can be considered vertical in the **k**-space-energy (x,y) picture while phonon-induced transitions are horizontal. Thus, for optical applications (and, naturally, investigation) direct-gap semiconductors are preferable since no phonon is required for transitions resonant to E_g.

Both materials investigated in this thesis, GaAs and CdSe, are direct gap materials. GaAs crystallises in the zinc-blende structure, while CdSe can be found in both the zinc-blende and wurzite forms. Figure 2.1 shows both the crystal structure and the first Brillouin zone for both of these crystal types. Both structures have atoms bonded to

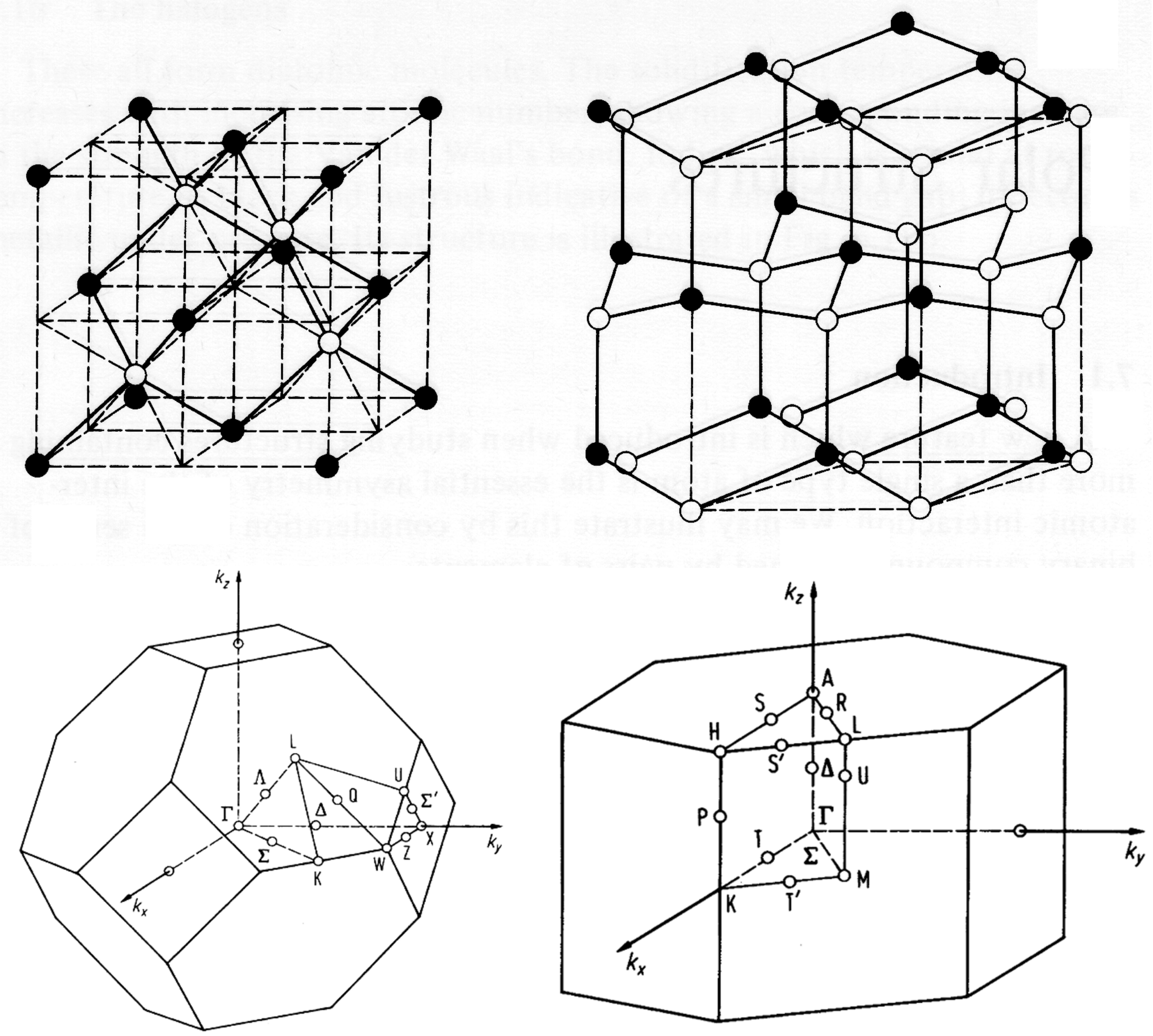

Figure 2.1: *Top: The structure of zinc-blende(left) and wurzite(right) materials[BF73] Bottom: The first Brillouin zone for each crystal type.*

their neighbours in a tetrahedral structure, the difference between the two stems from a rotation of one of the bonds so that the layering in zinc-blende may be described as ABCABC, whereas that of wurzite is ABAB. In both GaAS and CdSe, the bonds are formed through sp^3-hybridisation with the resulting band structure being such that the conduction band at the centre of the Brillouin zone (about the Γ-point) is dominantly formed by the 4s(5s) orbital of gallium(cadmium) and the valence band by the 4p orbital of arsenic(selenium). At higher values of $|\mathbf{k}|$ the mixing is more complex and the simple picture described above no longer holds true. Figure 2.2 shows the calculated bandstructure for both of these materials. The spin, $\mathbf{S}$, and orbital angular momentum, $\mathbf{L}$, through the spin-orbit coupling, give rise to important features of the bandstructure about $\Gamma = 0$. The important quantity here is the total angular momentum, $\mathbf{J} = \mathbf{L} + \mathbf{S}$, and its projection in the z-direction, j_z. The conduction-band has $\mathbf{J} = 1/2$ and is doubly degenerate in both wurtzite and zinc-blende crystals. In zinc-blende crystals

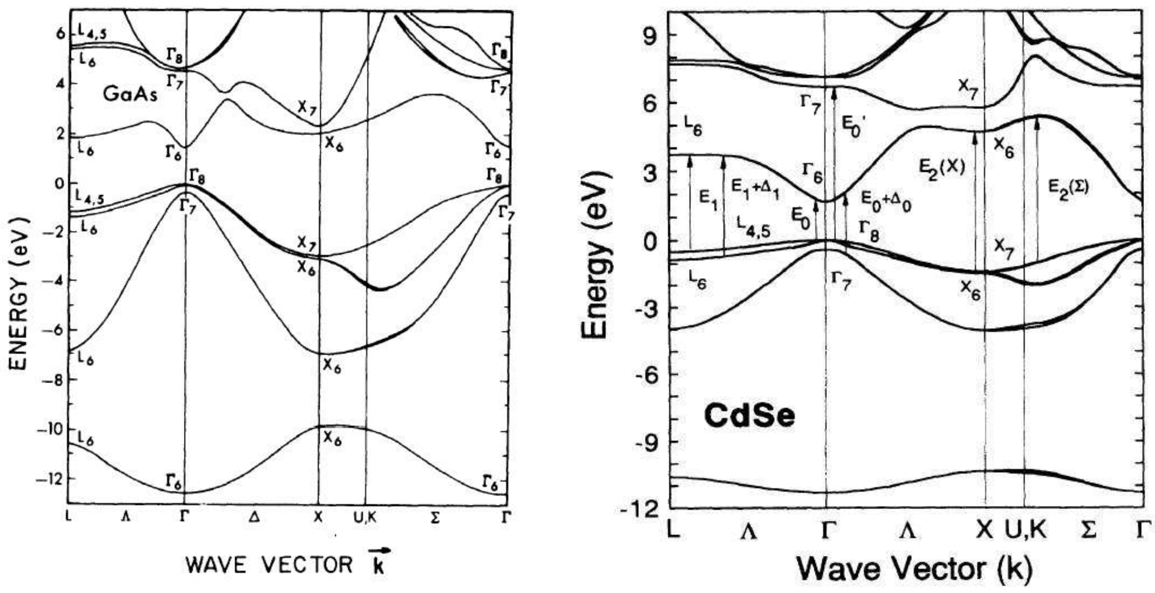

Figure 2.2: *The band-structures of the two materials investigated in this work as calculated by the nonlocal empirical pseudopotential method. Left: GaAs[CC76] Right: Zinc-blende CdSe[KKR+94]*

the sixfold degeneracy of the valence band results in two bands with $J = 3/2$ that are both doubly degenerate and which are themselves degenerate at $\Gamma = 0$. Since they have different dispersions, they are referred to as the 'light' and 'heavy' bands. The third band, with $J = 1/2$ is known as the split-off band and is lower in energy by the split-off energy, $\Delta = 341\,meV$ in GaAs and $\Delta = 420\,meV$ in CdSe. This band can thus be ignored in most optical experiments. Figure 2.3 shows the conduction and valence bands for both zinc-blende and wurzite structures. The valence band in wurzite crystals is comprised of three bands - an additional crystal-field splitting leading to the two upper valence bands being no longer degenerate but forming two bands, the higher energy being of Γ_9 symmetry and the other of Γ_7. The split-off band also has Γ_7 symmetry. These three bands are then referred to as the 'A-', 'B-' and 'C-'band respectively. In agreement with Reference [GWL+99], which found that CdSe quantum dots of the type investigated in this work could be modelled accurately as being of zinc-blende structure, and also with Reference [KKR+94] which showed that $Zn_xCd_{1-x}Se$ structures grown by MBE on GaAs substrates showed zinc-blende structures over the whole range from ZnSe to CdSe, I will only consider bandstructures of the zinc-blende type from now on.

2.1 Excitons

Excitation of an electron to the conduction band will leave an empty state in the valence band. The energy-momentum relationship gives an effective electron mass in the conduction band of $m_e = 0.067m_0$ for GaAs and $m_e = 0.13m_0$ for CdSe, where

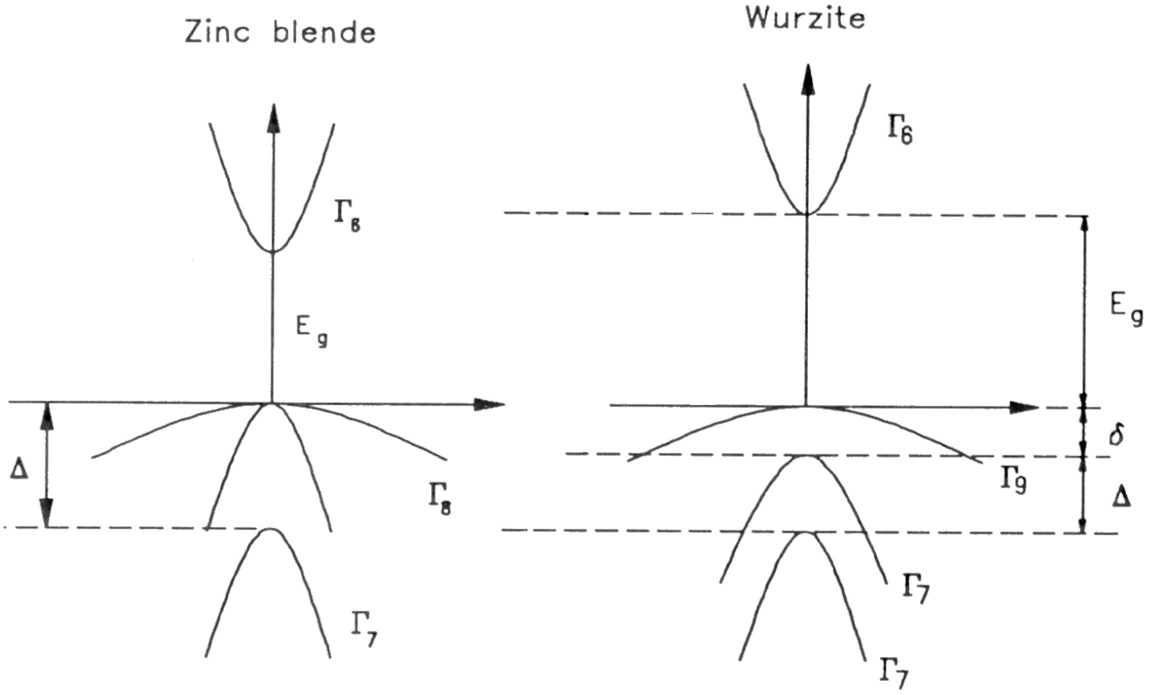

Figure 2.3: *Schematic band structure near* $\mathbf{k} = 0$ *for Left: a zinc-blende structure with spin-orbit coupling and Right: a wurzite structure with additional splitting,* δ*, of the upper-valence band due to the crystal field. (From Ref. [PKM93])*

m_0 is the free electron mass. In the valence band, the empty state can be treated as a quasi-particle of positive charge called a *hole*. Treating the kinetic energy of the hole as a negative quantity and assuming parabolicity of the bands, the effective mass of the hole is given by a reciprocal relationship to the band curvature. The labelling of the two degenerate bands as 'heavy' and 'light' is now apparent: the heavy-hole has $m_{hh}(\Gamma, 50K) = 0.475m_0$ in GaAs and $m_{hh}(\Gamma, 1.8K) = 0.45m_0$ in CdSe while the light hole has $m_{lh}(\Gamma, 50K) = 0.087m_0$ in GaAs and $m_{lh}(\Gamma, 1.8K) = 0.145m_0$ in CdSe. A Coulomb interaction between the electron and hole can lead to a bound state whereby one particle orbits the other. Since the resulting interaction lowers the energy of the combined pair, such bound states are to be found at energies beneath the conduction band and are known as *excitonic* states. To calculate the energy of an exciton state, consider the (simple) case of an electron and hole of mass m_e and m_h moving against a uniform background material of dielectric constant ϵ. By analogy to the Rydberg series, which gives the energy levels for a simple H atom, we get

$$E_{Ex} = E_g - \frac{\mu e^4}{2(4\pi\epsilon\epsilon_0\hbar)^2}\frac{1}{n^2} \tag{2.1}$$

where n is an integer and $\frac{1}{\mu} = \frac{1}{m_e} + \frac{1}{m_h}$ is the reduced mass. The radius of the exciton is given by

$$< r >_n = \frac{m_0}{\mu}\epsilon a_0 n^2 \tag{2.2}$$

where a_0 is the 1^{st} Bohr orbit of the H atom (= 0.529 Å). In CdSe $< r >_1 = 54$ Åwhile in GaAs $< r >_1 \approx 200$ Å, which, when compared to the lattice-constants $a_{CdSe} = 6.05$ Å and $a_{GaAs} = 5.65$ Å, shows that the original assumption of a uniform background is justified. Such weakly bound, and therefore large, excitons are known as *Mott-Wannier* excitons. As the quantity $< r >$ is itself derived from the Bohr radius, I will refer to it from now on as a_B, the excitonic Bohr radius.

2.2 Heterostructures

Control of the bandstructure can be achieved through the growth of alternate layers of two semiconductors. Figure 2.4 shows the value of two important parameters, the lattice constant and the bandgap, for a variety of Group IV, III-V and II-VI semiconductors. Appropriate choice of the two semiconductors in such *heterostructures* can drastically change the properties of the resulting material: growing a thin layer of material (the well) with a bandgap smaller than that of the surrounding material (the barrier) will result in the confinement of carriers to this inner layer. If the thickness of the well is comparable to the deBroglie wavelength of the carriers then quantisation effects come in to play in the growth-direction and the well can be considered to be effectively two-dimensional. Further reduction in the dimensionality can be achieved, for example, through the patterning of the material so that the carriers are also confined in one of the lateral dimensions. Such a *quantum wire* is an example of a one-dimensional system. Quantum wires will not be discussed further in this work. Confinement in both lateral directions as well as the growth direction results in a zero-dimensional structure known as a quantum dot. The next section will discuss the ways in which the quantum dots investigated in this work were formed. First, though, it is worth looking at some of the ways in which the reduced dimensionality affects particles within such structures. For all following discussion I will assign the growth direction to the z-direction.

First, consider the joint density of states(DOS), $D(E)$ for different dimensionalities. The DOS gives the number of states in the interval $E \rightarrow E + dE$ and, assuming a parabolic band dispersion and infinite potential barriers, is given by[Sug99]

$$D_{3D}(E) = \frac{1}{2\pi^2}\left(\frac{2m^*}{\hbar^2}\right)^{3/2} E^{1/2} \tag{2.3}$$

$$D_{2D}(E) = \frac{m^*}{\pi\hbar^2 L_z}\sum_{n_z}\Theta(E - E_{n_z}) \tag{2.4}$$

$$D_{0D}(E) = 2N_D \sum_{n_x,n_y,n_z} \delta(E - E_{n_x} - E_{n_y} - E_{n_z}) \tag{2.5}$$

where m^* is the effective mass of the particle, $\Theta(E)$ is the Heaviside step function, $L_{x,y,z}$ and $n_{x,y,z}$ give the characteristic size of the confinement potential and the (integer) quantum number in the appropriate direction, and we have introduced N_D as the volume density of quantum dots. Figure 2.5 shows the resulting density of states for

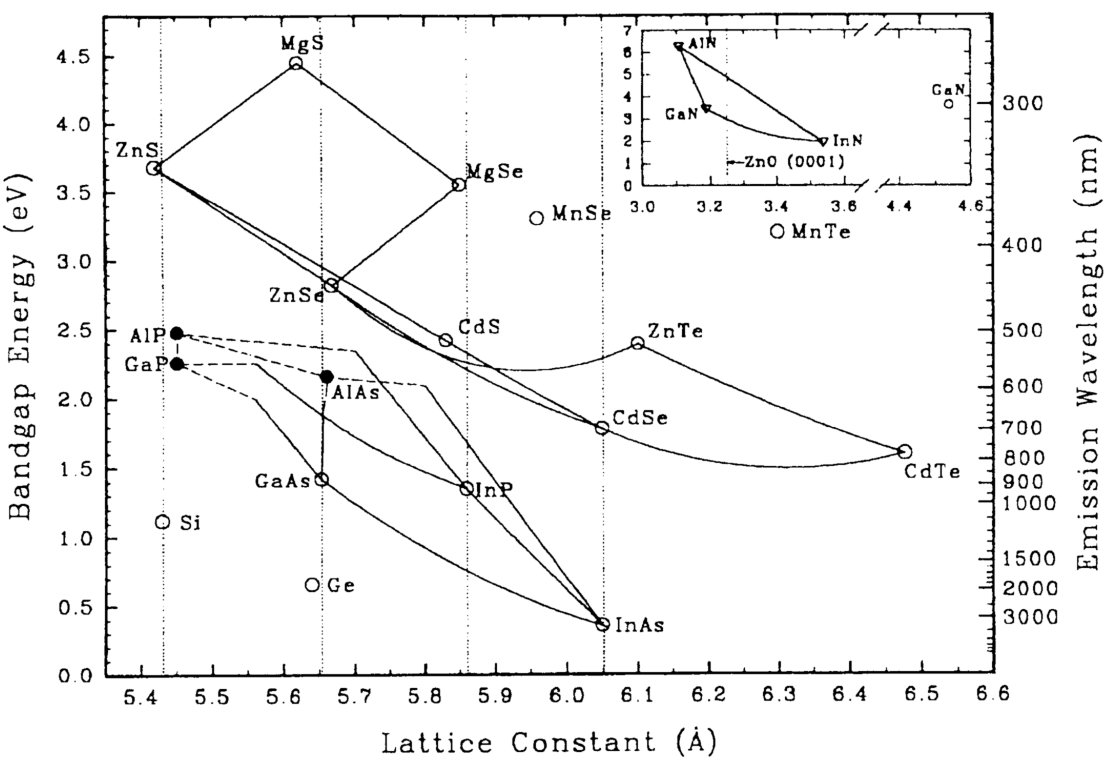

Figure 2.4: *Fundamental band gaps of many of the Group IV, III-V and II-VI semiconductors plotted against their cubic lattice constants. Taken from Ref. [GR]*

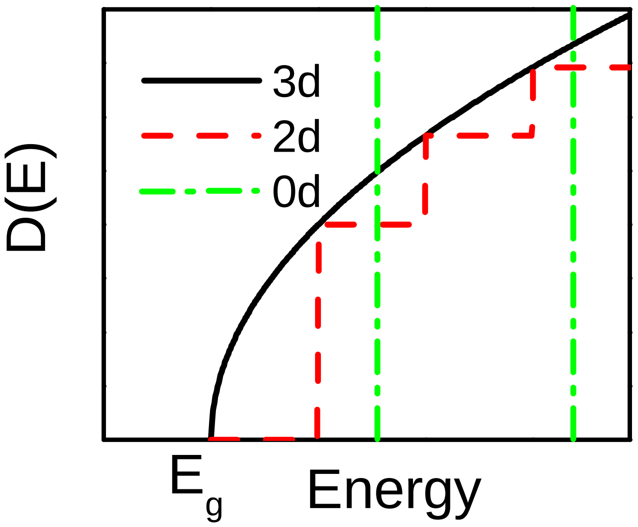

Figure 2.5: *The density of states as a function of energy for an effective material dimensionality of 3(bulk), 2(well) and 0(dot).*

these three cases. In calculating the DOS, the energies for the different cases were given by

$$E_{3D} = \frac{\hbar^2 k^2}{2m^*} \tag{2.6}$$

$$E_{2D} = \frac{\hbar^2}{2m^*}\left[k^{||2} + \left(\frac{n_z\pi}{L_z}\right)^2\right] \tag{2.7}$$

$$E_{0D} = \frac{\hbar^2}{2m^*}\left[\left(\frac{n_x\pi}{L_x}\right)^2 + \left(\frac{n_y\pi}{L_y}\right)^2 + \left(\frac{n_z\pi}{L_z}\right)^2\right] \tag{2.8}$$

where k is the wavevector and, in the 2d case, $k^{||}$ is its component in the plane of the quantum well. Thus, it can be seen that the effect of the confinement upon the DOS is large, with reduced dimensionality leading to effects not present in the bulk material. As such, low-dimensional semiconductor structures have been the source of much interesting research in recent decades. Furthermore, it is worth nothing that the effects of reduced dimensionality will also be seen in the excitonic Bohr radius and binding energy.

2.3 Dots and confined excitonic states

The discrete energy levels in a quantum dot have led to them being dubbed “artificial atoms”. Useful introductions to their properties may be found in References [Sug99, Wog97, BGL99]. There are multiple systems that may be considered dot-like, from epitaxially-grown dots, to interface fluctuations in quantum wells, to nanocrystals. Furthermore, when looking at transport processes in semiconductors, it is possible to induce dots in a quantum well either through the application of electric fields by means of gates patterned on the surface of the sample or by direct etching of a quantum-well

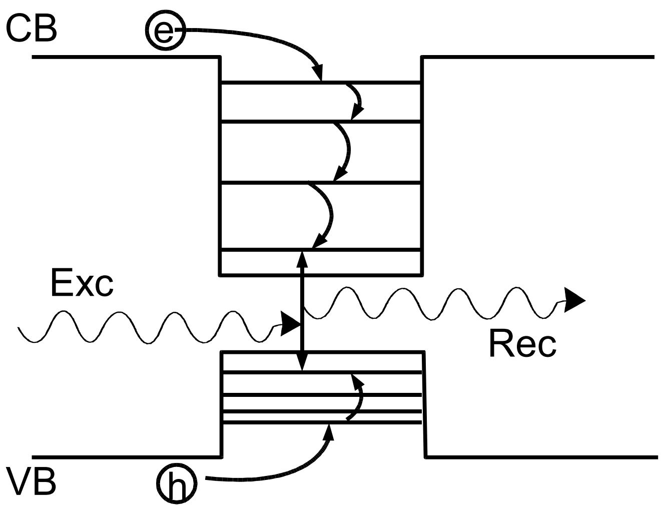

Figure 2.6: *Trapping of charge carriers in a quantum dot. Carriers in the conduction (CB) or valence (VB) bands can, through phonon-mediated relaxation, relax down through the energy levels of the dot to be trapped in the dot's ground state. From there, in the absence of thermal escape, only radiative recombination(Rec) will allow further relaxation to the crystal ground state. Direct optical excitation(Exc) of an electron-hole pair in the dot is also possible.*

sample to reduce the in-plane dimensions[RRA+88]. In this thesis I will report on work carried out upon self-assembled dots grown through a variation of molecular-beam epitaxy and upon another sample in which the dots are comprised of monolayer fluctuations in the thickness of a quantum well.

The trapping and subsequent relaxation of the charge carriers is similar in both types of dots and is shown schematically in Figure 2.6. All the experiments undertaken in this work involve optical excitation. For the non-resonant case, charge carriers are created in the barrier material about the dot. When captured by the dot, these carriers relax rapidly through the emission of, or scattering by, phonons until they are in the ground state of the dot. Since most of the experiments were performed at low ($< 50K$) temperatures, thermal escape, whereby the carriers absorb phonons until they are once more in the conduction or valence bands, is not possible. Instead, the only route by which the dot can relax to the crystal ground state is through optical recombination, either direct or, as is discussed in Section 3.6, with an additional phonon-interaction. Due to the multiple scattering events in such non-resonant experiments, the charge carriers rapidly lose any coherence with the excitation field. Alternatively, it is possible to directly create an electron-hole pair in the dot. Note that, as is the case with optical excitation in molecules, a Franck-Condon shift (also commonly referred to as a "Stokes shift") due to the effect of the charge carriers on the lattice can lead to a difference between the energy of absorption and emission from the dot[FP03].

2.3.1 Self-assembled quantum dots

The II-VI quantum dots which we investigate here are an example of epitaxially grown, self assembled dots. To grow such dots, two semiconductors of differing lattice constants are required. In this case, a layer of CdSe was grown between ZnSe barriers; CdSe and ZnSe having a 7% lattice mismatch. The resulting strain field relaxes itself through the formation of islands with increased concentration of one of the species; in the samples studies here, the islands are CdSe inside a mixed $Zn_{1-x}Cd_xSe$ layer[GMW+98, GHLW99, GWL+99]. The geometry of the resulting islands is approximately cylindrical with a height:radius ratio of $> 1 : 4$. Other material systems may result in wildly different geometries - an accepted geometry for some III-V dots is pyramidal.

2.3.2 Excitonic confinement through interface disorder

While technically "self-assembled", dot-like structures formed by interface fluctuations in quantum wells of some tens of monolayers thickness have traditionally been considered somewhat separately from the self-assembled dots described above. In the samples under investigation in Chapter 5, an AlAs/GaAs/AlAs quantum well was grown with a growth interruption of $120\,s$ at each of the interfaces. Since, in the absence of strong interdiffusion of species at the interface, the spatial distribution at transition surface from one material to another is frozen by overgrowth with the second material, it is the growth interruption which determines the geometry of the resulting interface fluctuations. Incomplete growth of the n^{th} layer will lead to *interface roughness* which can be characterised by length scale X such that an interface is described as being *atomically smooth* if there are both no changes in thickness over this scale and if the interface can be described as *abrupt*, that is, there is no perturbation to the surface from the overgrowth with the second material[KSHB91]. By allowing time for the diffusion of surface atoms to form larger islands, growth interruption can allow a selection of the size distribution of the interface fluctuations[KSH+93] with increasing growth interruption increasing the size of the islands. The resulting surface is thermodynamically stable. References [KSHB91, KSH+93] also discuss the possibility of a bimodal distribution of length scales - larger islands which trap excitons themselves having fluctuations on a scale $<< a_B$, the exciton Bohr radius, referred to as *nanoroughness.* Such a case is considered pseudo-smooth and will lead to a decrease in the ML-splitting with increasing impact of the nanoroughness[Koc03]. The effect of the nanoroughness was also observed when the energy splitting due to the fluctuations did not correspond to exactly $1\,ML$ but lay in the range $0.8 - 0.9\,ML$[GVG+97]. Nevertheless, for convenience I will still refer to the splitting as a monolayer-splitting, ignoring the effect of the nanoroughness, a not unreasonable assumption for the purposes of the work here.

Part II

Non-Coherent Spectroscopy of Single Dots

Chapter 3

Micro-Photoluminescence from Single Dots

The emission of light from non-resonantly excited carriers is a source of information on the structure of the energetic levels within the quantum dot. In particular, the spectral resolution of the photoluminescence(PL) signal shows features corresponding to excitonic, bi-excitonic and charged-excitonic states within the dot. Furthermore, measurements on ensembles of dots can, through the inhomogeneous broadening of the emission, give an indication of the size distribution of the ensemble. Scattering of excitons with phonons is also observable as additional peaks at higher(lower) energies corresponding to phonon absorption(emission) during recombination. Examination of the polarisation of the emitted light can reveal the presence of anisotropy in the shape of the dots that leads to linearly polarised emission. Time resolution of the PL recovers not only the lifetime of excitons in given states but can also show the filling of these states that occurs when charge carriers relax or are scattered from other states.

The results presented here were obtained through a micro-photoluminescence(μPL) technique. This differs from normal PL in that the imaging is performed with a high-spatial resolution. To obtain this resolution we use microscope-objective lenses to collect the light emitted from the sample. While this does not provide high enough resolution to isolate single dots on the samples we use, it does reduce sufficiently the number of dots in the collection region that other techniques can then be used to identify transitions belonging to individual dots.

3.1 Experimental techniques and apparatus

Figure 3.1 shows the scheme in which we perform μPL. Excitation of carriers is done with a laser as the light source and there are three options to choose from. Time-resolved measurements and some of the time-integrated results use frequency doubled pulses from an optically pumped Titanium-Sapphire laser emitting at $800\,nm$. A

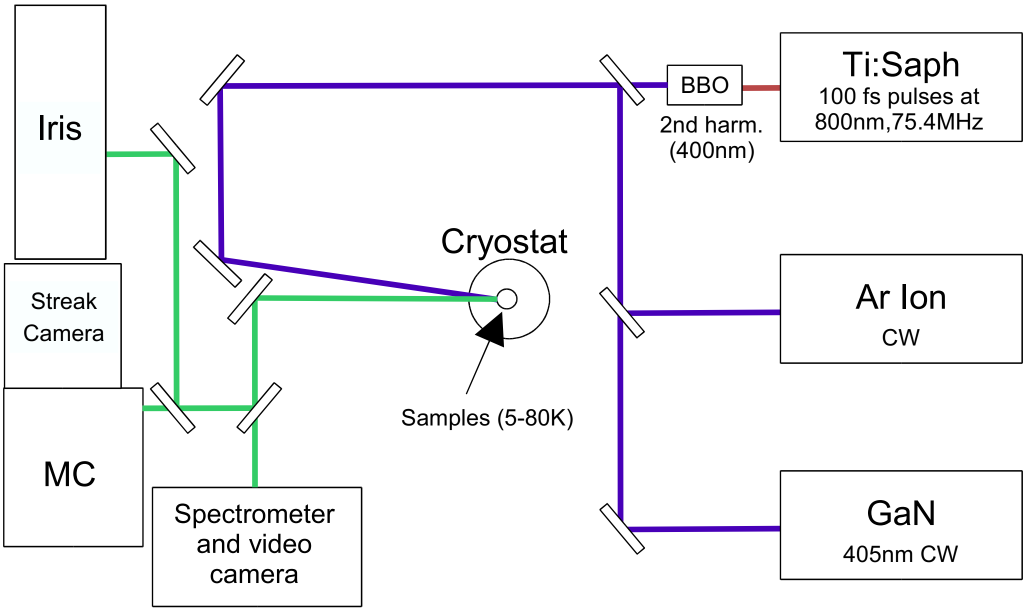

Figure 3.1: *Schematic layout of the apparatus for micro-photoluminescence (imaging optics not shown). BBO: Barium Borate crystal for* 2^{nd} *harmonic generation. MC: monochromator. Iris: High-resolution imaging spectrometer. Not shown explicitly here is the possibility of confocal excitation.*

crystal of Barium-Borate ($\beta{-}\mathrm{BaB_2O_4}$, BBO) provides the frequency-doubled pulses through second-harmonic generation. Subsequent filtering removes any remaining infra-red component. Individual pulses from this source are of approximately $150\,fs$ duration. There is also the option of using continuous-wave excitation from an Argon-ion laser or Gallium-Nitride diode laser. The light is then focussed onto the sample either at a 45^o angle from the surface normal giving an excitation spot diameter of $50\,\mu m$ diameter or is coupled into the detection beam-line using the scheme described in Section 4.2.3 to allow confocal excitation.

The sample is mounted in one of two liquid-helium cooled cryostats. The first has the sample mounted in vacuum on the cold-finger of the cryostat. A long-working distance microscope objective of numerical-aperture (NA, also described in Section 4.2.3) 0.4 collects the emitted photoluminescence. This microscope objective is mounted on an x-y-z piezo stage which allows fine control over the region of the sample from which we collect signal. Coarser control is provided by the mount of the cryostat which also allows three-dimensional translational control. One downside to this cryostat is given by the quality of the thermal contact between the sample-mount and the cold-finger which limits the temperature attainable to approximately $7.5\,K$. Furthermore, we have observed some discrepancy between the temperature of the cold-finger and the actual temperature of the sample as determined by optical properties of the emission such as the linewidth of the emission from single states.

The second cryostat is a bath-cryostat that both allows for measurements to lower temperatures ($3.5\,K$) and, through the use of a $0.85\,NA$ objective lens mounted inside the bore of the cryostat, gives higher spatial resolution and light-collection efficiency. This cryostat is also the one used in the heterodyne four-wave mixing experiments described later in the thesis.

After being collected at the cryostat, the PL is imaged onto a pinhole (not shown on Figure 3.1) in order to reduce any background luminescence. We then have four options for detection and imaging of the sample:

- A video camera is used as an aid in alignment, both in terms of the position of the excitation upon the sample and to ensure that the sample has not moved relative to the collection optics.
- A $0.5\,m$ spectrometer with a choice of 300 or $1200\,lines/mm$ gratings and a liquid-nitrogen cooled CCD as detector is used when a wide spectral range is required, for example, when correlating states to individual dots.
- To measure time-resolved photoluminescence, a synchro-scan streak camera coupled to a monochromator provides images with a time-resolution of $4\,ps$ and that are also spectrally-resolved.
- A high-resolution imaging spectrometer provides spectrally resolved data. This spectrometer is described in more detail below.

Both spectrometers used for time-integrated measurements have two-dimensional CCD detectors allowing measurement of spectra as a function of position on the input slit. Taking advantage of this, a calcite ($\mathrm{CaCO_3}$) crystal is used as a polarisation displacer, resulting in the two linear polarisation components being imaged on different parts of the input slit. We therefore have simultaneous measurement of both linear polarisations emitted from the sample.

3.1.1 High-resolution detection with the IRIS spectrometer

High-resolution detection of the emitted PL was performed with the IRIS spectrometer, an imaging grating spectrometer designed here in Dortmund by Wolfgang Langbein and built here by Wolfgang Langbein and Stephan Schneider[Sch00]. This is a 2m focal length spectrometer that uses a holographic grating of $1200\,lines/mm$ blazed at $900\,nm$ as the dispersive element, having a theoretical resolution of $9\,\mu eV$ at $800\,nm$. The large focal length allows the spectrometer to work with small angles with respect to the optical axis of the instrument and thus small imaging errors are obtained. Detection is with a two-dimensional CCD detector that is liquid nitrogen cooled and back-illuminated. The CCD consists of 2000×800 pixels (2000 along the spectrally-resolved axis), each $15\,\mu m$ square in size. This results in an effective dispersion of $8\,\mu eV$ per pixel. However, due to imaging errors, the effect of finite slit-width and pixel size the effective resolution of the system is $12 - 25\,\mu eV$.

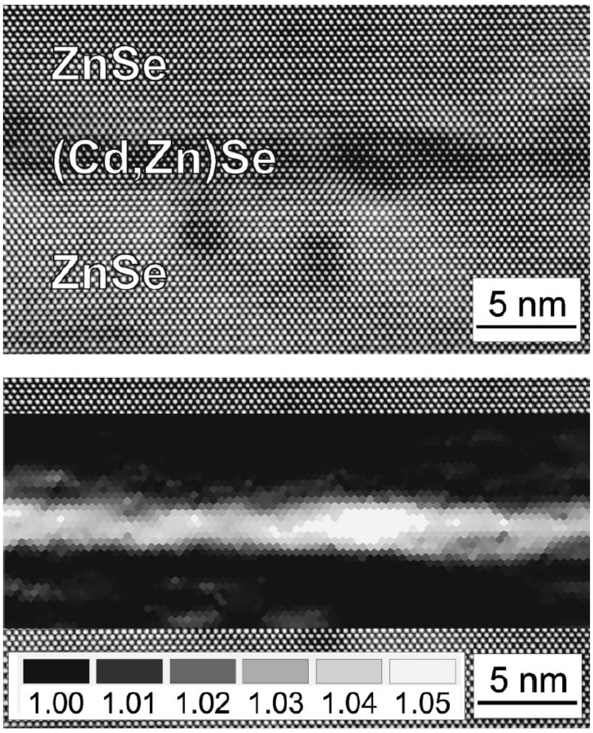

Figure 3.2: *Upper: HRTEM image of a single CdSe quantum film embedded in ZnSe of nominal deposited layer thickness of 3 ML Lower: Result of digital analysis of local lattice displacement (DALI). The gradient in the grey scale shows the increase in lattice constants starting from the pure ZnSe lattice (black) up to approximately 50% CdSe (white).(Taken from Ref.[GWL$^+$99])*

3.2 Mesa-etched CdSe/ZnSe sample

The results presented here were measured on a sample containing of CdSe quantum dots embedded in ZnSe. This type of sample has previously been characterised in References [GWL$^+$99, GMW$^+$98, LHO$^+$97]. Grown by migration-enhanced epitaxy(MEE), the dots are islands of increased Cd concentration in nominally 3 monolayer(ML) thick CdSe grown between ZnSe layers of 25 and 50 nm thickness, the lower layer of which was grown on a GaAs substrate. GaAs and ZnSe have a lattice mismatch of 0.3% and so strain due to this mistmatch can be ignored. The Cd in these islands exceeds 70%, as discussed in Reference [GWL$^+$99] where digital analysis of local lattice displacement(DALI) techniques were applied to high-resolution transmission electron microscope images in order to identify the alloy composition through the lattice spacing. It is also worth noting that, due to the diffusion processes, the thickness of the dots is greater than the nominally deposited thickness; 9ML for the deposited thickness of 3ML. The lateral dimensions are of the order $5 - 10\,nm$ which is comparible to the excitonic Bohr radius in CdSe, $a_B = 5.4\,nm$.

In order to reduce the number of dots observable within the optical resolution, an array of square mesas was etched into the sample using a process described in Reference [IBK$^+$95]. With a lateral dimension in the range of 1 μm down to 50 nm, we observed fewer than 5 optically active dots in the smallest mesas. A separation of 200μm between mesas ensured that only one was visible in the microscope objective's field of view at any one time. The time-integrated spectrum is thus one of multiple sharp lines at low temperature. The spread in energy is related to the inhomogeneous broadening of the dots and thus to their size distribution. No further discussion of this distribution will be held here, save to note that when reporting on measurements of multiple dots attempts have been made to ensure that the dots from which we took results were not grouped in any one part of the inhomogeneous broadening.

3.3 Identifying single dots: spectral wandering

Trapping of charge carriers in the nanoenvirons of a quantum dot can lead to a quantum confined Stark effect(QCSE) which manifests as a shift in the position of excitonic transitions. This change in spectral position, referred to as *spectral wandering* or *diffusion*, has been reported in References [ENG96, SWB$^+$00, TRH$^+$01, TRS$^+$00, MBT$^+$02, BKMM02]. The process by which the charge carriers are trapped and subsequently scattered from the trapping sites depends on the depth of the trapping site and the phonon scattering rate. As such, the dynamics show characteristic timescales of microseconds to seconds and can be used as a fingerprint of transitions from individual dots: the rate of change of the field is sufficiently slow that the dot may go through repeated excitation and decay cycles before a resolvable change in the magnitude of the shift becomes apparent. Thus, although certain features (such as excitons and trions) may not be present simultaneously, the slow rate of change of the Stark shift compared to the time scale of the population dynamics and the change in the charge state of the dots sees them appearing in the same spectra. It is also worth noting that the Stark shift represents only a small change in the emission energy.

The upper part of Figure 3.3 shows an example of such jitter in the spectral position. This plot was generated by taking 256 spectra of $1\,s$ integration time. Correlations in the spectral position of individual transitions are readily apparent. To better quantify the degree of correlation and to allow the analysis of spectra with multiple individual transitions we have performed a correlation analysis on the jitter-spectra. We make a correlation of the form:

$$C_{ij} = \frac{\langle E_i E_j \rangle - \langle E_i \rangle \langle E_j \rangle}{\sigma_i \sigma_j} \tag{3.1}$$

with E_i being the time-dependent position of peak number i, $\langle .. \rangle$ denotes the time-average, and $\sigma_i = \sqrt{\langle E_i^2 \rangle - \langle E_i \rangle^2}$ is the standard deviation of E_i. This correlation coefficient will be exactly unity for peaks that show up to a scaling factor the same time-evolution, and we expect peaks with a high correlation coefficient to come from the same dot.

More specifically, the spectral position of each transition can be expanded in powers of the local electric field, $\mathbf{F}_k$, at the position of the corresponding QD k:

$$E_i = E_{i0} + \mathbf{p}_i \mathbf{F}_k + \frac{1}{2} \mathbf{F}_k P_i \mathbf{F}_k + O(\mathbf{F}^3) \tag{3.2}$$

with $\mathbf{p}_i = p_i \hat{p}_i$ the permanent dipole moment of amplitude p_i and direction $\hat{p}_i$, and the polarisibility tensor P_i of the transition. Using only the linear term, and assuming zero average field $\langle \mathbf{F} \rangle = 0$ (which can be satisfied by a suitable choice of E_{i0}), we find:

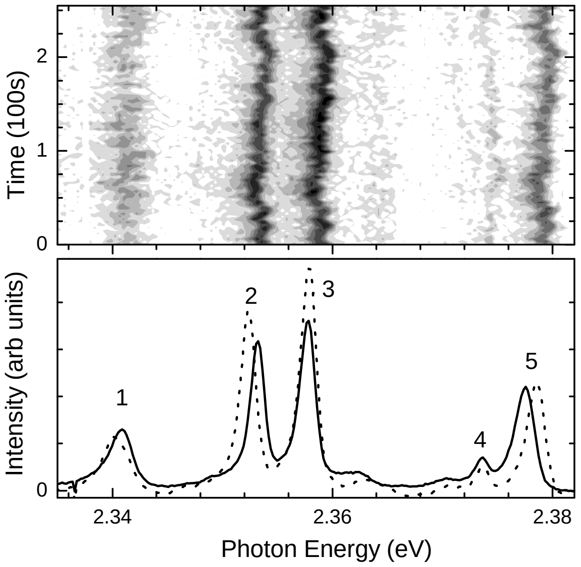

Figure 3.3: *Upper: Spectrally-resolved intensity versus time (logarithmic greyscale) Lower: Jitter-corrected, time-integrated photoluminescence spectra for the two linear polarisation directions along* [110] *and* [1$\bar{1}$0]. *Peaks are marked by their correlation-matrix index as given in the text.*

$$C_{ij} = \frac{\langle(\hat{p}_i\mathbf{F}_k)(\hat{p}_j\mathbf{F}_l)\rangle}{\sqrt{\langle(\hat{p}_i\mathbf{F}_k)^2\rangle\langle(\hat{p}_j\mathbf{F}_l)^2\rangle}} \tag{3.3}$$

The correlation is thus independent of the amplitude p_i which instead is a scaling factor of the fluctuations. For transitions in the same dot ($k = l$), the correlation is unity for parallel dipole moments ($\hat{p}_i = \hat{p}_j$). In other cases, the correlation depends both on the directional distribution of $\mathbf{F}$ and, for transitions in different dots, upon the correlation between the fields $\mathbf{F}_k$ and $\mathbf{F}_l$. If they are uncorrelated ($\langle\mathbf{F}_k\mathbf{F}_l\rangle = 0$), C_{ij} will vanish. Otherwise, the result will be a finite value of the correlation coefficient. Since the transitions under investigation are all located within the size of the relevant mesa the fields are likely to be partially correlated, and thus even transitions of different dots can show some degree of correlation.

To make the jitter correlation described in Equation (3.1) we take a series of consecutive spectra with each individual spectrum having an integration time of approximately 1 second (naturally, the integration time depends on the intensity of PL from the mesa). A simple peak finding routine finds the position of each transition for each spectrum. We can now correlate the change in spectral position for each transition which allows the grouping of spectral features. Due to the statistical nature of the shift, the correlation value is subject to error since we measure only a finite ensemble of emission energies in time (256 in the case of Figure 3.3). Additionally, due to the finite accuracy of the peak position, related both to the resolution of the spectrometer and the fact that the position of the peak is digitised by the finite array of pixels at our detector, even fully correlated peak shifts would show a measured correlation smaller than unity. Taking this into account, about ten mesas, each containing one to three dots, have been screened to extract reliable data.

The correlation coefficients found for an individual mesa were always arranged in two groups, one in the range ±0.2, which we assigned to transitions of different dots, and another one in the range 0.7 - 1.0, which we assigned to transitions in the same dot. An advantage of this correlation method is that it allows the rapid identification of groups of lines within spectra that would otherwise be laborious to work with. Five peaks in Figure 3.3 have been labelled. When performing the correlation analysis on this jitter-plot the following correlation matrix is recovered

$$C_{ij} = \left| \begin{array}{rrrrr} 1 & -0.143 & -0.138 & -0.173 & -0.108 \\ ... & 1 & 0.915 & -0.113 & 0.907 \\ ... & ... & 1 & -0.145 & 0.882 \\ ... & ... & ... & 1 & -0.130 \\ ... & ... & ... & ... & 1 \end{array} \right|$$

The matrix is symmetric, hence only the upper half is presented. It can be seen that peaks $2, 3$ and 5 are correlated while peaks 1 and 4 belong to two different dots (since there is no independent correlation between these two transitions). At this point peaks belonging to a single dot have been identified, however the excitonic species responsible for the transition is not yet clear. The following section discusses how we label the peaks.

3.4 Anisotropy in the dots: polarised emission

Of the three transitions labelled above, both transition 3 and 5 show a behaviour with increasing excitation intensity that is linear at low intensities and then becomes saturated as we increase the excitation further. This is characteristic of single excitonic transitions, either charged (trion) or uncharged. At low excitation intensities the PL is limited by the number of excitons that can be captured by the dot. When, on average, less than one exciton is captured per pulse (or in a time period governed by the intradot relaxation and subsequent radiative relaxation to the crystal ground state for CW excitation) then the emission will depend on the number of charge carriers and so will be linear with the excitation intensity. As the mean number of charge-carriers captured on the time scales described above increases past one per cycle we begin to see a saturation effect, with the capture of multiple excitons quenching the emission of the single-exciton line. Conversely, peak 2 is absent at the lowest excitation intensities and shows a quadratic behaviour with increasing intensity. This is characteristic of biexcitonic transitions; until the carrier density after excitation is sufficiently high to provide an appreciable probability of capture of multiple excitons there will be no emission from this state. Figure 3.4 shows this intensity dependence for the emission at $13\,K$ from a different dot to that of Figure 3.3. Only one linear polarisation is presented here and the peaks in this figure have already been labelled as exciton (X), trion (T) and biexciton (XX). The reference excitation intensity, I_0 was $250\,\mu W$ in a spot of $50\,\mu m$ diameter.

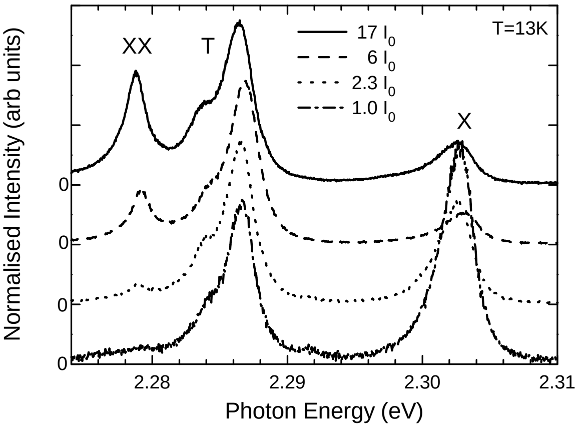

Figure 3.4: *Excitation intensity dependence of μPL. Peaks labelled are exciton (X), trion (T) and biexciton(XX). Reference excitation intensity I_0 is 250 μW in a 50μm diameter excitation spot*

The labelling of the exciton and trion peaks takes advantage of the linear polarisation splitting observable in Figure 3.3. Here, the direction of the polarisation is along the [110] and [1$\bar{1}$0] crystal directions. The fine structure results from exchange interactions which have been treated theoretically in Reference [FWFZ98] and has been observed in both semiconductor nanocrystals [NNK$^+$95, CGL$^+$96, WGWK96] and epitaxially grown III-V [BF02, GSS$^+$96] and II-VI quantum dots [PRWH99, BKM00]. Electron-hole exchange interaction splits the fourfold degenerate heavy-hole exciton state by a splitting energy δ_0 into a radiative (bright) doublet with total pair angular momentum of $\pm 1\hbar$ and a non-radiative (dark) doublet of $\pm 2\hbar$. In QDs of cylindrical symmetry in the [001] direction the dark doublet is split further by a splitting energy δ_2. Breaking the cylindical symmetry, e.g. by an anisotropic confinement potential, as shown in Figure 3.5, splits the bright doublet by a splitting energy δ_1 into two states which have optical transitions to the ground state which are linearly polarised along the two orthogonal principal axes of the elliptical part of the anisotropy. For single excitons in CdSe/ZnSe QDs values of δ_1 between 0 and more than 0.8 meV were reported [KBW$^+$99]. In a CdSe/ZnSe QD ensemble, average values of $\delta_0 = 1.9$ meV, $\delta_1 = 0.2$ meV and $\delta_2 < 0.02$ meV [PRWH99] were measured. For comparison, in CdTe/ZnTe quantum dots bright-state splittings δ_1 from 0.06 to 0.32 meV were found [MBT$^+$02].

From the anisotropy-split level diagram in Figure 3.5 it can be seen that, for one polarisation, the peak for the biexciton transition is expected to be at a lower energy than for the other polarisation, while the excitonic peak is at a higher energy. This process whereby the peaks for one polarisation act as bookends to those of the other polarisation is characteristic of a biexciton/exciton pair within a single dot and hence, returning to the peaks labelled in Figure 3.3, allows us to identify peaks 2 and 5 as being such a pair. Consider the case of a negatively charge trion in its lowest state. This will consist of two electrons of opposite spin and a hole with two possible spin orientations, that is, the complex is a hole interacting with a spin-singlet electron pair. Thus, the exchange energy splitting is no longer present[BOS$^+$02] and the trion will exhibit no splitting in the polarisation. It can be seen that this is the case for peak 3. We have identified the excitonic species responsible for the transitions occurring within a single dot.

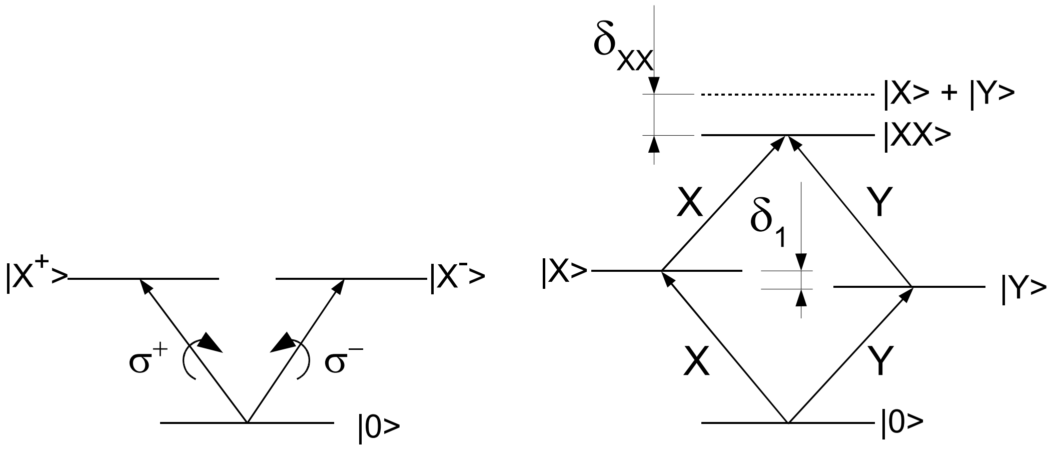

Figure 3.5: *Left: In cylindrically symmetric dots the two optically active exciton states $|X^{+,-}\rangle$ are spin-degenerate and accessible optically by circularly polarised light,$\sigma^{+,-}$ Right: Elongation along one of the radial axes lifts the degeneracy, resulting in two exciton states that emit linearly polarised light along (orthogonal) directions labelled X and Y.*

As is shown in Figure 3.5, the Coulomb interaction between the two excitons that comprise a biexciton leads to a shift in the energy of the transition, δ_{XX} from that expected by two non-interacting excitons (shown as $|X\rangle + |Y\rangle$ in the diagram). This binding energy is derived by calculating the energy difference with respect to the energy of the bright exciton, i.e. we neglect the correction due to polarisation splitting introduced in Reference [KBW+99]. Since the observed polarisation splitting is smaller than the experimentally obtained standard deviation of the biexciton binding energy itself, this approximation is justified. Figure 3.6 shows the binding energies we derived using this method for trions and biexcitons plotted versus their emission energy. As a result of this analysis we have found biexciton binding energies of $19 - 26\,meV$ and trion binding energies of $15 - 22\,meV$. We have always observed the trion emission at a higher energy than that of the corresponding biexciton. Note that the binding energy for both quasi-particles is quite well defined. Interestingly, the trion binding energy is comparable to energy shifts observed in charged colloidal CdSe nanocrystals [SWF+02]. Theoretical predictions [FZ00] indicate that singly-charged nanocrystals should emit 22 meV to the red of the neutral exciton emission. For the biexciton binding energy the data reproduce well the value measured in quantum dot ensembles by use of femtosecond four-wave mixing (FWM) and two-photon absorption techniques [GWL+99]. No systematic trend of biexciton binding energies with increasing exciton localization is observed. This may be due to the 150 meV energy window in which we detected biexciton emission being too small to observe any pronounced confinement induced increase in biexciton binding energy.

The lower part of Figure 3.6 shows the observed polarisation splittings $E_{[110]} - E_{[1\bar{1}0]} = \delta_1$ of the exciton peak. Note that we could only determine the orthogonal directions [110] and [1$\bar{1}$0] by the orthogonal cleavage facets of the crystal which leaves an ambiguity in the absolute ordering. However, since all QDs are on the same crys-

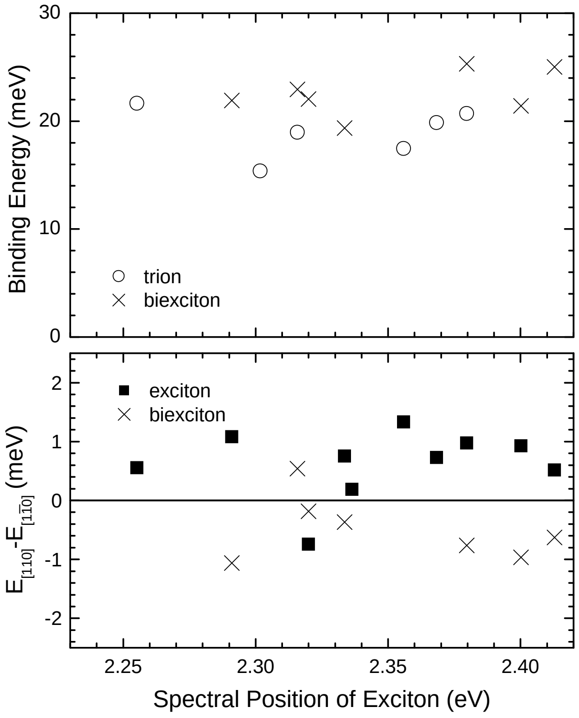

Figure 3.6: *Top: The binding energy of trions and biexcitons versus the spectral position of the transition. Bottom: The polarisation splitting observed for biexcitons and excitons versus the spectral position of the transition.*

tal, their relative polarisation orientation is unambiguous. The results indicate an anisotropy in the confining potential experienced by the excitons. The asymmetry-induced splitting does not show a systematic size dependence, as was also the case in results from InGaAs QDs[BF02]. However, the splitting as given above is dominantly positive for the exciton, so that the exciton anisotropy is not completely random but has a size that is preferentially larger in the $[1\bar{1}0]$ crystal direction.

The consequences of the exchange interaction for the fine structure of the biexciton and the trion transitions are the following: The trion ground state is a spin-singlet state and the wave function overlap of the two electrons (or holes) in the trion gives zero local spin density of the two electron (holes). The trion's third carrier does not experience an exchange interaction and thus the trion peak does not exhibit an exchange splitting. Indeed, to within the experimental resolution ($100\,\mu$eV) we have not observed any trion polarisation splitting. Because the biexciton has no spin degeneracy, the biexciton to exciton transition shows the (inverted) fine structure of the exciton transition [BKM00, KBW$^+$99]. Therefore the peak positions of the linearly polarised exciton and biexciton transitions are inverted relative to each other, as discussed above and as can be observed in the lower part of Figure 3.3. The polarisation splitting observed for the biexciton is 0.2 - 1.2 meV as can be seen in Figure 3.6. As expected, the observed exchange splitting of exciton and biexciton is equal to within the experimental accuracy. We have not seen any relationship between the magnitude of the polarisation splitting and other parameters such as the biexciton binding energy or the transition energy.

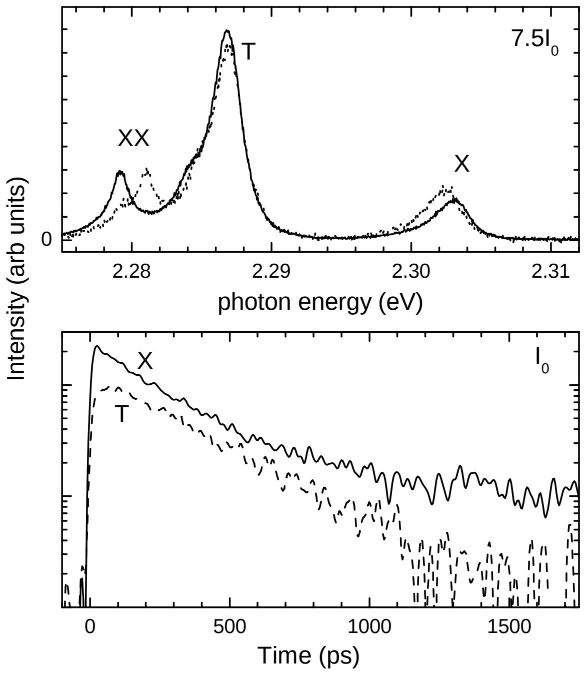

Figure 3.7: *Top: Time-integrated photoluminescence for linear polarisations along* [110] *(solid) and* [1$\bar{1}$0] *(dashed). Bottom: Time-resolved photoluminescence intensity (log scale) of the exciton (X) and trion (T) emission after pulsed excitation at time zero. The excitation intensity was* $I_0 = 250\,\mu W$.

3.5 Time-resolved photoluminescence

As mentioned in Section 3.1, we have the option of performing time-resolved measurements of the μPL by using a streak camera. In the setup used for these experiments an imaging monochromator disperses the light collected from the sample. The output slit of the monochromator is aligned parallel to the input slit of the streak camera so that we have simultaneous energy- and temporal-resolution of the PL. A stripe-shaped photo-cathode at the entrance of the streak camera emits electrons which are accelerated towards a phosphorescent screen. During the transit to the screen they are deflected perpendicularly to their flight-path by a time-varying electric field which determines the temporal resolution of the detected image. A CCD array of 640 × 512 pixels detects the light emitted by the screen and allows readout to a PC for subsequent data analysis.

Figure 3.7 shows the time-resolved decay of a trion and an exciton at a low excitation intensity along with the corresponding time-integrated PL spectrum for this dot. With an excitation intensity of $I_0 = 250 \mu W$, this figure shows the low intensity regime of the PL where there is no biexciton population in the dots and in which the intensity dependence of the excitons has not yet reached the saturation regime. We have fitted the data for the exciton with a bi-component exponential decay. The initial decay is dominated by a part with a decay-constant of 240 ps. The second component of the decay has a decay-constant of 2.5±0.5 ns. We attribute this long-time component to a repopulation process of the bright from the dark exciton states. From the presence of the long-time component it is clear that there is a finite probability of a transition between bright and dark exciton states, which presents an additional channel for the initial population decay of the bright exciton state. The initial decay time of $240\,ps$

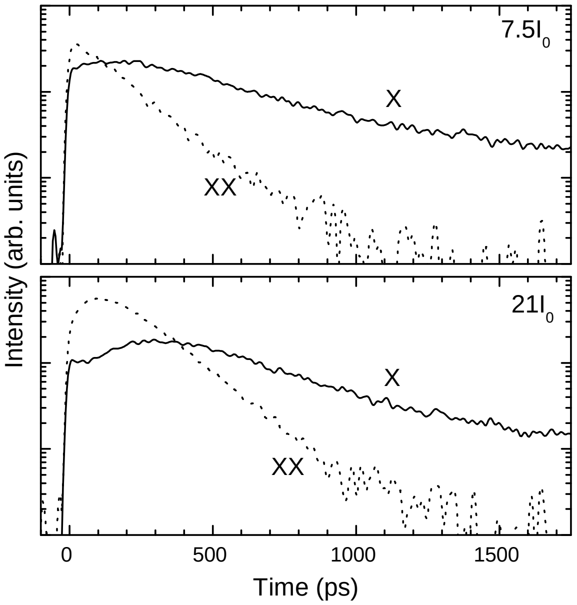

Figure 3.8: *Top: Time-resolved photoluminescence plot of an exciton (X) and biexciton (XX) for the same quantum dot. Bottom: The same features as above at a higher excitation intensity such that the biexciton also shows signs of refilling.*

is thus not purely due to radiative decay. This process is discussed in further detail in Section 3.5.1, where the temperature-dependence of the time-resolved photoluminescence is used to gain additional insights in to the dark-bright state splitting and scattering processes between the two types of state. Note that the trion does not possess such a dark ground state and, indeed, we see it exhibit no such behaviour at long times. Instead we observe a single exponential decay with a time of 320 ps. In addition, it shows an initial refilling behaviour, which is not shown by the exciton, even at low excitation intensities. We attribute this to a spin-relaxation process in which the trion starts from a state with equal spin for all carriers, which is a dark state. One of the two equally charged carriers is in the first excited electronic state since Pauli blocking prevents the relaxation into the ground state. A spin-flip lifts the blocking and allows the carrier to relax. After the spin-flip, the trion state is bright and the radiative recombination can be observed. The probability of creating this blocked initial state by non-resonant optical pumping, assuming a random spin distribution of the carriers, is only 1/4, so the slow process does not dominate the average trion emission dynamics. The observed rise has a time constant of 30-50 ps, and we attribute it to this spin-flip relaxation.

Figure 3.8 shows the time-resolved photoluminescence of the exciton and biexciton transition for medium and high excitation intensities. The biexciton is fitted by a mono-exponential decay and was found to have a decay time of $170\,ps$ which is faster than the exciton. When looking at the biexciton decay time in a selection of dots we found that, in most cases, the ratio of the exciton decay time to the biexciton decay time was approximately 2:1, in contrast to some previous results [BWS$^+$99] but in agreement with ensemble data [GWL$^+$99] and recent experiments on InAs quantum dots [SSPY02] which also show an enhancement of the biexciton decay-rate over that of the exciton. For both intensities shown in Figure 3.8 the exciton now shows an initial refilling. A good fit is obtained by setting the time-constant for this refilling to the decay time of

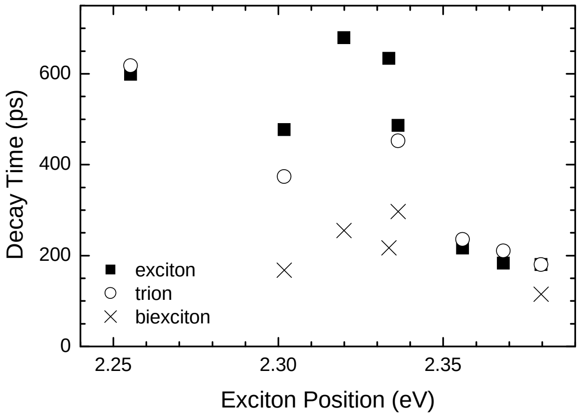

Figure 3.9: *Measured PL intensity decay times for exciton, biexciton, and trion transitions in multiple quantum dots versus the corresponding exciton transition energy.*

the biexciton. At the highest intensities we also see evidence for refilling of the biexciton from states which have 3 or more excitons in the dot. Examination of the spectra from the streak camera at times soon after the excitation of the sample showed a short lived peak $4\,meV$ below the biexciton. Its decay time of $140\,ps$ is comparable to the rise time of the biexciton at this intensity and so it can be tentatively labelled as a triexciton. Naturally, further examination of the properties of this peak would be required to make this identification more trustworthy. At the highest excitation intensities the trion also begins to show signs of refilling other than the spin-flip refilling discussed above. Furthermore, the time constant for this additional refilling is comparable to that of the biexciton, suggesting that a charged biexciton is responsible for this effect. However, we have been unable to isolate a peak corresponding to this transition and so also cannot present an energy splitting.

Beside this representative quantum dot discussed in Figures 3.7 and 3.8, we screened the decay dynamics of a much larger number of quantum dots. Figure 3.9 shows the resulting decay times for the different transitions in the investigated single dot ensemble. Note that the times given here for the exciton are only those of the fast initial decay.

As can be seen from Figure 3.9, the trion has a lifetime comparable to that of the exciton, while the biexciton has a lifetime which is shorter than the exciton, typically by a ratio of 2:1. This result is in agreement with both earlier data measured on ensembles [GWL$^+$99] and more recent single-dot experiments [SSPY02]. Furthermore, the observed systematic increase of the decay times with decreasing transition energy is in agreement with measurements on the ensemble [GWL$^+$99], and is attributed to the decreasing coherence volume of the excitons with increasing localization. While trions and biexcitons are characterized by an almost monoexponential decay, the presence of a dark state complicates the analysis of the exciton dynamics.

In the next Section we therefore give an overview of the temperature-dependent exciton dynamics in the time range $< 1\,ns$ using data from a streak-camera.

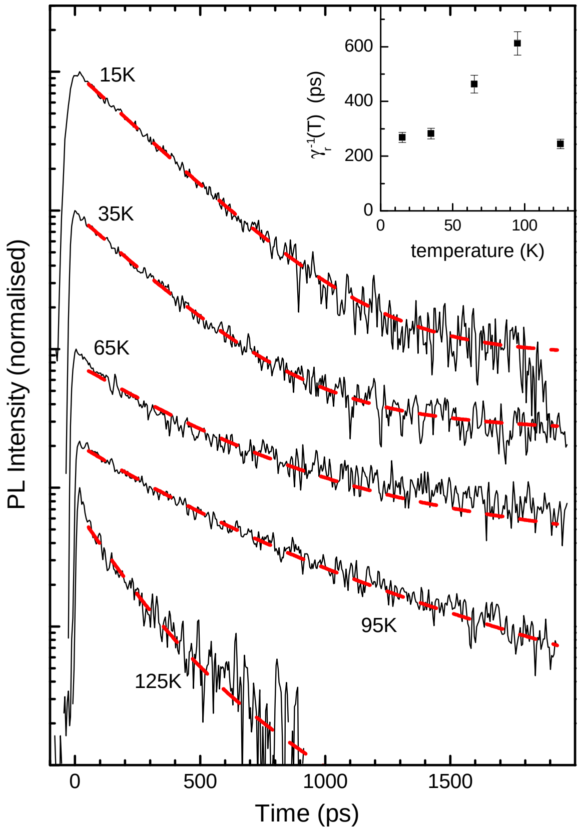

Figure 3.10: *Time-resolved photoluminescence decay of the exciton at varying temperatures as indicated. The inset shows the extracted temperature-dependence of the effective radiative lifetime* $\gamma_{\mathrm{r}}^{-1}(T)$ *of the spin-singlet exciton state ensemble (see text).*

3.5.1 Temperature dependent photoluminescence of excitons

Figure 3.10 shows the time-dependent photoluminescence of the exciton at low excitation intensites (ie, no significant population of biexcitons is present). Three regimes are apparent: At the lowest temperatures there is little repopulation from the dark state, leading to emission dynamics that are dominated by the decay of the bright exciton. Increasing the temperature results in an increasing repopulation of the bright state from the dark. Indeed, by $65\,K$ there is a strong contribution from the dark state-refilling. Finally, at temperatures above $100\,K$ there is a strong decrease in the lifetime of all transitions, something that we attribute to the thermal escape of carriers from the dots and their subsequent non-radiative recombination.

The analysis of the PL dynamics is performed by applying a simple rate equation model to the observed behaviour. At low temperatures it is expected that the dynamics after the initial (rapid) capture of carriers by the dots and their relaxation to the ground state of the dots will be dominated by two decay rates γ_{r} and γ_0. The first describes the radiative recombination of the exciton while the second gives the phonon-assisted scattering rate between the two bright (spin singlet) and the two dark (spin triplet) exciton states. Furthermore, a bright-dark splitting, δ_0, is assumed. As the temperature increases we need to include contributions from both the thermal population of excited exciton states and from thermal escape of the excitons into the ZnCdSe quantum well surrounding the dots. Since the thermal population of excited exciton states is rapid when compared to escape and spin-flip we absorb it into a temperature-dependent effective radiative decay rate $\gamma_{\mathrm{r}}(T)$ of the bright exciton states. Escape from the dots is through a phonon-assisted transition with escape energy δ_e and a scattering rate γ_{e}. Recapture of charge-carriers by the dot is considered to be negligible: in the small mesa structures investigated here we expect the carriers to be mostly captured by surface states. This is supported by the thermally-activated decrease in the time-integrated emission intensity. We can then write the rate equations governing the probability of bright excitons (n_{b}) and dark excitons (n_{d})as:

$$\partial_t n_{\mathrm{b}} = -n_{\mathrm{b}}\left(\gamma_{\mathrm{r}} + (1+N_0)\gamma_0 + N_{\mathrm{e}}\gamma_{\mathrm{e}}\right) + n_{\mathrm{d}} N_0 \gamma_0 \tag{3.4}$$

$$\partial_t n_{\mathrm{d}} = -n_{\mathrm{d}}(N_0\gamma_0 + N_{\mathrm{e}}\gamma_{\mathrm{e}}) + n_{\mathrm{b}}(1+N_0)\gamma_0 \tag{3.5}$$

where $N_{0,\mathrm{e}}$ denotes the Bose occupation number of phonons $(\exp(\delta_{0,\mathrm{e}}/k_{\mathrm{B}}T) - 1)^{-1}$ at the energies $\delta_{0,\mathrm{e}}$ of bright-dark splitting and escape, respectively. Since we perform non-resonant excitation with linearly polarised light the carriers will lose their spin polarisation during the initial phonon-assisted relaxation into the dots and we can also assume an initially equal probability of creating bright or dark excitons, *i.e.* $n_{\mathrm{b}}(0) = n_{\mathrm{d}}(0)$. Since the excited average exciton number is less than one, the effect of multiexciton states on the dynamics [IM96] is not considered.

The set of temperature dependent transients of the PL intensity can be fitted with the analytical solution of Equation (3.4) for $n_{\mathrm{b}}(t)$, since the intensity is proportional to the probability of the exciton being in the bright state. A consistent fit (see dashed lines in Figure 3.10) is found for the parameters $\delta_0 = 1.5\,\mathrm{meV}$, $\delta_{\mathrm{e}} = 30\,\mathrm{meV}$, $\gamma_0 = 0.08\,\mathrm{ns}^{-1}$, $\gamma_{\mathrm{e}} = 30\,\mathrm{ns}^{-1}$, and the temperature-dependent effective radiative lifetime of the spin singlet states $\gamma_{\mathrm{r}}^{-1}(T)$ shown in the inset. The value of δ_0 is similar to previous findings [PRWH99], and the escape energy δ_{e} is close to the LO-phonon energy of ZnSe (31 meV), indicating that the escape is mediated by LO-phonon absorption. The spin relaxation time γ_0^{-1} is about 13 ns, much longer than the radiative decay rate. This is consistent with previous observations of the bright-state spin dynamics [TFHL$^+$01]. The radiative lifetime γ_{r}^{-1} is 270 ps at low temperature, where only the lowest electronic states are populated. With increasing temperature, the effective $\gamma_{\mathrm{r}}^{-1}(T)$ of the spin singlet exciton states increases due to the population of excited exciton states, of which a large fraction has smaller radiative recombination rates due to the small envelope function overlap between electron and hole.

The temperature dependence of the spectral wandering has also been measured and is shown in Figure 3.11. The jitter dynamics can be divided into a continuous jitter of the spectral position and intensity of spectral features, and into a component with abrupt changes of the spectral intensity. With increasing temperature, the homogeneous linewidth of the emission increases, so that the spectral jitter becomes less obvious. The low-frequency components of the spectral jitter decrease with increasing temperature, so that at 120 K only fast intensity jitter remains. I will leave discussion at this qualitative level, while a quantitative analysis and modelling like that in References [TRS$^+$00, SWB$^+$00, BKMM02] is not attempted.

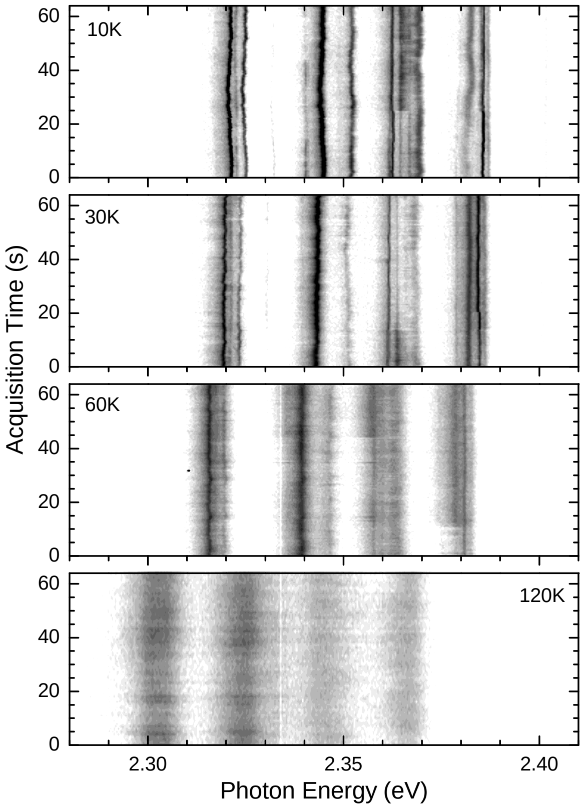

Figure 3.11: *Spectrally-resolved intensity versus time (logarithmic greyscale) shown at temperatures of (from top) 10K, 30K, 60K and 120K.*

3.6 Non-Lorentzian emission lineshape

The high-resolution images obtained from the IRIS spectrometer open the possibility of extracting information on the dephasing and relaxation processes directly from the lineshape of the transitions. The dynamics of the relaxation are related to the lineshape through a Fourier transform. This can be shown easily for the simplest case of a monoexponential decay where the intensity as a function of time decays exponentially $I(t) \propto e^{-\gamma t}$. If the field responsible for the detected intensity has a centre frequency ω_0 then it can be written as

$$E(t) = \begin{cases} 0 & for\ t < 0 \\ E_0 e^{-t\gamma/2} cos(\omega_0 t) & for\ t > 0 \end{cases} \tag{3.6}$$

which has a Fourier transform of

$$\begin{aligned} F[E(t)] &= E(\omega) = \int_0^\infty E_0 e^{-t\gamma/2} cos(\omega_0 t) e^{i\omega t}\, dt \\ &= \tfrac{1}{2} E_0 [\tfrac{1}{2}\gamma - i(\omega + \omega_0)]^{-1} \\ &\quad + \tfrac{1}{2} E_0 [\tfrac{1}{2}\gamma - i(\omega - \omega_0)]^{-1} \end{aligned} \tag{3.7}$$

If $\omega \approx \omega_0$ then we ignore the first term and can recover the frequency-dependent intensity $I(\omega)$

$$\begin{aligned} E(\omega) &\approx \tfrac{1}{2} E_0 [\tfrac{1}{2}\gamma - i(\omega - \omega_0)]^{-1} \\ |E(\omega)|^2 = I(\omega) &= \frac{E_0^2}{\gamma^2} \frac{\gamma^2}{4(\omega-\omega_0)^2 + \gamma^2} \end{aligned} \tag{3.8}$$

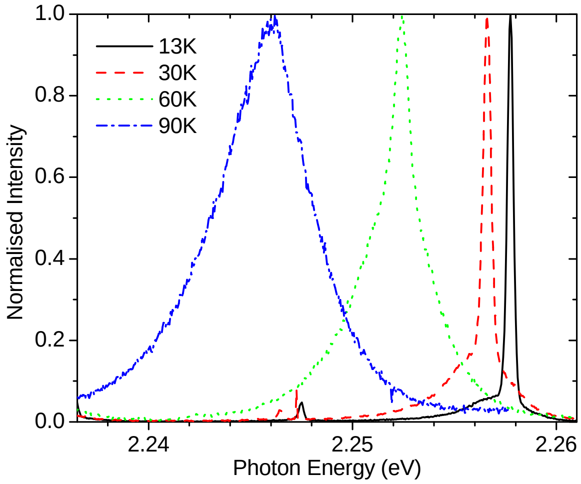

Figure 3.12: *Non-Lorentzian lineshape of exciton versus temperature.*

This intensity distribution is known as the Lorentzian. Due to the spectral wandering, which can be considered to be a random process, an additional Gaussian component is added to the lineshape. The resulting spectral profile is described by the Voigt function, a convolution of Lorentzian and Gaussian functions. The additional broadening due to the Gaussian can be minimised by choosing spectra whose jitter-spectra show minimal spectral wandering and by making multiple, short exposures whose change in spectral position can then be corrected by the spectral-offset matrix used to generate the correlation matrix described in Equation (3.1). This results in spectra that have no contribution to their lineshape from jitter processes with a lifetime longer than the integration time for a single acquisition. The cost is greater readout noise since multiple spectra need to be read out.

Figure 3.12 shows the jitter-corrected spectrum of a single linear-polarisation from a single exciton at multiple temperatures. The lineshape is clearly neither Lorentzian nor Gaussian, consisting of a narrow central peak at low temperatures whose spectrally-integrated weight decreases with increasing temperature. The other component of the lineshape is a broad background which is asymmetric at low temperature.

Such features have already been noted in PL experiments on both CdTe[BKMM01] and InAs[FCF$^+$03, UMK$^+$04] dots and, more recently, in spectral-hole burning experiments on CdSe dots[PWG$^+$04]. Furthermore, four-wave mixing experiments on InGaAs/GaAs dots[BLS$^+$01] have shown a non-exponential polarisation decay that corresponds to a sharp central peak with a broad background. The four-wave mixing results in particular have lead to a number of theoretical papers on the phenomemon[KAK02, ZR02, FWDK03, ZM04, MZ04]. Experimental results show that not only does the central peak decrease in spectral weight with increasing temperature, but it also shows an increase in spectral width. This is of importance since the standard theoretical model for these systems does not predict such an increase in width.

The theoretical understanding of the non-Lorentzian lineshape attributes the broad background to acoustic-phonon assisted radiative recombination, with phonon emission(absorption) at energies below(above) the ZPL, while the central peak is the direct radiative recombination without phonon participation and is referred to as the zero-phonon line (ZPL). The model of choice for these systems is the independent-Boson model since it allows an exact analytical solution for the linear optical polarisation and for the photon echo observed in FWM experiments. In this model the exciton-phonon interaction is linear in the phonon displacement operators and excited excitonic states are neglected. Its exact solution describes the broad-band satisfactorily but fails to reproduce the broadening of the ZPL.

To model the lineshape measured in μPL measurements, a model and corresponding fitting routing developed by Prof. Roland Zimmermann in the *Institut für Physik der Humbolt-Universität zu Berlin* is used and the derivation below follows the References [ZM04] and [MZ04]. Based on the independent-Boson model, it extends the standard model by adding a phenomenological decay rate which accounts for the long-time decay of the polarisation and hence the broadening of the ZPL. The Hamiltonian used for this model is

$$H = \sum_j E_j B_j^\dagger B_j + \sum_{\mathbf{q}} \hbar\omega_{\mathbf{q}} a_{\mathbf{q}}^\dagger a_{\mathbf{q}} + \sum_{jl\mathbf{q}} M_{\mathbf{q}}^{lj}(a_{\mathbf{q}}^\dagger + a_{-\mathbf{q}}) B_j^\dagger B_l \tag{3.9}$$

where E_j is the energy of the exciton in the j_{th} level, $B_j, B_j^\dagger$ are the annihilation and creation operators of the excitons, a phonon with wavevector $\mathbf{q}$ and energy $\hbar\omega_{\mathbf{q}}$ has annihilation and creation operators $a_{\mathbf{q}}, a_{\mathbf{q}}^\dagger$ and the coupling is given by the matrix $M_{\mathbf{q}}^{lj}$. It is assumed that the states are separated sufficiently in energy that there is no comparable phonon energies and so little coupling between states. Thus the matrix element is diagonal: $M_{\mathbf{q}}^{lj} \propto \delta_{lj}$. Furthermore, only one level, the QD ground state, is considered i.e. $j - l = 0$. For simplicity the matrix element is now written as $M_{\mathbf{q}}$ and the electric charge densities for the electron and hole enter through this element.

As has been mentioned, the exact solution (via a technique known as the cumulant technique) of this model is possible and leads to a final result for the polarisation of

$$P(t) = ie^{-it\tilde{\omega}_{10} + R(t) - S} \tag{3.10}$$

with

$$R(t) = \sum_{\mathbf{q}} \frac{M_{\mathbf{q}}^2}{\omega_{\mathbf{q}}^2}[(2N_{\mathbf{q}} + 1)cos(\omega_{\mathbf{q}} t) - i\sin(\omega_{\mathbf{q}} t)] \tag{3.11}$$

and introducing the Huang-Rhys factor which is a measure of the electron-phonon coupling strength

$$S = R(0) = \sum_{\mathbf{q}} \frac{M_{\mathbf{q}}^2}{\omega_{\mathbf{q}}^2}(2N_{\mathbf{q}} + 1) \tag{3.12}$$

and where a thermal average over phonon operators leads to a Bose distribution of phonons $N_{\mathbf{q}} = \langle a_{\mathbf{q}}^\dagger a_{\mathbf{q}} \rangle = 1/(exp(\hbar\omega_{\mathbf{q}}/k_B T) - 1)$ where k_B is Bolzmann's constant, T is the temperature, and $\tilde{\omega}_{10}$ is the transition frequency after being corrected for the polaron shift and gives the position of the ZPL.

Since there is no long-time decay of the polarisation in Equation (3.10), a phenomenological decay rate Γ is added by hand and models both the radiative decay

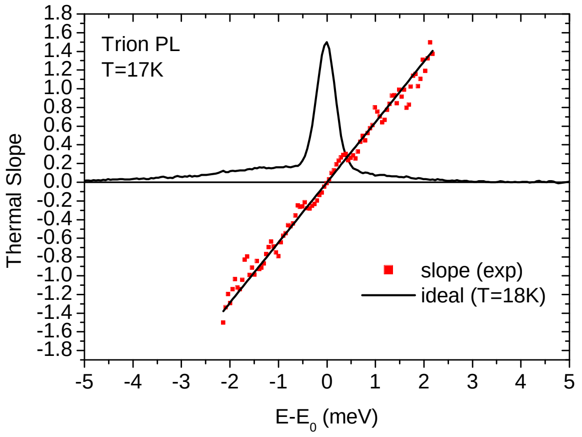

Figure 3.13: *Application of Equation (3.15) to PL of trion. Dots indicate the slope calculated from the data, the solid line is the predicted slope for a phonon temperature of 18K.*

and higher order phonon scattering. A complex Huang-Rhys factor, which occurs if phonon-damping is included, is also allowed for: $S = S_1 + iS_2$. The polarisation is now given by

$$P(t) = ie^{-i(t\tilde{\omega}_{10}+S_2-R_2(t))+R_1(t)-S_1-\Gamma t} \tag{3.13}$$

Fourier transforming the imaginary part of the polarisation gives the absorption spectrum

$$P_2(\omega) = -\int_0^\infty \Im e^{i\omega t} P(t)\, dt \tag{3.14}$$

The ZPL is found to have a weight $Z = e^{-S_1}$ and the additional dephasing Γ gives it a Lorentz lineshape. The rapid initial dephasing of the polarisation accounts for the broad spectral background. Indeed, when fitting to the data it was found that separating the ZPL led to better results, i.e. $P_2(\omega) = P_2^{ZPL} + P_2^{phonon}$. The effect of the spectral wandering is to contribute a Gaussian component to the ZPL and the Lorentz broadened ZPL will show a Voigt profile instead. Naturally, there will also be an effect on the broad band, however this will only comprise a small fraction of the total width of this component of the lineshape.

Since the broad band depends on a thermal distribution of phonons, it can be used as a 'phonon thermometer'[ZM04] where the zero of energy is taken to be at the ZPL. This arises from the difference between phonon emission, $\propto N_{\mathbf{q}} + 1$, and phonon absorption, $\propto N_{\mathbf{q}}$. Note also that there is a mirror symmetry between absorption and photoluminescence $I(\omega) = P_2(-\omega)$, leading to

$$log\left(\frac{I(-\omega)}{I(+\omega)}\right) = \frac{\hbar\omega}{k_B T} \tag{3.15}$$

Figure 3.13 shows the result of calculating the phonon temperature from the PL of a trion at 17 K. The dots indicate the thermal slope, with the solid line showing the predicted case for a phonon temperature of 18 K.

To fit the data it is necessary to describe the geometry of the dot and a coupling function for the exciton-phonon interaction. Acoustic phonons of dispersion $\omega_{\mathbf{q}} = qs$,

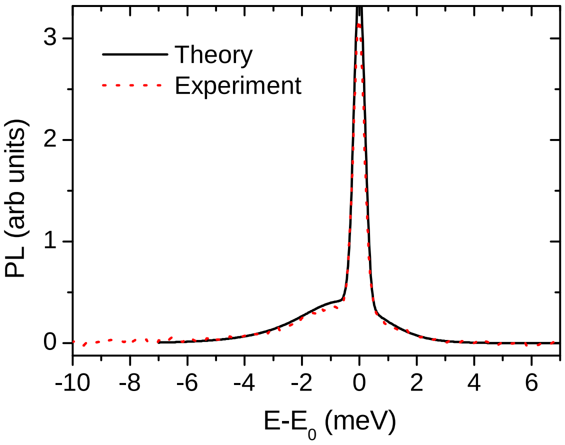

Figure 3.14: *Comparison of the observed spectrum of a trion at 17K (dotted line) with that calculated by the method described in the text.*

where s is the velocity of sound in the material, are used. Furthermore, instead of the matrix element $|M_{\mathbf{q}}|^2$, we use a coupling function of the form

$$f(E) = \frac{1}{4\pi^2 s^2 \rho_M (\hbar s)^3} |\int dr e^{i\mathbf{q}\cdot\mathbf{r}} (D_c \rho_e(\mathbf{r}) - D_v \rho_h(\mathbf{r}))|^2 \ , \quad (E = \hbar q s) \tag{3.16}$$

where ρ_M is the mass density of the crystal, $\rho_{e,h}$ the charge density of the electron or hole and $D_{c,v}$ the deformation potential of the conduction and valence bands. The form of Equation (3.16) can be understood as an angular average over $\mathbf{q}$ since $N_{\mathbf{q}}$ depends only on $|q|$. In the ground state the charge densities of electrons and holes are similar and so for this fitting we set $\rho_e(\mathbf{r}) = \rho_h(\mathbf{r}) = \rho(\mathbf{r})$. What is important is the spatial distribution of charge. A prolate spheroid (pancake) model is applied; a cylindrically symmetrical distribution that has a radial size greater than the height (z) extent. The form of the charge distribution is given by a Gaussian distribution

$$\rho_{\mathbf{q}} = \exp(-q_r^2 l_r^2/4 - q_z^2 l_z^2/4) \tag{3.17}$$

remembering that r here is the radial component in a cylindrical geometry.

Figure 3.14 shows the results of applying the independent-Boson model with additional dephasing to the CdSe dots under investigation in this chapter of the thesis. The important parameters of the calculation are as follows:

T (K)	17
l_r (nm)	2.4
l_z (nm)	1.1
σ_G (meV)	0.19
$Scale_{D_c-d_v}$	1.75
$D_c - D_v(meV)$[LS91]	-4250
s (m/s) [Med82]	4070
ρ_M (g/cm^3) [Bha97]	5.42

where σ_G is the width of the Gaussian used to model the ZPL and $Scale_{D_c-d_v}$ is an empirical weighting factor for the band edge deformation potentials. Since the model

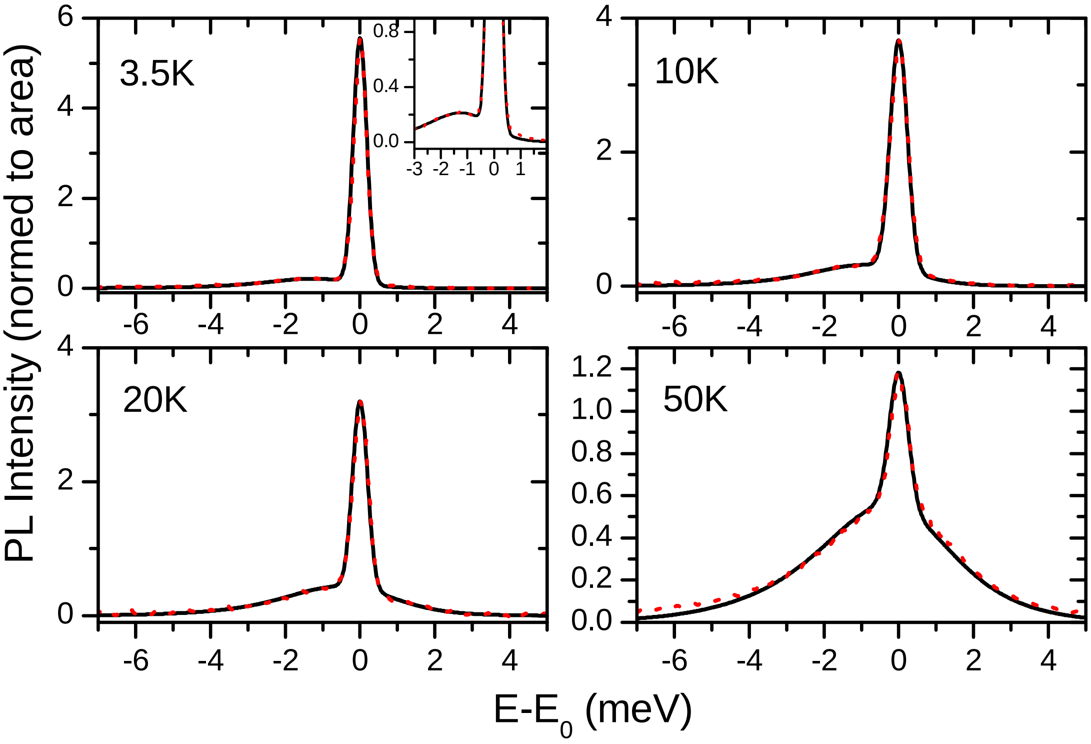

Figure 3.15: *Theoretical calculation (solid lines) of trion lineshape at multiple temperatures using the (non-temperature) parameters given in the table above. Good agreement with experiment (dotted lines) is evident. Inset(3.5K): Enlarged view of the region about the ZPL showing that a dip in the acoustic phonon assisted emission which is present at low temperatures also appears in the modelled data.*

assumes bulk-like phonons, the material parameters given here are not those for CdSe, the dot material, but the relevant values for ZnSe since it is phonons from the ZnSe barriers that we assume will interact with the excitonic states. Indeed, calculating the PL spectra using the CdSe values gave neither reasonable extensions, l_r, l_z, for the excitonic wavefunction nor a good fit at multiple temperatures for a single set of parameters.

Figure 3.15 shows the result of calculating the PL spectrum at varying temperatures using the (non-thermal) parameters given above. In order to optimise the fit it was necessary to vary the value of $Scale_{D_c-d_v}$ by some $15-20\%$ over the range of temperatures invesitgated $(3.5-50K)$. Futhermore, in contrast to the expected behaviour of an increasing ZPL width with increasing temperature, we saw no evidence of such behaviour here. However, this is not entirely unexpected. Fitting the ZPL with a Voigt profile instead of the Gaussian one used in this routine shows that, up to approximately $50K$, the Lorentzian component of the Voigt is dominated by the Gaussian component. In other words, at these low temperatures the effects of spectral wandering upon the ZPL width dominate any intrinsic width due to the dephasing of the state. Measurements at higher temperatures, to extract this Lorenztian broadening, are also complicated by the fact that, as can be seen in Figure 3.16, the fraction of the total

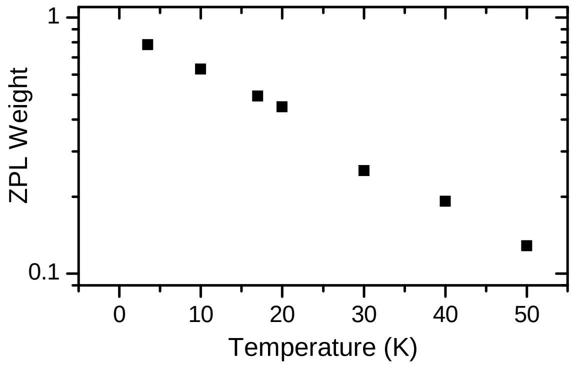

Figure 3.16: *The fraction of the PL emission given by the ZPL as a function of temperature.*

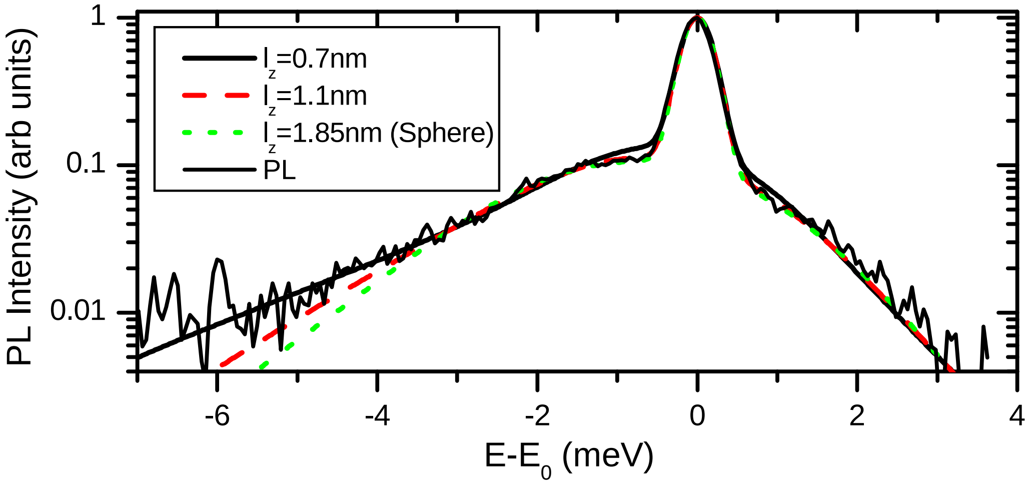

Figure 3.17: *Effect of dot geometry on the PL lineshape. A range of aspect ratios for equal QD volume, labelled by their extent in the z-direction, are used to generate PL spectra. Also shown is the observed PL at* $T = 17\,K$.

emission which is due to the ZPL decreases rapidly with increasing temperature. Since the emission efficiency also decreases with temperature, it is somewhat of a challenge to extract reliable data over a wide temperature range. Nevertheless, the fits to the experimental data given by this model, and using a Gaussian to represent the ZPL, are very satisfactory. The inset to the PL at $3.5K$ in Figure 3.15 expands the view of the region about the ZPL. The increasing asymmetry in the phonon-assisted band with decreasing temperature leads to in interesting effect whereby a dip appears in the PL in the spectral region immediately below the ZPL. This is clearly seen in our data and is also recovered in the theoretical calculations.

In order to get a feel for the effect of the aspect ratio, $l_r : l_z$, of the dot upon the emission, we calculated the PL spectrum for a range of values while keeping the volume $l_r^2 l_z$ of the wavefunction constant. Figure 3.17 shows the results of these calculations, indexed by the value l_z, and the observed PL at $T = 17\,K$. The range investigated runs from an extremely flat dot to one with spherical symmetry. The constraints of the programme used to calculate the PL meant that we were unable to move from such a ‘thin pancake’ to a spherical dot and then on to a ‘cigar’ geometry ($l_z > l_r$). As can be seen, the effect of increasing spherical symmetry serves to reduce the interaction with phonons at higher energies, and thus $|q|$ values, shown by the increasingly rapid drop-off of the PL emission with decreasing emission energy. Conversely, the thinnest geometries show a deterioration of the agreement with the data close to the ZPL line, a region where we desire a good fit from the model. The fact that these thin geometries appear to show a good agreement at energies lower than $4\,meV$ is not of importance here for two reasons. Firstly, in order to maximise the signal from the exciton and trion it was necessary to use excitation powers close to the saturation regime of the exciton, where the biexciton begins to become apparent. Since the separation of the trion and biexciton is of the order of a few meV and the biexciton is below the trion in emission energy, we cannot be certain that any deviation in the quality of the fit is due to the model and not due to the fact that there may be some contribution from the biexciton. Secondly, it is also worth noting that the noise begins to dominate at these low signal intensities and so it would be foolhardy to weight the fit heavily here. We have found that the emission is relatively insensitive to the geometry in the range $1.0 < l_z < 1.4\,nm$. Hence, our initial estimation of $l_z = 1.1\,nm$ is supported by the calculations shown here.

Part III

Coherent Spectroscopy of Single Excitonic States

Chapter 4

Heterodyne Four-Wave Mixing: Theory and Experimental Details

4.1 Theory

In this section we will look at the theoretical grounding for both four-wave mixing (FWM) and optical heterodyne techniques. The FWM is examined in terms of the *independent two-level model* which assumes two states, $|\Psi_a\rangle$ and $|\Psi_b\rangle$, of energy E_a and E_b which are sufficiently far from other states that a photon nearly resonant to the transition between $|\Psi_a\rangle$ and $|\Psi_b\rangle$ is far off resonance with respect to other transitions. Using this approximation, we can derive equations that govern the behaviour of the system under resonant excitation.

4.1.1 Optical Bloch equations

In this formalism we are interested in the effect of an electromagnetic field upon an ensemble of identical two-level systems. The requirement that the individual systems be isolated means that this approach works equally well for both a spatial ensemble of such systems and for repeated measurements upon a single system in such a way that the results of each measurement may be considered to be independent of the previous measurements. The derivation of the optical Bloch equations presented here follows that of Reference [Sha96].

We first define the *density matrix operator*, ρ for an ensemble of such systems. This describes the statistics of such an ensemble

$$\rho = \sum_j P_j |\Psi_j\rangle\langle\Psi_j| \tag{4.1}$$

where P_j is the fraction of the systems with state vector $|\Psi_j\rangle$ with $j \in \{a, b\}$ for a two-level system. In this case we can also write the density operator conveniently as

$$\rho = \begin{bmatrix} \rho_{bb} & \rho_{ba} \\ \rho_{ab} & \rho_{aa} \end{bmatrix} \tag{4.2}$$

In such a description it is useful to view the diagonal elements as the probability of finding the system in the relevant eigenstate, with the off-diagonal elements being the coherence between the states. In a closed system it is also worth remembering that the system is normalised to one, ie

$$\rho_{aa} + \rho_{bb} = 1 \tag{4.3}$$

Since we are treating the system quantum mechanically, it follows the Schrödinger equation and, in particular, the Liouville form of the equation. Using $\dot{\rho} = \delta\rho/\delta t$ and the commutator $[H, \rho] = H\rho - \rho H$ we write the equation as:

$$i\hbar\dot{\rho} = [H, \rho] \tag{4.4}$$

with H the Hamiltonian for the system and having the form

$$H = H_0 + H_{int} + H_R \tag{4.5}$$

where H_0 is the Hamiltonian of the isolated system, H_{int} describes the effect of the interaction between the system and the electromagnetic field and H_R is a phenomenological description of relaxation and dephasing processes. In the absence of the interaction and relaxation terms the Hamiltonian has no explicit time-dependence and so we find solutions of the form

$$\Psi_j(\mathbf{r}, t) = \phi_j(\mathbf{r})e^{-iE_jt/\hbar}, \quad H_0\phi_j = E_j\phi_j \tag{4.6}$$

with ϕ_j normalised to one.

Extending the model to a system of n independent, two-level systems we find that the state-vector for the n-th system is given by

$$|\Psi_n(\mathbf{r}, t)\rangle = c_{an}(t)|\Psi_a(\mathbf{r}, t)\rangle + c_{bn}(t)|\Psi_b(\mathbf{r}, t)\rangle \tag{4.7}$$

and, using Equations (4.2) and (4.1), we can write the density matrix for the system explicitly

$$\rho = \sum_n P_n \begin{bmatrix} |c_{bn}|^2 & c_{bn}c_{an}^* \\ c_{an}c_{bn}^* & |c_{an}|^2 \end{bmatrix} \tag{4.8}$$

noting that the off-diagonal elements are only non-zero where there is a well-defined phase relationship between all the different n in the ensemble, *i.e.* there is coherence in the ensemble. We are interested in interaction Hamiltonians of the form

$$H_{int} = -\mathbf{p}.\mathbf{E}(\mathbf{r}, t), \quad \mathbf{p}_{ij} = -e\int d^3r\phi_i^*\mathbf{r}\phi_j \tag{4.9}$$

The components of H_{int} are thus given by

$$\Delta_{ij} = -\mathbf{p}_{ij}.\mathbf{E}(\mathbf{r}, t) \tag{4.10}$$

This assumes electric-dipole allowed transitions with an incident electric field $\mathbf{E}(\mathbf{r}, t)$ and an electric dipole moment of the charged particle $\mathbf{p}$. Furthermore, we are working in the dipole approximation which assumes that the characteristic size of the wavefunction describing the particle, a_0 is much smaller than the wavelength of the incident electric field. Hence, there is a negligible contribution to the Hamiltonian from the wavevector-dependent term since $\mathbf{q}a_0 << 1$.

Since H_{int} is the representation of a physical observable it is a self-adjoint operator, that is, $H_{ij} = H^*_{ji}$. Furthermore, the matrix H_{ij} can be additionally simplified by taking into account the fact that $\mathbf{p}$ is an odd-parity operator and so the diagonal components of H_{ij} will be zero.

Consider a monochromatic plane wave, linearly polarised in the direction ϵ, and with a frequency ω. The electric field can then be written as the sum of two fields

$$\mathbf{E}(\mathbf{r}, t) = \mathbf{E}^+(\mathbf{r}, t) + \mathbf{E}^-(\mathbf{r}, t) \tag{4.11}$$

with

$$\mathbf{E}^+(\mathbf{r}, t) = \frac{1}{2}\epsilon E_0 e^{i(\mathbf{q}\cdot\mathbf{r}-(\omega t+\eta))}, \;\; \mathbf{E}^-(\mathbf{r}, t) = \mathbf{E}^{+*}(\mathbf{r}, t) \tag{4.12}$$

where E_0 is the (real) electric field amplitude and η is an overall phase term. Looking at the time-dependent terms of Equation (4.10) and using the field given by Eq. (4.11) we see that there are two terms, one with a phase factor $\propto e^{i(\Omega+\omega)t}$ where $\Omega = (E_b - E_a)/\hbar$. The *rotating wave approximation* is applied and this term is ignored, leading to an explicit form for Δ_{ba} of

$$\Delta_{ba} = (\hbar/2)e(\mathbf{r}_{ba}\cdot\epsilon)E_0 e^{i(\mathbf{q}\cdot\mathbf{r}-(\omega t-\eta))} \tag{4.13}$$

This can be thought of as making a time-average to remove the rapidly varying terms. In later sections it will become useful to note that the *Rabi-frequency*, Ω_R can be extracted here from $\Omega_R = e(\mathbf{r}_{ba}\cdot\epsilon)E_0/\hbar$ at resonance (when $\omega = \Omega$). The interaction Hamiltonian matrix can thus be written as

$$H_{int} = \begin{bmatrix} 0 & \Delta_{ba} \\ \Delta^*_{ab} & 0 \end{bmatrix} \tag{4.14}$$

As mentioned above, the relaxation component H_R of the Hamiltonian is accounted for phenomenologically with two time constants, T_1 and T_2 corresponding to the lifetime of the population and the coherence, respectively

$$\begin{aligned} [H_R, \rho]_{bb} &= -i\hbar\rho_{bb}/T_1 \\ [H_R, \rho]_{ba} &= -i\hbar\rho_{ba}/T_2 \end{aligned} \tag{4.15}$$

Having the full Hamiltonian, it is now worth rewriting the density matrix to take into account all important terms. Using the notation for the population $n = \rho_{bb}$, $1-n = \rho_{aa}$ and polarisation $p = \rho_{ba}$ we get

$$\rho = \begin{bmatrix} n & p \\ p^* & 1-n \end{bmatrix} \tag{4.16}$$

and can recover the *optical Bloch equations*[Sha96]

$$\dot{n} = -n/T_1 - (i/\hbar)(\Delta_{ba}p^* - p\Delta_{ba}^*) \tag{4.17a}$$

$$\dot{p} = -p(i\Omega + 1/T_2) - (i/\hbar)\Delta_{ba}(1-2n) \tag{4.17b}$$

These equations form the basis for the analysis of coherent transient equations in two-level systems. However, they cannot be solved analytically in the general case. Instead, the density and polarisation are Taylor expanded in order to obtain a solution to the desired order. With

$$\begin{aligned} n &= n^{(0)} + n^{(1)} + n^{(2)} + \ldots \\ p &= p^{(0)} + p^{(1)} + p^{(2)} + \ldots \end{aligned} \tag{4.18}$$

we use initial conditions of $n = 0$ and $p = 0$ and note that odd powers of n and even powers of p are zero. The optical Bloch equations can then be written to the third order as

$$\dot{p}^{(1)} = -(i\Omega + 1/T_2)p^{(1)} - (i/\hbar)\Delta_{ba} \tag{4.19a}$$

$$\dot{n}^{(2)} = -n^{(2)}/T_1 - (i/\hbar)(\Delta_{ba}p^{(1)*} - p^{(1)}\Delta_{ba}^*) \tag{4.19b}$$

$$\dot{p}^{(3)} = -(i\Omega + 1/T_2)p^{(3)} + 2(i/\hbar)\Delta_{ba}n^{(2)} \tag{4.19c}$$

That is, the $i+1$ order of $n(p)$ is influenced by the i order of $p(n)$. On a matter of terminology, remembering that the polarisation is given by $p = \epsilon_0\chi E$, with χ the susceptibility, it is common to refer to non-linear optic experiments according to the order in the Taylor expansion in which the processes governing them occur, but using the susceptibility as the term being expanded. Four-wave mixing would then be referred to as a $\chi^{(3)}$ process.

To look at the four-wave mixing signal we will consider a two-beam, degenerate experiment in which two pulse trains, seperated by a delay τ and propagating along directions $\mathbf{q}_1, \mathbf{q}_2$ interact with the sample. For delay times which are small compared to the dephasing time T_2 the polarisations created by pulses 1 and 2 can interfere to create a grating resulting in the self-diffraction of pulse 2 along the direction $\mathbf{q}_d = 2\mathbf{q}_2 - \mathbf{q}_1$ In order that Equations (4.19) are analytically soluble, we consider the case where the pulses are delta-functions and ignore propagation effects (equivalent to assuming that the sample is thin). We can write the resulting pulse train at the sample as

$$E(\mathbf{r}, t) = \left[E_1\delta(t)e^{i\mathbf{q}_1\cdot\mathbf{r}} + E_2\delta(t-\tau)e^{i\mathbf{q}_2\cdot\mathbf{r}}\right]e^{i\omega t} \tag{4.20}$$

where $E_{1,2}$ is the amplitude of the relevant field, ω is the centre frequency of the laser pulses and we absorb the refractive index into the coordinate $\mathbf{r}$. Furthermore, we assume that the first pulse arrives at time $t = 0$ and the second at a time $t = \tau$. Writing the solutions to the Bloch equations to third order directly, we get

$$p_1 = (er_{ba}/i\hbar)\left\{E_1 e^{-Gt}\Theta(t) + E_2 e^{-G(t-\tau)}\Theta((t-\tau))\right\} e^{i\omega t} \tag{4.21a}$$

$$n^{(2)}_{21^*} = (e^2|r_{ba}|^2/\hbar^2)E_2E_1 \left\{ \begin{array}{l} \Theta(-\tau)\Theta(t)e^{-t/T_1+G\tau} \\ +\Theta(\tau)\Theta(t-\tau)e^{-(t-\tau)/T_1-G^*\tau} \end{array} \right\} \tag{4.21b}$$

$$p^{(3)}_{221^*} = -i(e|r_{ba}|/\hbar)^3 e^{-i\omega t} e^{i(2\mathbf{q}_2-\mathbf{q}_1).\mathbf{r}} E_1 E_2^2 \times \Theta(\tau)\Theta(t-\tau)e^{-Gt+(G-G^*)\tau} \tag{4.21c}$$

where Θ is the Heaviside step function and $G = (1/T_2 + i(\Omega - \omega))$. Thus, the first order polarisation is a sum of two damped oscillations at ω displaced by the delay τ when at resonance ($\Omega = \omega$) while the second order term in n contains two terms of which only one is non-zero for $\tau > 0$ and the other non-zero for $\tau < 0$. Futhermore, the second-order population is only present after the second pulse (be that pulse 1 or pulse 2) arrives and then decays exponentially. The third order polarisation (which is what we measure in a FWM experiment) only appears for positive delays and after the second pulse arrives. Thereafter it decays with the time T_2, the dephasing time.

Since we are dealing with ensembles which may have a distribution of transition energies it is worth looking at two cases for this distribution. The first, *homogeneous broadening*, is described above and is dominant when the distribution of energies is smaller than the natural linewidth given by $\Gamma_h = 2\hbar/T_2$. Note that this case also applies when looking at a time-ensemble of measurements on a single transition in the absence of any time-dependent change in transition energy (*i.e.* in the absence of spectral jitter). As mentioned above, the third order polarisation is created at $t = \tau$ for positive delays and then Free-Polarisation Decay (FPD) occurs, a process analogous to free-induction decay in nuclear magnetic resonance, with a decay constant $\tau_{decay} = T_2/2$. For a finite pulse width τ_p the peak of the FPD is delayed to $t = \tau + \tau_p$ but the decay time is unchanged.

The other regime of interest is when the broadening of the ensemble is greater than the homogeneously broadened linewidth. In this *inhomogeneously broadened* case the phase evolution of the individual components of the ensemble occurs at different rates given by the time-dependent Schrödinger equation. Hence, the macroscopic polarisation rapidly decays to zero even though the individual polarisations have evolved in the absence of any dephasing processes. However, the second pulse reverses the phase evolution of the ensemble, resulting in the well known photon echo at a time $t = 2\tau$ when the components of the ensemble are once more in phase. This phenomenon will be examined in more detail in Section 5.3.

4.1.2 Vector model of the Bloch equations

An alternative representation of the optical Bloch equations, which will be particularly useful when looking at Rabi oscillations in the population of the excitonic system, is the vector representation[Jon03]. We write a unitary vector, the *Bloch vector*, of the

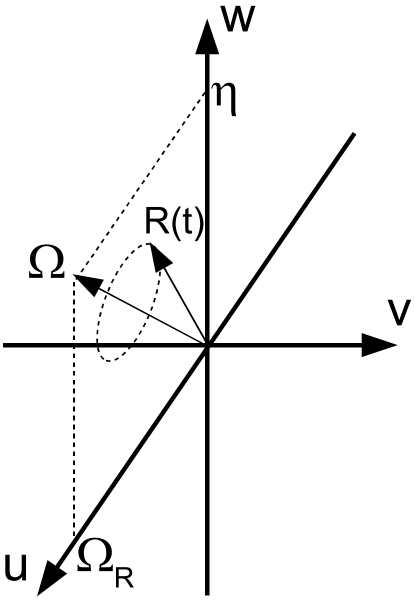

Figure 4.1: *Evolution of the Bloch vector* **R** *around the precession vector* Ω_B*. In the absence of external fields, and ignoring any thermal population of the upper state, the vector will relax towards the ground state, at* $w = -1$.

form $\mathbf{R} = (u, v, w)$. Its components are given by

$$u = \rho_{ba}^{\Omega} + \rho_{ab}^{\Omega}, \quad v = i(\rho_{ba}^{\Omega} - \rho_{ab}^{\Omega}), \quad w = \rho_{bb} - \rho_{aa} \tag{4.22}$$

where, using the rotating-wave approximation, the substitution $\rho_{ab} = \rho_{ab}^{\Omega} exp\left[i(\Omega - \eta)t\right]$ gives the temporal envelope of the off-diagonal density-matrix elements, recalling that $\Omega = (E_b - E_a)/\hbar$ and with the detuning $\eta = \Omega - \omega$. The optical Bloch equations in the absence of any thermal population of the upper-level are then given by

$$\dot{u} = -\eta v - u/T_2 \tag{4.23a}$$

$$\dot{v} = -\eta u + \Omega_R w - v/T_2 \tag{4.23b}$$

$$\dot{w} = -\Omega_R v - w/T_1 \tag{4.23c}$$

recalling the Rabi-frequency $\Omega_R = e(\mathbf{r}_{ba} \cdot \epsilon)E_0/\hbar$. The coordinate w thus describes the inversion of the system, while u and v are related to the polarisation of the system. Hence, when measuring the FWM of the system, it is the component of **R** projected onto the $u - v$ plane that will determine the signal.

Equations (4.23) can also be expressed as

$$\dot{\mathbf{R}} = \Omega_B \times \mathbf{R} - \underbrace{(u/T_2, v/T_2, (w+1)/T_1)}_{Relaxation\ Terms} \tag{4.24}$$

where Ω_B is a vector that describes the precession of the Bloch-vector

$$\Omega_B = (-\Omega_R, 0, \eta) \tag{4.25}$$

Figure 4.1 shows the evolution of the Bloch vector in this model. An external electric field excites the vector from its equilibrium state (in the absence of thermal occupation of the upper level) of $\mathbf{R} = (0, 0, -1)$. The vectorial form of the optical Bloch equations is of particular use when looking at the phenomenon of Rabi oscillations (Section 5.4), where the $\omega = \Omega$ and so the w-component of Ω_B is zero, resulting in a precession of the Bloch vector about u, *i.e.* (in the absence of dephasing) a cyclical inversion of the population followed by a return to the ground state.

4.1.3 Heterodyne four-wave mixing

In the previous section the FWM signal in the spatial-selection case was examined. However, if the two pulse trains are chosen so that they have different optical centre-frequencies ω_1, ω_2 then FWM will also be detected at the frequency $2\omega_2 - \omega_1$. In practice, this is achieved by the use of acousto-optic modulators (AOMs), described in more detail in Section 4.2.1, to achieve a radio-frequency shift in the centre-frequency of the pulses. Since the pulse width is given by the Fourier transform of the pulse shape in time and we are using pulses of sub-picosecond duration, the shift induced by the AOM is negligible compared to the overall pulse width. Such heterodyne FWM mixing techniques were developed to study FWM in waveguides where spatial selection is not possible due to the requirement of coupling into the waveguide[HLIR92, MMH96].

4.1.4 Signal to noise ratio

Performing the recovery of the FWM signal through spectral interferometric methods (see Section 4.2.4) has an additional benefit in terms of the signal to noise ratio of the recovered signal[LGX99]. In particular, at the detector, the mean square signal current is given by

$$< i_S^2 >= 2(e\eta/\hbar\omega)^2 I_{ref} I_{signal} \tag{4.26}$$

where η is the detector efficiency and $I_{ref}(I_{signal})$ is the intensity of the reference(signal). As can be seen, we can increase the measured signal simply by increasing the intensity of the reference. Furthermore, since the photocurrent is being increased with the reference, it is possible to reach the shot-noise limit, that is, the point at which detector and readout noise is negligible compared to the shot-noise of the reference field, given by

$$< i_n^2 >= 2e^2 \eta B I_{ref}/\hbar\omega \tag{4.27}$$

where B is the bandwidth of the receiver. Combining Equations (4.26) and (4.27) we find the signal to noise ratio to be

$$< i_S^2 > / < i_n^2 >= \eta I_{signal}/(\hbar\omega B) \tag{4.28}$$

giving a minimum detectable signal of

$$I_{signal(min)} = \hbar\omega B/\eta \tag{4.29}$$

Furthermore, since we are using a balanced detection scheme which is shot-noise limited, we also compensate for classical intensity fluctuations of the laser. Thus the detection noise can be limited by the reference shot-noise!

4.2 Experimental setup

In comparison to the microphotoluminescence experiments described earlier the requirements for realisation of this heterodyne four wave mixing scheme are quite steep:

- This is a three-beam experiment; pump, probe and reference. We need control over

  The polarisation of the beams

  The pulse width

  The centre-frequency of individual pulses

  The relative delay between the three beams

- At the sample we need to be able to select a small spatial region to minimise the number of excitonic states contributing to the signal
- Since the magnitude of the signal is quite small, it is important to have both a high collection efficiency at the sample and to minimise loss of signal in the detection path
- The use of an AOM to perform the mixing required for spectral interferometry requires a careful choice of detection optics. Furthermore, non-standard AOM driving electronics are required and were specially constructed for the experiments
- Along with the physical requirements for the apparatus, there is also a significant amount of preprocessing of the data required before analysis of the physics in the sample is possible. This manifests itself both in the way in which the data are acquired and in a set of algorithmic routines that are subsequently applied to the data
- As a coherent technique, the relative phase between each beam should ideally be constant or at least change slowly enough that phase-correction or compensation techniques can be applied

This section of the thesis deals with the manner in which the experimental setup was constructed in order to fulfil these requirements.

4.2.1 The acousto-optical modulator

Acousto-optic modulators, AOMs, serve essential functions in this technique, As such, it is worth looking at the physics behind these devices. At heart, an AOM is simply a piece of glass or crystal to which a piezoelectric transducer is bonded. Acoustic waves generated by the transducer produce periodic regions of compression and expansion in the material in which they propagate and hence create a periodic structure in the refractive index with which light can interact. Furthermore, since the light is interacting

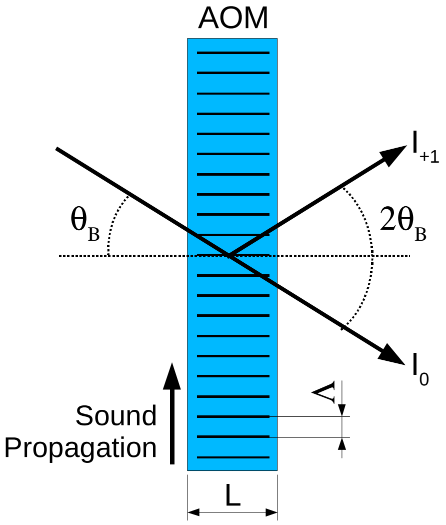

Figure 4.2: *Diffraction in an AOM. Angles are exaggerated for clarity. θ_B: Bragg angle. I_0: zeroth-order (undeflected) beam. I_{+1}: First-order (positive frequency shift) beam. Λ: Acoustic wavelength. L: light-sound interaction length within device.*

with a travelling wave it can be up- or down-shifted in optical frequency through a Doppler shift process.

In practice, this is a somewhat simplified picture. A more accurate model of diffraction by an AOM considers collisions between photons and phonons[GP02]. Figure 4.2 shows the geometry of diffraction for an up-shifted beam. Conserving momentum and energy we have

$$\begin{aligned} \hbar k_{+1} &= \hbar k_0 + \hbar \mathbf{K} \\ \hbar \omega_{+1} &= \hbar \omega_0 + \hbar \Omega \end{aligned} \tag{4.30}$$

where k_0 (ω_0), k_{+1} (ω_{+1}), K (Ω) is the wavevector (frequency) of the incident photon, scattered photon and phonon respectively. The requirement on wavevectors can be seen to be a phase-matching condition. In actual operation K is small compared to k_0, ie $k_0 \approx k_{+1}$. Hence, the angle at which scattering will be optimum is given by

$$\theta_B = \sin^{-1}\left(\frac{K}{2k_0}\right) = \sin^{-1}\left(\frac{\lambda}{2\Lambda}\right) \tag{4.31}$$

with θ_B the Bragg angle. Equivalent equations hold for incident light travelling along the other Bragg-vector and so experiencing a frequency down-shift when scattered. Taking the light-sound interaction length, L, into account, a further condition was found to be necessary before the device will operate in such a Bragg diffraction geometry. The Klein-Cook coefficient, Q, given by

$$Q = \frac{2\pi\lambda L \Omega^2}{n c_{sound}^2} \tag{4.32}$$

where n is the refractive index and c_{sound} the speed of sound in the medium, should be greater than 7.

In practice, we use AOMs made by Intraaction Corp. These are made of crystalline Tellurium Dioxide (TeO_2) and are rated for acoustic driving frequencies centred at

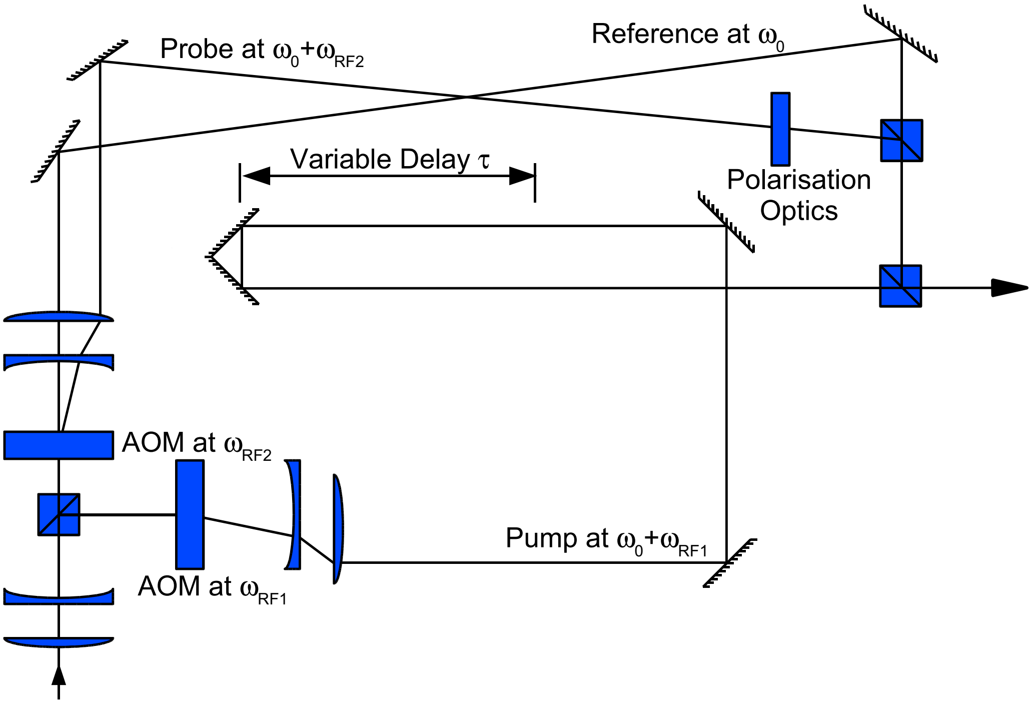

Figure 4.3: *Beam preparation: Input is* $250\,ps$ *pulses from Ti:Saph at* $75.4\,MHz$ *repetition rate.* ω_0 *is the optical centre frequency of the pulses. AOM: Acousto-Optic Modulator.* $\omega_{RF1,2}$ *are the radio-frequencies at which the AOMs are driven.*

$80\,MHz$. With acoustic velocity $c_{sound} = 4260\,ms^{-1}$ in this material and driving them at the centre frequency, a light beam at $800\,nm$ will be diffracted through an angle

$$\theta = 2\theta_B = \lambda\Omega/c_{sound} \approx 0.015\,rad \tag{4.33}$$

4.2.2 Beam preparation

All the data presented here were obtained with an optically pumped titanium:sapphire laser as the light source. It emits pulses of approximately $150\,fs$ width at a rate of $75.4\,MHz$. We then passed the pulses through a pulse-shaper[Man00] which, through a spectral filtering, increased their duration to within a range of $0.25 - 5\,ps$. Finally, we focus through a $50\,\mu m$ pinhole to obtain a clean spatial mode.

At this point we are ready to generate our pump, probe and reference beams. We have chosen to construct a compact, self-contained unit where all three beams are generated and then recombined in the required configuration for imaging onto the sample. This allows us to minimise the optical path along which the beams are spatially separated and so open to relative phase fluctuations induced by environmental effects (air currents and the like). Should significant fluctuations still be present, we also have the option of completely enclosing the preparation stage with plexiglass to further isolate the system.

Figure 4.3 shows the optical layout of our preparation apparatus. A 70:30 non-polarising beamsplitter separates the probe/reference and pump lines. The 30% line will form the pump. It passes through an AOM being driven at $\omega_{RF1} = 79\,MHz$ and the first-order diffracted beam is picked up and a subsequent delay-stage, consisting of a retroreflector mounted on a computer-controlled linear stage, allows us to vary the pump-probe delay τ. The probe-reference delay in our scheme is fixed. The reason for this is discussed below in the section on spectral interferometry.

The other beamline will be used to form the probe and reference beams. Here we pick up both the zero- and first-order diffracted beams from an AOM driven at $\omega_{RF2} = 80\,MHz$. The zero-order will form the reference, while the first-order diffraction forms the probe. We also have the option of controlling the polarisation of the probe to allow cross-polarised pump and probe beams.

Finally, we recombine all three beams in such a way that the pump and probe propagate in the same spatial mode and so will fully overlap at the sample, while the reference propagates in a slightly different direction to the other beams and is imaged on the sample at a point approximately $5\,\mu m$ distant. A telescope (not shown on Figure 4.6) is the final optical element in our beam-preparation; it allows the size of the beams be adjusted to optimally fill the microscope objective with which we perform the final imaging onto the sample. This is necessary to achieve the maximum resolution allowed by this lens.

Not shown in Figure 4.3 are three independent, computer-controlled shutters which allow us to block any combination of beams. This allows the power and spectrum of individual beams be measured along with spectral interference between pairs of beams. The latter is important when characterising the delay between the pump, probe and reference pulses (see below).

4.2.3 Coupling to sample and collection of signal

Figure 4.4 shows the scheme we use for the detection of the signal. The beams from the preparation stage are coupled into the microscope objective mounted in the cryostat by reflection from a beam-sampler. This is a wedged piece of glass which has an anti-reflex coating on one side only. As such it has a nominal coefficient of reflection of 4%(intensity) at the 45^o reflection geometry for which it was designed. While this does mean that over 96% of our excitation power is lost at this one component it nevertheless offers some serious advantages. Excitation power is not an issue for these experiments; we have found that an excitation power of $1\,\mu W$ time-integrated at the sample to be sufficient for FWM. On the other hand, when detecting the signal we wish to avoid losses wherever possible. As we are using a confocal geometry with excitation and detection on the same side of the sample the optics we use to couple in the excitation beam must also be traversed by the signal. Thus we wish to have as high a transmission as possible - something which the beam sampler lends itself to perfectly.

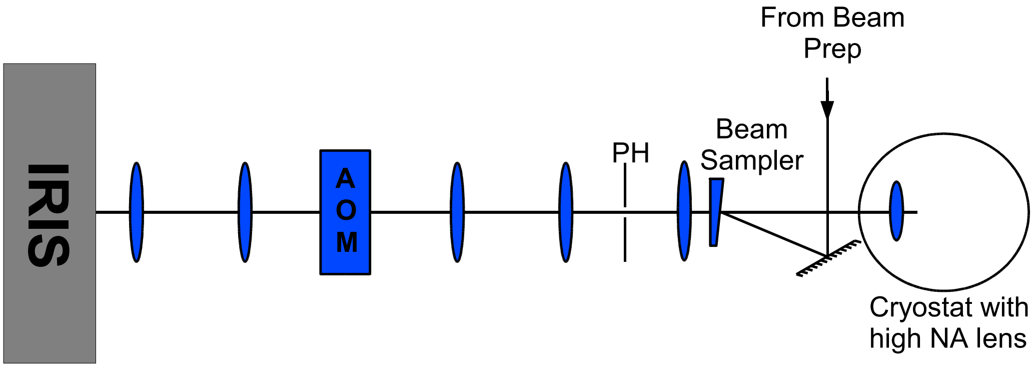

Figure 4.4: *Schematic of detection apparatus. PH: Pinhole AOM: Acousto-Optic Modulator IRIS: 2m imaging spectrometer with liquid-nitrogen cooled CCD*

Imaging of the sample when performing the HFWM is done using a high (0.85) numerical aperture (NA) microscope objective. With the confocal geometry we have both a very high resolution on the sample surface (some hundreds of nanometres depending on our excitation wavelength) and a high collection efficiency. The resolution attainable by a lens can be looked at in terms of the highest order of diffraction which can be admitted by the finite aperture of that lens. For an object of given size, d, the first order will appear at an angle θ given by:

$$\sin(\theta_1) = \lambda/d \tag{4.34}$$

Rearranging, we can see that the resolution will be limited by the angular admittance of the lens. This is taken into account through the *numerical aperture*: $NA \equiv n \sin\alpha$ with n the real part of the refractive index. In this case we use no immersion liquid and thus n is very close to 1 since the atmosphere in the cryostat is helium at a pressure of $200 - 300\,mBar$. Hence,

$$d_{min} = \lambda/n\sin(\alpha) = \lambda/NA \tag{4.35}$$

gives the smallest object, d_{min} which can be resolved by a lens of given NA, with the inverse relationship between size and NA meaning that higher values give *better* resolutions. However, the effect of the refractive index of the sample is to decrease the solid angle detected at the lens. Figure 4.5 shows this clearly. Calculation of the area over which we detect light gives us a geometrical collection efficiency of 7.5%. This does not take into account any reflection at the sample surface and so our actual collection efficiency will be somewhat lower.

The sample is mounted in a helium bath cryostat which allows detection of the FWM at temperatures down to 4K. It is placed on a specially designed holder which allows movement of the sample perpendicular to the optical axis while still in the cryostat and at low-temperatures. Furthermore, the microscope objective lens that is described above is mounted on an x-y-z piezo stage that also fits in the cryostat.

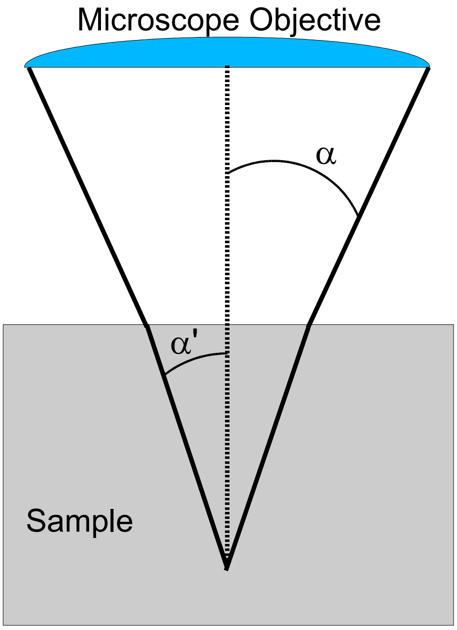

Figure 4.5: *The effect of the refractive index of the sample on the numerical aperture of the imaging lens. α is the angular admittance of the lens, α' is the effective angular admittance of the light emitted from the QD in the barrier of $n = 3.5$.*

This stage was designed and built here in Dortmund[Möl00]. By using a full x-y-z stage we are able to both ensure an optimum focusing of the imaging and to have fine control over the position of the sample. The latter was not only useful as it allowed the optimisation of the signal observed for single transitions, but it also opens up the possibility of mapping the FWM signal in real-space on the sample.

4.2.4 Imaging and spectral interferometry at the AOM

As can be seen in Figure 4.4, the requirements for the implementation of spectral interferometry with the reference and the imaging into the spectrometer lead to a non-trivial solution for the imaging optics. We first image onto a set of pinholes. This is important for two reasons; if gives a fixed excitation position on the sample so that when the photoluminescence is measured we can change between excitation sources with confidence that we are viewing the same region and hence making valid comparisons between PL and FWM signals. Additionally, since we are not performing a directionally-resolved FWM measurement, the pinholes also cut down on the light from non-signal-producing regions and so increase our signal to noise ratio.

Geometrical ray optics were used to calculate the required scheme for the optics. In this methodology matrices represent the optical components involved:

$$D_i = \begin{pmatrix} 1 & d_i \\ 0 & 1 \end{pmatrix} \quad F_i = \begin{pmatrix} 1 & 0 \\ \frac{-1}{f_i} & 1 \end{pmatrix} \tag{4.36}$$

with D_i being distances (through air) over which the light should propagate and F_i being a lens of focal length f. A light ray from the object being imaged is described by a vector $r = (r, \alpha)$ with r being the radial distance from the optical axis and α the angle between the optical axis and the direction of propagation of the ray. Only two dimensions are required since we assume cylindrical symmetry for the lens system, thus lifting the requirement for an azimuthal component. At any given point the resulting vector $r' = (r', \alpha')$ is given by the matrix-multiplication of the matrix representations of the components up to that point. That is, for a system of i lenses of focal length f_i and separated by distances d_i we would have, when using the matrices from Equation (4.36)

$$r' = (D_{i+1} \otimes F_i \otimes D_i \otimes \cdots F_1 \otimes D_1)r$$

where $\otimes$ indicates matrix multiplication and D_1 is the distance from the object to the first lens.

Two special cases for r' present themselves. The first, known as the *near field*, is:

$$r'_{NF} = F'(\alpha, r) \tag{4.37}$$

where $F(r[\alpha])$ denote functions purely depending on $r[\alpha]$. In this case, the spatial information of the object being imaged is preserved in the spatial co-ordinate of r'. We use near field imaging at the pinholes and at the entrance slit to the spectrometer. Note that in reference literature the near field is sometimes referred to as the *object plane*. Finally, unlike the case in scanning near-field optical microscopy (or SNOM), the near field here does not contain information on the evanescent field of the object being imaged.

The second case is *far field* or *k-space* imaging:

$$r'_{NF} = F'(r, \alpha) \tag{4.38}$$

The far field is the image of an object at an infinite distance from the lens (or, alternatively, the image at the focal plane of an object an infinite distance from the lens). The far-field image contains information about the directional intensity of the light emitted by an object. Note that the near- and far-field images are related to each other through a Fourier transform. A property of the far-field that holds importance for our purposes is that the directional component α of light rays in the far-field contains spatial information about the object being imaged. In particular, we can transform a spatial separation of signal and reference beams at the sample into an angular dependence that satisfies our requirements for in-coupling to the AOM at the Bragg angle. Since the angular emission of both beams at the sample is essentially isotropic, imaging in the far field will also ensure the spatial overlap of the two beams at the sample.

The FWM is recovered by Fourier-transform spectral interferometry[LCJ95, DBLJ00] performed on the signal. In this technique we use the interference of the signal with a known reference pulse to recover the field, E_ω, in both amplitude and phase. Since the Fourier transform of E_ω is E_t we are thus able to recover the full, time-dependent electric field with this technique. This opens many possibilities when analysing the data for interesting physical phenomena.

Consider the case of a reference pulse $E_{ref}(\omega, \tau)$ with a fixed delay, τ, relative to the signal interfering with the signal $E_{sig}(\omega)$. The interference signal, $S(\omega, \tau)$ is given

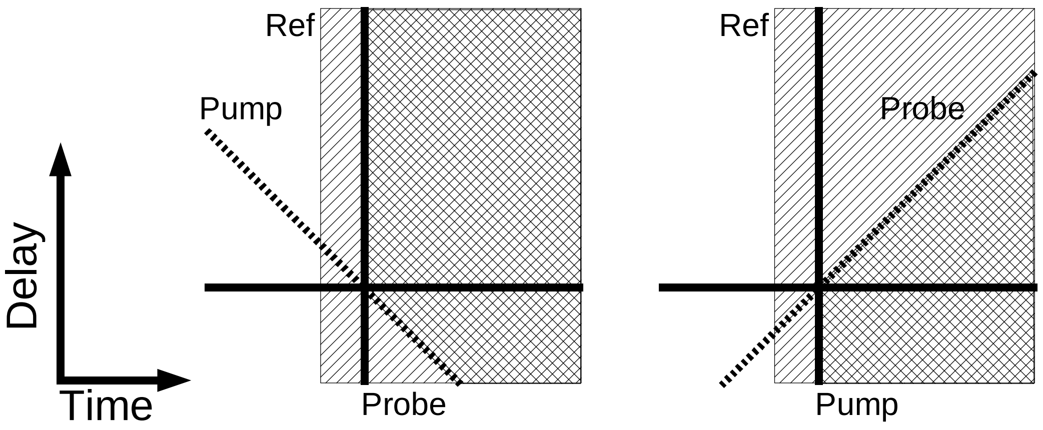

Figure 4.6: *Choice of fixed pump or probe. We are most interested in signals at positive delay (vertical axis). Causality places our signal from interference with the reference at positive times (horizontal axis), shown by the single hatched regions. Cross-hatched regions show times for which we recover signal for a variable pump delay (left) and probe delay (right).*

by

$$\begin{aligned} S(\omega,\tau) &= |E_{ref}(\omega,\tau)+E_{sig}(\omega)|^2 \\ &= |E_{ref}(\omega,\tau)|^2+|E_{sig}(\omega)|^2+2\Re\, E^*_{ref}(\omega,\tau)E_{sig}(\omega) \end{aligned} \tag{4.39}$$

where the final term will be proportional to $\cos(\phi_{sig}(\omega)-\phi_{ref}(\omega))$, the phase difference between the two beams. The terms $|E_{ref}(\omega,\tau)|^2$ and $|E_{sig}(\omega)|^2$ can simply be subtracted as they are the intensities of the reference and signal beams respectively. Removing these terms from Equation (4.39) and writing the reference with delay explicitly as $E_{ref}(\omega)e^{-i\omega\tau}$ we find

$$S(\omega,\tau) = 2\Re\, f(\omega)e^{i\omega\tau};\;\; f(\omega) = E^*_{ref}(\omega)E_{sig}(\omega) \tag{4.40}$$

Fourier transformation of this spectrum leads to

$$F^{-1}S(\omega) = f(t-\tau)+f(-t-\tau) \tag{4.41}$$

Because $S(\omega,\tau)$ is real, the inverse Fourier transform is the sum of two, time reversed components. From the principle of causality it is evident that no signal should be present at times less than τ; there is no emission before excitation of the sample. Overlap of these two components can therefore be prevented by ensuring that τ is greater than any rise time of the signal (for example, due to the finite duration of the excitation pulses). Given this condition, we can recover the positive-time component $f(t-\tau)$ by multiplying the time-domain signal by the Heaviside function, $\Theta(t)$.

The effective time range over which we detect signal is shown schematically in Figure 4.6. For reasons of stability and increased simplicity in alignment and hardware requirements it was decided to fix the position of the reference pulse in time and to use only a single delay-stage. The maximum range over which we can still detect signal will be given by the spectral resolution of our detection scheme and, from the causality

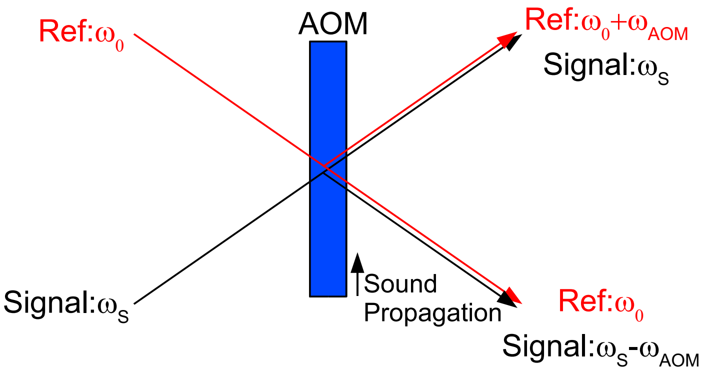

Figure 4.7: *Spectral interferometry as performed in an AOM. ω_0 is the optical centre frequency of the laser, ω_S the centre frequency of the signal and ω_{AOM} the (radio-frequency) driving frequency of the AOM. The sound propagation direction determines whether the signal is up- or down-shifted by the AOM*

condition discussed above, the maximum *time* at which we can still see signal is thus independent of pump-probe delay since the signal will only be present after the probe pulse arrives. The left side of Figure 4.6 shows the effect this has when it is the pump that is moved with changing delay. For positive delays we recover all the signal out to our maximum time while with increasing negative delay we recover progressively less of the signal. The converse is true for a fixed pump and moveable probe - it is the positive delays which are affected by the maximum time at which we can measure. Since we were most interested in signals at positive delay, we fixed the probe position in time. Note that there are cases in which signals at negative delays may be more interesting to observe; two-photon coherences being one example.

At this point we are still working with $f(t-\tau)$, the correlation product between the signal and the reference. It is now necessary to extract the electric field due to the reference from this product. As we do not have a fully characterised reference pulse we will use the flat-phase approximation for the reference

$$E_{ref}(\omega) = \sqrt{I_{ref}}e^{i\theta} \tag{4.42}$$

where I_{ref} is the measured intensity of the reference and θ is a frequency-independent phase factor. The signal's field can then generated from

$$E_{sig}(\omega) = \frac{F[\Theta(t)F_{-1}S(\omega)]e^{-i\omega\tau}}{E_{ref}(\omega)} \tag{4.43}$$

In practice it is also possible to divide through by the reference electric field before the inverse-Fourier transform and we have found it convenient to do so when pre-processing the data.

Figure 4.7 shows the manner in which the AOM is used to mix the signal and reference and thus perform the interferometry. The reference is coupled into the AOM at the Bragg angle corresponding to an up-shift of the optical centre frequency of the pulse, ω_0 by the (radio-frequency) AOM driving frequency, ω_{AOM}. Similarly, the signal, at optical centre frequency ω_S enters the AOM in such a way that it is down-shifted by the AOM. The options for the AOM driving frequency are:

$\omega_{\mathbf{AOM}}$	**Recovers**
ω_{RF1}	Pump
ω_{RF2}	Probe
$\omega_{2\,RF2-RF1}$	Four Wave Mixing

The option of recovering pump or probe interference is useful when calibrating the probe-reference delay and subsequently the zero delay position of the pump translation stage - a beating will be observed with a period in energy of $E_{Beat} = h/\tau$ where τ is the delay between the reference and the beam being interfered. Note that the sign of τ is not implicit in the above relation; it can be easily recovered by placing a small piece of glass in one of the beam paths in order to increase the optical path-length and thus change the observed value of τ.

In order to drive the mixing AOM we use a frequency-mixing unit that was designed and built here in Dortmund. The requirements for this unit are as follows:

- It should supply a stable frequency at ω_{RF1}, ω_{RF2} or $\omega_{2RF2-RF1}$ in order to generate interference with the pump, probe and heterodyne signals respectively. It should also be clean, *i.e.* contain no components at other frequencies.
- The output should be stable in phase in order to avoid loss of fringe contrast through mixing of signals between the two output paths at the AOM.
- We require computerised control over the phase of the output signal in order to effect a π-phase flip between individual integrations on the CCD.
- Control over the amplitude of the signal is also required to optimise the mixing of the signal since the reference and signal lines are of different intensity.

These requirements were met by using the reference outputs of the beam preparation AOM-drivers as inputs to the mixer in order to ensure that we are using the actual values for ω_{RF1} and ω_{RF2}. The actual frequency mixing is done by a pre-amplifier that allows control of the amplitude and phase of the mixed signal. Both may be controlled directly at the device or externally by means of inputs that accept either analogue or digital input. To further improve the quality of our driving-signal we use a Stanford Research Systems model SR844 lock-in amplifier as a narrow pass filter: the reference-in on the lock-in amplifier accepts a reference signal from our mixer. The internal reference oscillator in the lock-in amplifier then generates a signal at our required frequency with a low phase noise and no sidebands. The signal from the internal oscillator is then passed back to our frequency mixer where it is used to generate an output signal of the required amplitude. Finally, a separate power-amplifier of fixed gain is used to amplify this signal to the power level required to run the AOM.

As a result of the mixing in the AOM we have two beams, E_{upper} and E_{lower}. Due to the frequency shift induced by the AOM, these aren't both at the same optical frequency but differ by ω_{AOM}. Taking $\omega_{AOM} = 80\,MHz$ we get an equivalent energy shift of $330\,neV$. As the spectral resolution of the spectrometer at the wavelengths used for detection of the signal is $8\,\mu eV$ and the effective linewidth of the transitions is about $50\,\mu eV$ we can ignore the shift due to the AOM and treat E_{upper} and E_{lower} as being at the same energy.

Finally, due to the fact that there is a π-phase change between successive orders of diffraction from a grating (in this case the acoustic waves in the AOM), the signal recovered from E_{upper} and E_{lower} will also differ from each other by a factor of $e^{i\pi}$. This means that the full signal can be recovered through a simple subtraction of E_{upper} from E_{lower}. This presents a favourable contrast with other geometries for spectral interferometry where either one branch of the interfered signal is discarded or extra optics are required to image the two branches into a single spectrometer. Our method and the fact that the angle between both branches is small ($\approx 0.015\,rad$) allows direct imaging of both components onto different positions of the input slit of the spectrometer. Since we use a two-dimensional CCD-array in the spectrometer we have single shot recovery of the full interferogram and no signal is lost.

4.2.5 Signal detection

As has been already mentioned above, we detect the signal using a home-built high-resolution spectrometer, described in Section 3.1.1. What is important to note is that the spectral dispersion must be calibrated with an accuracy in the second order in wavelength. Small errors in the frequency domain would otherwise lead to a walkoff from the correct calibration when the signal is transformed into the time domain. Since the heterodyne technique uses spectral interferometry to recover the FWM signal we will have the reference superimposed on the signal. As discussed in Section 4.1.4, it is essential to increase the power of the reference relative to the pump and probe in order that we are limited by the shot noise of the laser pulses. This adds to the following requirements for detection by the CCD:

- As a balanced technique, we are required to subtract one integration from another. Hence, it is essential that we are operating in the linear-response regime of the CCD.

- Furthermore, as we are detecting signal from two regions on the CCD, any difference in the response of both regions will need to be compensated.

- We are working with comparatively intense signals (hundreds of nanowatts) at the CCD and so will need short integration times. This means that we will have to choose the CCD readout mode in order to minimise downtime between integrations.

- Conversely, in order to be limited by shot noise, the integration time should be sufficently long that any readout or amplifier noise is dominated by the shot noise.

- While the overall signal intensity is high, the component consisting of the FWM signal is only $5-10\%$ of total intensity at best. Hence, multiple single shots will be required in order to acquire good FWM signal.

As an initial control against non-uniform response of the CCD, a form of doubly balanced detection is used. Rather than directly subtract the two measured signals from one another, sequences of integrations are made in which alternate spectra within a single CCD area differ in phase by π. This is done by changing the driving phase of the AOM in which the spectral interferometry is performed. Hence, we record a sequence of n pairs of interferograms which can then be binned into the final data set. Note that direct binning is often not desirable due to phase-stability considerations. Section 4.2.7 discusses this in further detail.

Labelling the areas on the CCD with indices A, B, the detection scheme can then be given by

$$N \times \begin{cases} I^{+}_{A,B} \\ I^{-}_{A,B} \end{cases}$$

where $I^{+,-}$ indicates the phase angle at which the mixing AOM is driven. Note also that the field generating the detected signal I_A is out of phase with that generating I_B by a factor of π. Figure 4.8 shows the result of such a measurement. It shows the pump-reference interference from multiple $300\,ms$ integrations. The left hand side of the figure shows a subgroup of the phase-flipped pairs collected during the acquired sequence. It clearly shows the effect of changing the AOM phase and the overall π phase difference between the two signals which are detected at the spectrometer. The right hand side shows the spectrum of one of the single shots. Note that the interference (shown in the upper-right plot) does not have full contrast; this is a result of the excess power in the reference beam which allows the measurement to be shot-noise limited. It is also worth noting that the light will not be affected by the change of phase of the acoustic wave in the AOM until the wavefront with the new phase has had time to propagate to the volume in which the interaction occurs. Given an acoustic speed of $4.26\,mm/\mu s$ in this material and the fact that the aperture is $33\,mm$ from the transducer we get a value of $7.75\,\mu s$ which, compared to the $50\,ms+$ integration time, can be considered to be essentially instantaneous.

4.2.6 Data pre-processing

Having acquired the interferograms, it is now necessary to do some initial processing of the data before we are able to analyse them. We first generate a function that corrects for any fluctuation in intensity that occurs on a timescale greater than the acquisition time for a single phase-flipped pair:

$$\begin{aligned} C_{A,n} &= \int [I^{+}_{A,n}(\omega) + I^{-}_{A,n}(\omega)]\, d\omega - 2\int D_A(\omega)\, d\omega \\ C_{B,n} &= \int [I^{+}_{B,n}(\omega) + I^{-}_{B,n}(\omega)]\, d\omega - 2\int D_B(\omega)\, d\omega \end{aligned} \tag{4.44}$$

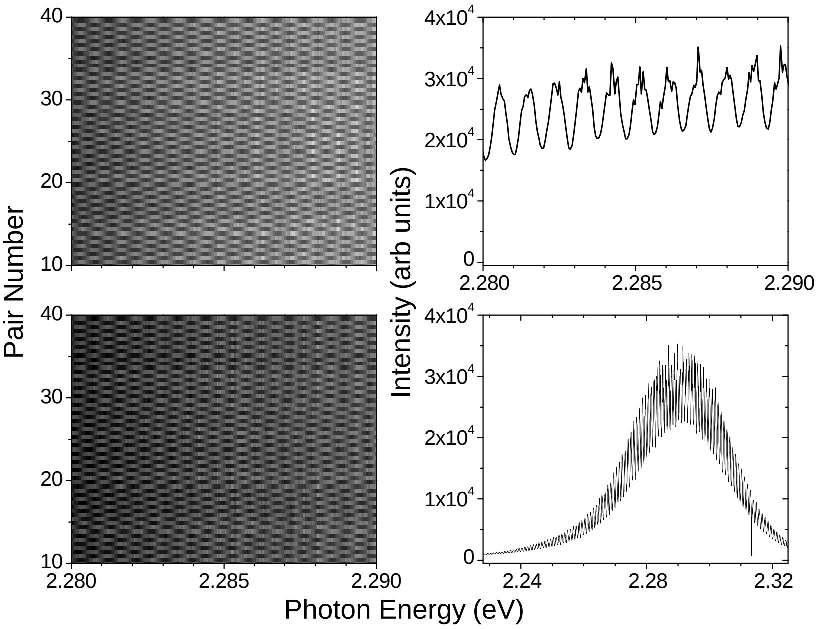

Figure 4.8: *Pump-reference interference as acquired from the spectrometer. Each left hand side plot shows the signal for one area on the CCD. Note the $\pi-$phase change between successive acquisitions and between identical acquisitions on different areas. Right hand side shows sample cuts through one area to show both the reference envelope and the fringes resulting from the* 6 *ps delay between pump and reference*

where $D_{A,B}(\omega)$ is the dark-response of the CCD for the two areas on which we detect the signal and n is the index of the pair within the acquisition. We use these coefficients when doing the subtraction on the individual pairs from each area.

$$\begin{aligned} \Delta P_{A,n}(\omega) &= \sqrt{\frac{C_{A,n}}{C_{B,n}}}^{-1}\left(I^{+}_{A,n}(\omega) - I^{-}_{A,n}(\omega)\right) \\ \Delta P_{B,n}(\omega) &= \sqrt{\frac{C_{A,n}}{C_{B,n}}}\left(I^{+}_{B,n}(\omega) - I^{-}_{B,n}(\omega)\right) \end{aligned} \tag{4.45}$$

We are now ready to perform the final subtraction on the two areas.

$$\Delta I_n(\omega) = \Delta P_{A,n}(\omega) - \Delta P_{B,n}(\omega) \tag{4.46}$$

The result of this process is seen in Figure 4.9. The signal is now fully modulated without any residual background from either the dark-response of the CCD or intensity from the reference beam. As expected, when comparing Figure 4.8 with Figure 4.9, the magnitude of the fringes after the process is four times that of the individual integration.

As was described in the Section 4.2.4, the Fourier transform is an essential mathematical technique in this experiment. Since we are doing digital processing of the data, the Fast Fourier Transform (FFT)[PTVF92] is the preferred method of performing the transform. However, constraints on the algorithm lead to several points which must be addressed to avoid artefacts in the processing[Koc03]. One limitation on the FFT is the requirement of 2^i, $i \in \mathbb{N}$, equally spaced data points. Since the data as measured from the CCD will meet neither of these requirements an interpolation and oversampling is required. We use a linear interpolation and, to avoid any artefacts from the interpolation process which, when transforming from $S(\omega)$ to $S(t)$, will show up as an additional systematic response function at high t, oversample such that we choose a value for i which is one greater than the first power of two which is greater than the number of points in our data-set. This provides an additional bonus in that we move any artefacts from aliasing processes past the end of the region containing the signal.

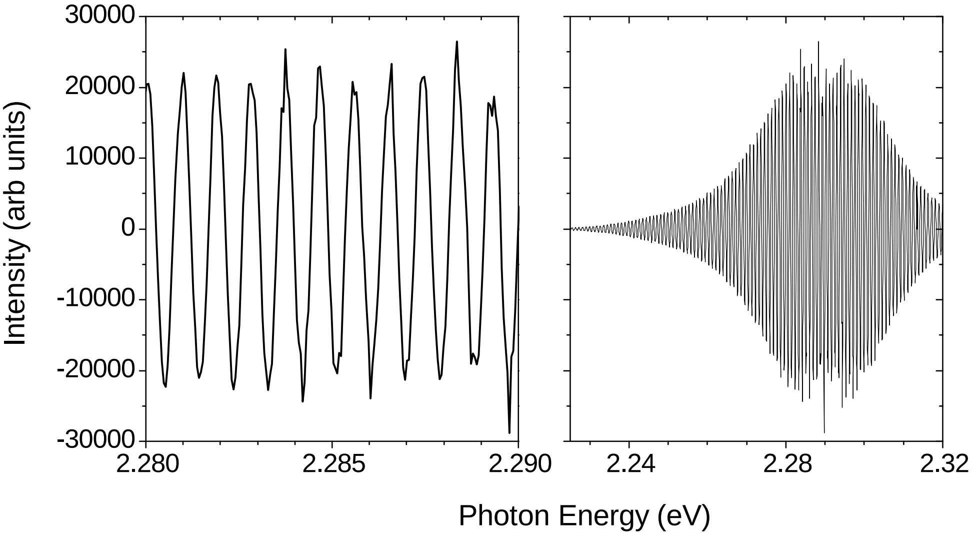

Figure 4.9: *Result of the pair- and area-subtraction. At this point the signal is fully modulated and contains all of the signal from both beams leaving the mixing-AOM. Left: A region about the maximum signal intensity. Right: The signal over the full spectral pulse-width.*

The actual process by which we transform the data is as follows. The area subtracted data $\Delta I_n'(\omega)$, where the prime indicates that it has been oversampled to a linear scaling, is corrected for the reference and Fourier transformed:

$$S_n(t) = F\left(\frac{\Delta I_n'(\omega)}{\sqrt{I_{n,ref}(\omega)}}\right) \tag{4.47}$$

As has been described in Section 4.2.4, the resulting data set contains signal at both positive and negative times. Rather than using the Heaviside function, $\Theta(t)$ as described above, we use an effective Heaviside function $\Theta'(t)$ which, rather than transitioning abruptly from zero to one uses the error function to generate a smooth transition. This avoids any ringing when transforming the data back into the frequency domain. Finally, we down-sample the signal by removing both all data points at negative times and those due to the extra power of two introduced in the oversampling. We now have a data set corresponding to the complex electric field which is of a size which allows fast-Fourier transformation between time- and frequency- domains. However, as indicated by the index n in Equation (4.47), we have not yet fully binned the data. Before doing so we need to correct for any changes in phase between individual spectra. This process, along with a discussion of phase-stability, is described in the next section.

4.2.7 Phase-correction

It is important to minimise drift in the phase of the three beams for the following reason:

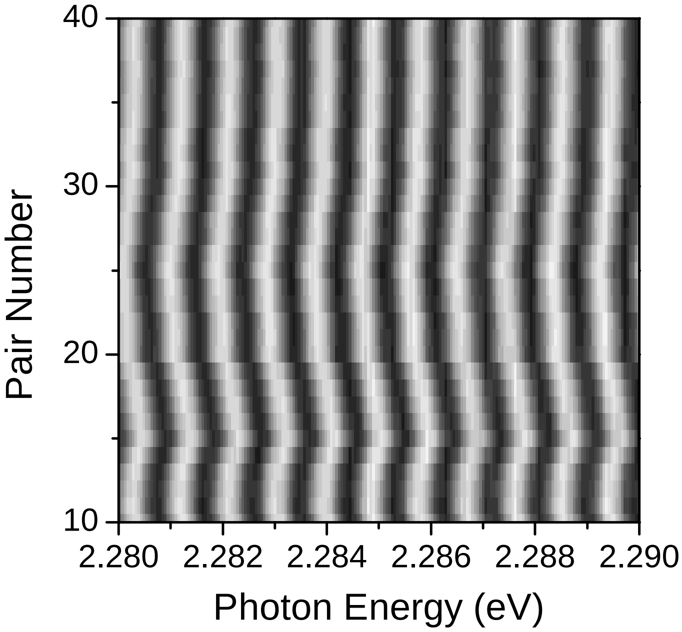

Figure 4.10: *Pump-reference interference showing the effect of phase-drift. The single-shot integration time was 100ms, giving a total time interval for the y-axis of 15s. At this stage in the data-processing both the phase-flipped pairs and the two areas on the CCD have been corrected for dark background and subtracted from one another.*

- While it is ok to have a *fixed* relative phase difference between the three beams, a varying relative phase will reduce the contrast of the signal observed after the interference in the down-mixing AOM.

- An evolution of the absolute phase of the signal over a time-scale that is both longer than our single shot time and comparable to (or shorten than) the time over which we acquire multiple shots will lead to a decrease in contrast when binning the shots.

The first point may be addressed by both enclosing the optical table to avoid the effect of air currents and density changes on the beams and by ensuring that the beams are separated over as short a path length as possible. This will also help with the problems due to the second point. However, we have observed that this is not sufficient to remove all sources of this absolute phase evolution. Figure 4.10 shows the effect of this phase drift on the interference of the pump and reference beams over 15s. Note that this rate of phase drift was only observed when the optical table was completely uncovered. However, over the longer total-integration times required when performing actual measurements, we observed similar drifts in the phase of the signal from single transitions. An advantage of our method is that, since we recover the complex field, we can *correct* the phase of individual shots to an (arbitrary) constant value.

While the correction can be applied in either Fourier domain, we typically correct in the time-domain. The pair-subtracted and dark-corrected data is corrected for the reference, Fourier transformed, resampled and filtered as described above. Since the value of the absolute phase ϕ:

$$A.e^{i\phi} = \int E(t)\,dt$$

is arbitrary, we use the value of ϕ for the first set of binned data as a reference value - we measure the corresponding ϕ_n between the 1^{st} and n^{th} binned sets:

$$I.e^{i\phi_n} = \int E^{'(1)}(t)(E^{'(n)})^*(t)\,dt \tag{4.48}$$

Where $E^{'n}$ is the signal from the n^{th} binned set after a filtering process to remove points that are noise:

$$E^{'}(t) = E(t)\Theta(t),\ \Theta(t) \in [0,1] \tag{4.49}$$

The filtering is necessary because we expect the signal to have a constant phase shift between binned sets whereas the noise will contribute a random phase. Thus, such a filtering will enhance the sensitivity by suppressing times where signal is not present. It was found that a relatively simple filter sufficed wherein we calculated a mean, μ, for the amplitude of the complex data set, discarded the points greater than μ and then twice repeated this process using the new set of data. The final values of μ and the standard deviation, σ, are then used as an indicator of the noise and its error - the filter function $\Theta(t)$ is then generated by:

$$\begin{aligned}\Theta(t) &= 1\ \forall\ |E(t)| > \mu + 3\sigma\\ \Theta(t) &= 0\ Otherwise\end{aligned}$$

Figure 4.11 shows the results of the phase correction. Here we are viewing the signal from Figure 4.10 in the time-domain. Only the real part of the signal is shown, hence the greyscale covers both positive and negative values. The upper plot clearly shows the effect of the varying phase: any naive binning would lose signal as the phase-shifted pairs cancel each other out. In contrast, the lower plot shows the signal after the phase-correction routine has been applied. The data need only be binned before data analysis can begin.

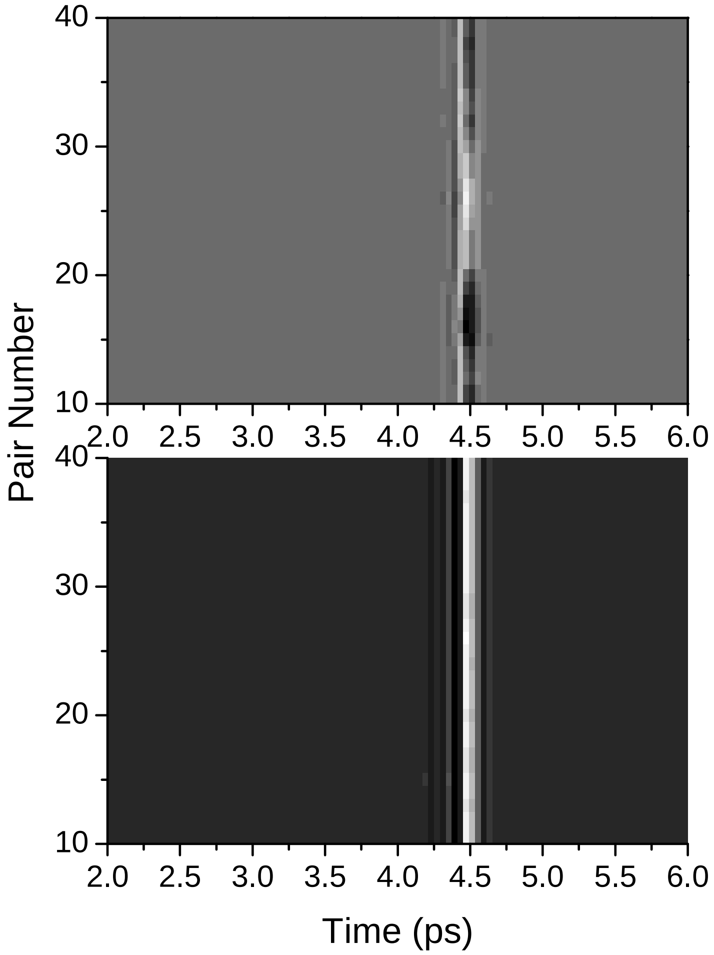

Figure 4.11: *Real part of the time-domain field from Figure 4.10. Black points are negative values of the polarisation, white positive. Top: Before phase-correction. Bottom: Following phase-correction.*

Chapter 5

Heterodyne Four-Wave Mixing: Experimental Results

Having looked at the theory behind our four-wave mixing technique and its implementation, I will now turn to the results we obtained through this method. Unlike Chapter 3, the semiconductor being investigated is not in the II-VI class of compounds. Instead, we performed all the experiments on excitons confined in monolayer fluctuations in GaAs/AlAs, a III-V material, quantum wells (see Section 2.3.2). A brief description of the sample follows.

5.1 The sample under investigation

All measurements presented in this section of the thesis were performed on a sample containing three AlAs/GaAs/AlAs quantum wells of nominal GaAs thickness 10, 7, and $5\,nm$ in the growth direction. The use of binary barrier and well material is important – it reduces the alloy disorder and so ensures that the disorder potential is dominated by the formation of islands that differ in thickness from the surrounding regions by only a single monolayer. We measured FWM in both the 5 and $7\,nm$ thickness wells. The growth and characterisation of such samples is given in detail in Ref. [LJLH00], I will present here only the most notable features of this type of sample. In order to vary the thickness of the well in a uniform manner across the sample, rotation of the sample was stopped during the growth stage of the wells. This resulted in a change of thickness of approximately 20% across the full 2" wafer. Furthermore, at both the upper and lower interface of each well a growth interruption of $120\,s$ was applied in order to tune the correlation length of the monolayer-scale interface fluctuations. Reference [LJLH00] gives a value of $15 - 20\,nm$ for this correlation length by analysing the PL emission from the wells.

The gradient in well thickness results in a useful behaviour whereby changes in the observed PL spectrum allow the determination of regions of interest on the sample.

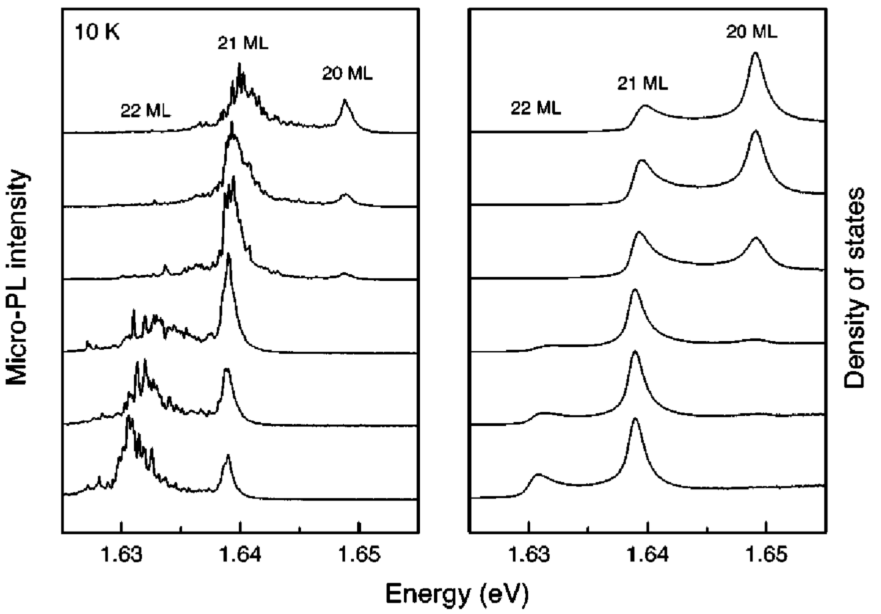

Figure 5.1: *Left: 10-K μPLspectra from a nominally 7 nm thick quantum well, growth-interrupted at both interfaces, at an excitation power of* $0.3\,\mu W$. *The spectra were recorded at 1 mm intervals along the sample surface and are displaced vertically for clarity. The total scan distance corresponds to a thickness change of one monolayer. Right: Optical density of states for the same positions on the sample, determined from 50-K PL spectra and corrected for the temperature dependence of the bandgap. (From Ref. [LJLH00])*

Consider observing PL from a region of uniform thickness and in a confocal geometry (so that distinction between the region of excitation and detection need not be made). A quasi-continuum of states will contribute to the PL, observable as an inhomogeneously broadened peak of approximately $1\,meV$ FWHM. Moving the imaged region along the thickness gradient will result in the appearance of narrow lines at energies below(above) the existing peak when moving in the direction of thickening(thinning). Moving further in this direction will see the narrow lines spread over a wider range of energies and then converge to a single spectral region at a lower(higher) energy corresponding to a monolayer splitting energy. Meanwhile, the initial peak decreases in intensity until disappearing as the new peak reaches its maximum energy. Figure 5.1 shows this effect in a series of PL spectra taken at $1\,mm$ intervals along the thickness gradient. The estimated thickness of the well is given, along with the calculated optical density of states at $50\,K$, corrected for the temperature dependence of the bandgap. The physical basis for this positional dependence is entirely due to the thickness gradient; the gradient manifests itself as regions of uniform thickness of n monlayers which, as the position on the sample is moved to thicker well regions, change to a thickness of $n+1$ monolayers in a region containing an increasing density of islands of this increased thickness.

In order to maximise the signal that was detected at the spectrometer, an anti-reflex coating was applied to the upper surface. This simultaneously increases the amount of light reaching the quantum well and cuts down on the amount of the reference

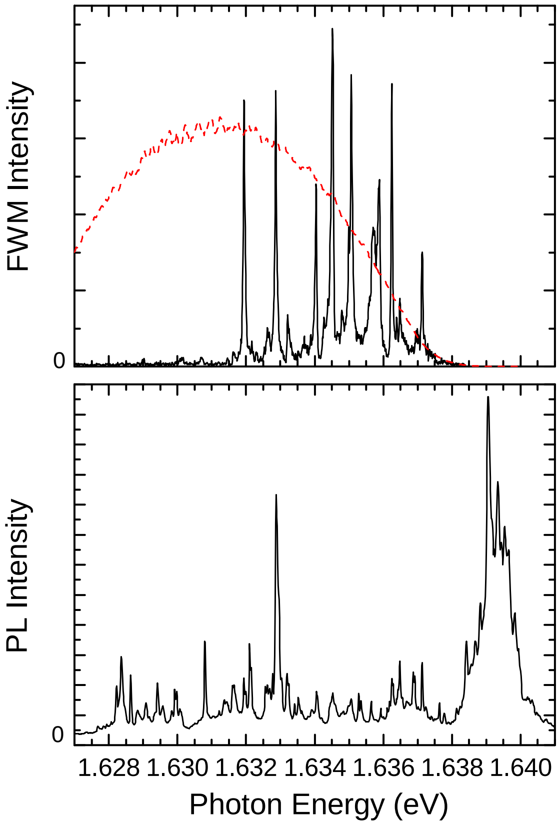

Figure 5.2: *Upper: Spectrally-resolved FWM from an area of* 500 nm *diameter. Included is the excitation laser spectrum. Lower: PL spectrum from same region of sample. Excitation was ArIon laser at* 496 nm.

beam which is reflected from the sample. The anti-reflex coating consisted of a $\lambda/4$ coating of Hafnium Oxide (HfO_2), where the reference wavelength was chosen to be $750\,nm$ ($1.65\,eV$), the measured coefficient of reflection was 5×10^{-4} at $732\,nm$ ($1.69\,eV$) and 5×10^{-3} at $760\,nm$ ($1.63\,eV$).

5.2 Initial characterisation of the FWM signal

Before examining the four-wave mixing signal results in detail, it is important to do some initial characterisation of the signal recovered by the heterodyne technique. The question of whether the sharp lines observable in the spectrally resolved FWM signal are the same states observed in PL measurements is relevant, as is the question of whether the measurements are performed in the third-order regime.

I will begin by comparing the FWM signal to PL experiments on the same sample. Figure 5.2 shows the results of such a comparison. The upper part of the figure is the FWM signal, spectrally resolved from a region of approximately $500\,nm$ in diameter. The pump-probe delay was $\tau = 1\,ps$. Also shown is the excitation spectrum. The lower part of the figure shows the PL spectrum from the same region of the sample. Excitation was with an ArIon laser at $496\,nm$ and a power of $260\,nW$ at the sample. This region on the sample was chosen so that we were measuring in a transition region, as described above, which is dominated by the thinner well thickness but with an

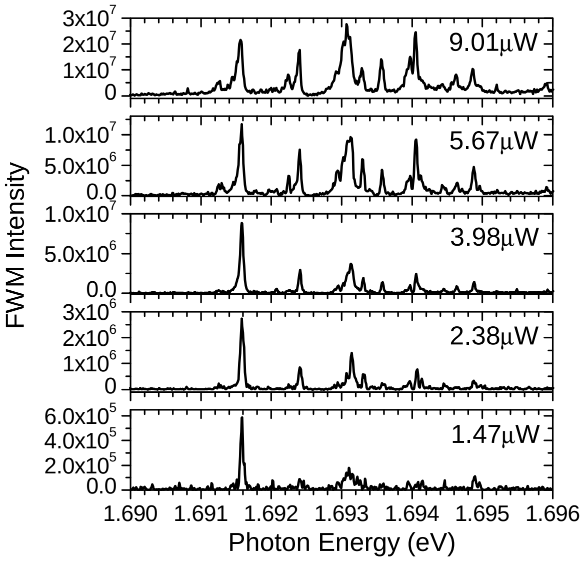

Figure 5.3: *Spectrally-resolved FWM for various excitation intensities. Since FWM is a $\chi^{(3)}$ process, it is necessary to avoid "over-excitation" of the sample and the subsequent introduction of $\chi^{(5)}$ features.*

appreciable number of islands of greater thickness. It is these thicker islands that produce the lines at low energies which are of interest to us. Note, however that there is still an effective quasi-continuum of states in the thinner well, observable as the inhomogeneously broadened peak at $1.639\,eV$ in the photoluminescence spectrum. We chose the excitation spectrum so as not to have a FWM signal which is dominated by these well states.

It can be seen that, apart from the peak at $1.633\,eV$, there is no correlation between the peaks on the FWM spectrum and those in the PL spectrum. The FWM signal strength is determined by the oscillator strength of any given transition, whereas the PL signal will be governed by the trapping and phonon-assisted relaxation of charge carriers into the dots. Hence, we are actually measuring different aspects of the states within the dots with these two techniques; the FWM will show states that couple strongly to the light-field, while the PL is a measure of which states have appreciable populations of excitons in them - an exciton trapped in these states at low temperatures can only relax radiatively and so we will see a PL signal from the state.

As a third-order process, FWM requires high excitation intensities at the sample in order to generate sufficient signal for efficient detection. However, using too high an excitation power can lead to additional complication in the form of a contribution to the signal from fifth-order processes. In order to estimate the non-linear regime in which we are generating the signal, it is necessary to take a series of FWM spectra at varying excitation powers. Figure 5.3 shows the FWM signal at a delay of $0.7\,ps$ for five different intensities. With increasing intensity it is clear that additional FWM lines are present at the highest intensities (*e.g.* a line appears at $1.6952\,eV$ at the highest excitation intensity). However, these may be indicative of higher-order *correlations* (*e.g.* biexciton or triexciton contributions) within the sample and not necessarily of higher-order *polarisation* processes. We must also look for saturation of individual lines. The transition at $1.6916\,eV$, which provides the strongest signal at the lowest intensity shown here, provides an example of such a response which deviates from the

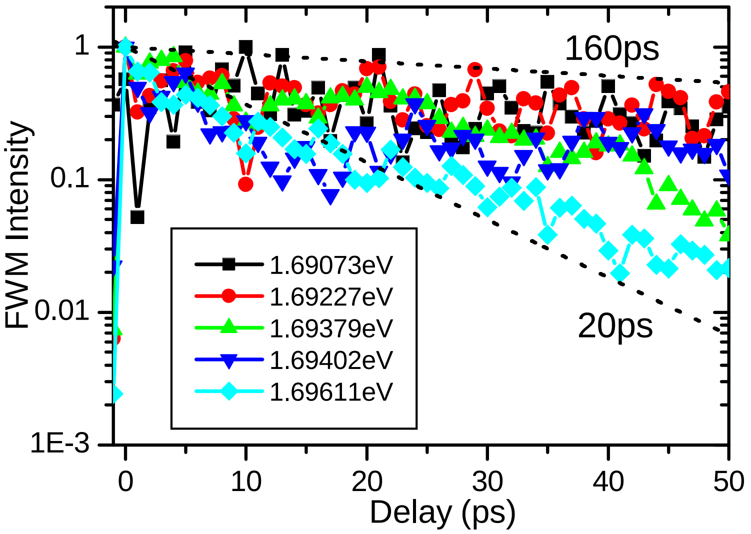

Figure 5.4: *The sample range of decay times for FWM transients observed in this experiment. All data have been normalised. Upper and lower bounds of* 20 *ps and* 160 *ps are given as a guide.*

expected $\propto I^3$ behaviour. While it is not completely clear whether the line is indeed undergoing saturation at the highest intensities, there is some sub-linear response which may indicate the onset of saturation and, hence, a contribution to the FWM signal from $\chi^{(5)}$ processes. To avoid this, we chose to excite the sample at $4\,\mu W$, an intensity free of such complications. With the exception of the Rabi-oscillation experiments described in Section 5.4, where the frequency of oscillations is proportional to the excitation intensity, thus requiring a high intensity to resolve the maximal number of oscillations, we observe the FWM in all the subsequent sections at an excitation intensity equivalent to the $3.98\,\mu eV$ of the current example.

Figure 5.4 shows the intensity of the spectrally-resolved FWM signal for a number of single transitions as a function of delay. This was obtained by taking the spectrally-integrated intensity of the individual transitions, this intensity was then normalised to the maximum intensity for all delays. As can be seen from Equations (4.21), for homogeneously distributed transitions the initial pulse (the pump for positive delays) creates a polarisation that decays as $exp(-2\tau/T_2)$. The FWM signal is observed after the arrival of the probe (for positive delay times), and decays in real time with a decay constant $\tau_{decay} = 2/T_2$, that is, it decays independently of the delay time and with a maximum intensity that depends on the residual polarisation at the time of arrival of the second pulse. Hence, the delay-dependence of the property measured in Figure 5.4 is also $\propto exp(-2\tau/T_2)$. As a guide, monoexponential decays with times of 20 and $160\,ps$ are also given. It can also be seen that there is a greater weight of transitions with decays closer to the $160\,ps$ upper bound. This range of decay constants is in agreement with previous experiments on such interface-fluctuation dots which showed typical linewidths in the range of $20 - 100\,\mu eV$ [BCG+98, SLS+02]

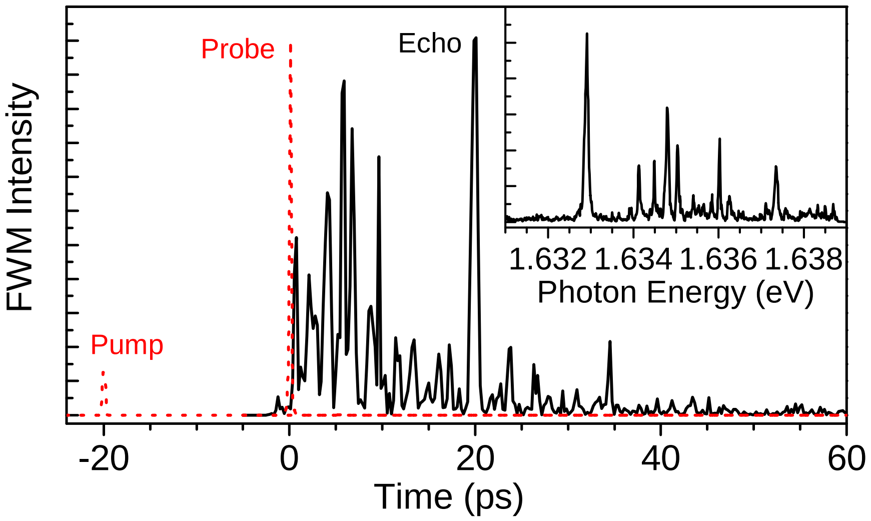

Figure 5.5: *Formation of a photon echo at* $t = \tau = 20\,ps$*. The rephasing of the FWM signal (solid line) at* $t = \tau_d$ *results in the well-known phenomenon of the photon echo. The pump and probe time-resolved signals(dotted line), normalised to the echo intensity, show the delay,* τ_d *of* $20\,ps$*. Inset: The corresponding spectrally-resolved FWM signal showing the multiple states that give rise to the echo.*

5.3 Time-resolved FWM: Polarisation decay and photon echo

As was discussed briefly in Section 4.1.1, measurements on an ensemble of transitions with a distribution of transition energies greater than the individual linewidth will result in the well-known phenomenon of the *photon-echo*. A good treatment of the theory behind this process is given in Reference [AE87]. Consider an ensemble of N individual two-level systems; they will all be in phase immediately after the initial excitation. However, their differences in oscillation frequency will lead to a dephasing of the whole ensemble due to the different rate of phase evolution of each component. Any two of these states with a frequency difference of $\delta\omega$ will return to a phase coherence after a time $\delta t = 2\pi/\delta\omega$. However, for the overall ensemble, such a rephasing becomes increasingly unlikely with increasing ensemble size; $\delta t \rightarrow \infty$. There is thus a rapid dephasing of the system even though there has been no actual energy loss. The electric-field emitted by the system, E_S, is a sum of the fields emitted by the individual two-level systems, E_k, and in the random case will be

$$E_S^{Rand} = \sum_k E_k \propto \sqrt{N} E_k \tag{5.1}$$

Compare this to the field resulting from an in-phase ensemble of oscillators

$$E_S^{Coh} = \sum_k E_k \propto N E_k \tag{5.2}$$

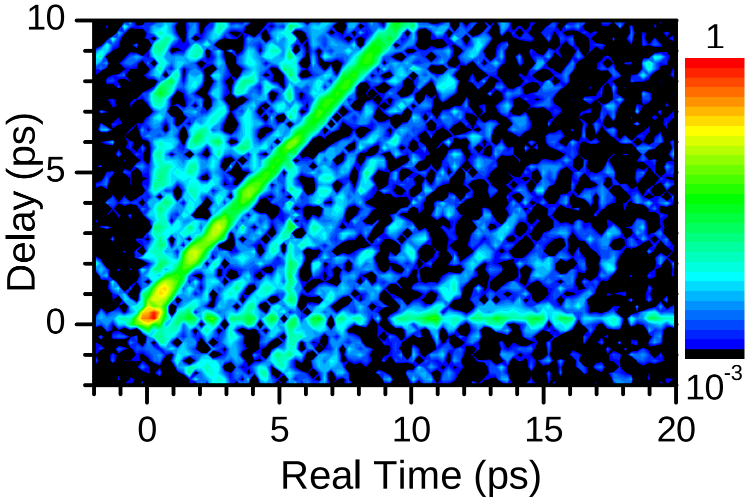

Figure 5.6: *FWM intensity versus delay and time. As is expected, the position of the photon-echo in real-time is given by the pump-probe delay. Also visible here are two types of interference visible as either vertical or diagonal bands of increased signal. See text for details.*

That is, there is a factor of $\sqrt{N}$ in the E-field (N in the intensity) between the two cases. For large ensembles the impact of such a dephasing is thus particularly important. The question then becomes one of whether there is a way of reversing the phase evolution of the individual oscillators in order to effect a rephasing of the overall ensemble. In the four-wave mixing experiment the second pulse flips the polarisation of the ensemble into a phase-conjugate state. The evolution of the individual states is thus reversed - it evolves back towards the initial coherence. If the first pulse arrives at a time $t = 0$ then it is clear that this rephasing will occur at twice the delay time, $t = 2\tau$.

Figure 5.5 shows the photon echo for a delay of $20\,ps$. Note that for all experimental results presented here we take $t = 0$ at the arrival time of the probe. Also shown in this figure are the pump and probe pulses normalised to the echo intensity. The inset shows the narrow spectral lineshape of the individual transitions contributing to the FWM, implying that their individual dephasing occurs on timescales much longer than that shown by the ensemble. As expected, the photon-echo appears at the delay time of $20\,ps$.

The delay-dependence of the photon-echo is shown more explicitly in Figure 5.6. As can be seen clearly, the photon echo moves with delay time. Also of interest in this figure is the fact that the signal range as shown schematically in Figure 4.6(page 56) is readily apparent. At negative delay, there is no signal until the arrival of the *pump*, while for positive delay there is signal as soon as the probe arrives, *i.e.* at $t = 0$ as defined here. This plot also shows that there is still some residual pump-frequency in the driving-signal provided to the mixing-AOM which is manifest in the time-domain plot shown here as a narrow-peak at the pump time. Furthermore, the pump-signal appears to re-enter the plot at $8.5\,ps$. This is an artefact from the spectral interferometry. Since the spectra-interferometry recovers both the signal and its time-mirror and we then filter this total signal to remove the negative-time component, it is clear that signals that are present at a sufficiently negative time will have their time-mirrored component appearing in the positive time domain. The intersection of this 'mirror'-pump with the actual pump signal will occur at the time of arrival of the reference and can be used as an independent confirmation of our reference-delay.

Also visible in this figure are two types of beating structures. The first move with the delay, that is, they have a fixed relationship to the position of the photon-echo. Furthermore, these additional peaks are symmetric in time about the photon-echo. This can be understood by recalling the phase-conjugation requirement for the photon-echo - the evolution of the relative phase of the individual components of the ensemble can be considered to be time-reversed about the position of the photon-echo. Hence the mirrored distribution of peaks. Note that the intensity of the peaks will not be equal about the photon-echo due to the dissipative processes also contributing to the overall dephasing of the ensemble.

The second type of structures visible are independent of delay. These are attributed to transitions that correspond to the same first-order polarisations - for example, exciton-biexciton beats. I will not discuss these beats in further detail -here but will cover them more thoroughly in Section 5.5.

The high spectral resolution of the heterodyne technique offers the possibility of looking at the build-up of the photon-echo with ensemble size; since the time-resolved data can be Fourier transformed to recover the spectrum of the states contributing to the signal we can directly compare the ensemble size with the intensity of the photon-echo compared to the in-phase emission. Figure 5.7 shows both the time- and spectrally-resolved FWM signal from a series of ensembles of increasing size and at a delay of $20\,ps$. Note that, due to the filter applied to the time-resolved data to remove the time-mirrored contribution, the noise at negative times is not apparent here. Included on the time-resolved plot is the ratio of the echo-intensity to the non-coherent emission at that delay. From the discussion above, this ratio is equal to the number of emitters in the ensemble when they can be assumed to be identical. Naturally, this is not necessarily the case for the excitonic transitions we are investigating here, however, a good general agreement between the magnitude of the echo and the number of transitions is evident.

Since we recover the full amplitude and phase of the FWM signal it is possible to look explicitly at the phase evolution of individual transitions within an ensemble and thus observe directly the phase recoherence at the echo time. Figure 5.8 shows just such a rephasing for an ensemble of three transitions at a pump-probe delay of $18\,ps$. The spectrally-resolved signal showing the three major peaks contributing to the overall signal is given on the top right of this figure. There may be some contribution to the signal from the large number of states in the quantum well, visible as a slight increase in the baseline signal at $1.636 - 1.637\,eV$. However, the intensity of the echo supports the notion that any contribution from these states is indeed negligible. To show that the individual transitions do not show an echo behaviour, a Gaussian filter of FWHM $246\,\mu eV$ was applied to the centre position of each transition in the spectral domain and the resulting filtered data was transformed back to the temporal domain to give the free-polarisation decay of the individual peaks. The lower-right plot shows these decays. The phase evolution of the three transitions is given in the upper left. Note that this assumes a phase angle $-\pi \leq \phi < \pi$. With this assumption, the transitions marked by triangles and circles evolve with increasing phase versus time before wrapping around

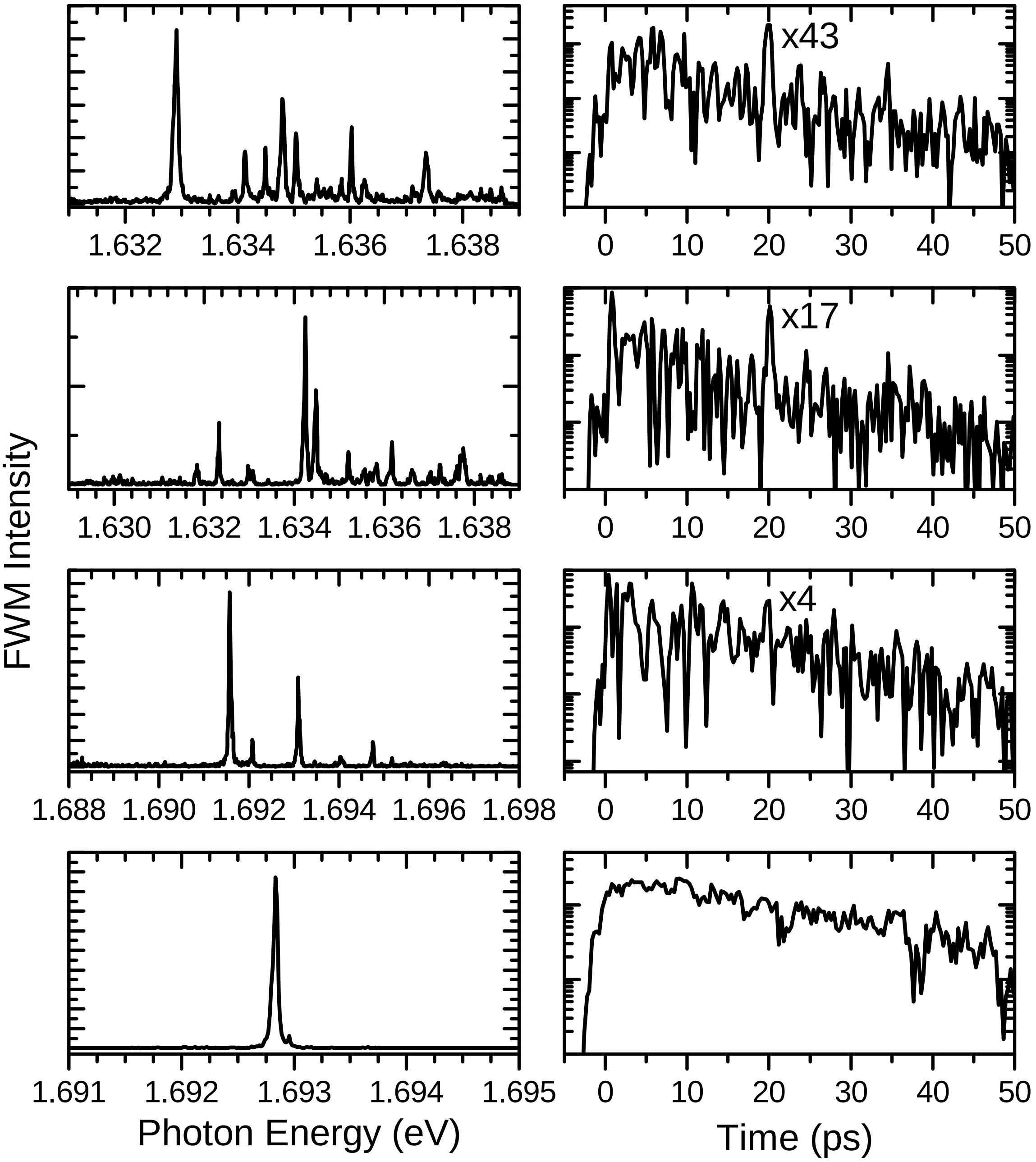

Figure 5.7: *Buildup of the photon echo with ensemble size. All data taken at a delay* $\tau = 20\,ps$. *Also shown on the time-resolved data is the ratio between the photon-echo intensity and the mean of the not in-phase emission to either side of the echo. Note the log-scale on the time-resolved data.*

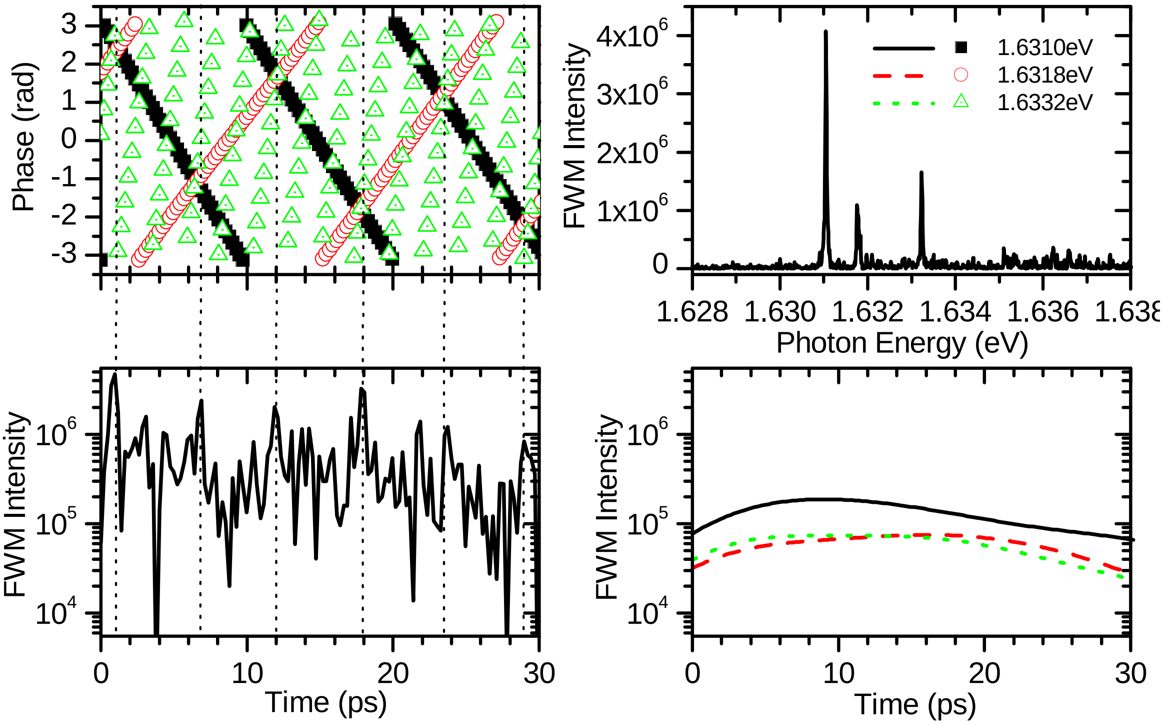

Figure 5.8: *Rephasing as a source of polarisation transients. Upper-left: The phase of the time-resolved FWM signal of the three major peaks contributing to the detected signal. Lower-left: The time-resolved signal of the full ensemble. The photon echo at* $\tau = 18\,ps$ *can be seen to be due to rephasing of the ensemble. Other peaks are also shown to be due to rephasing at other times. Upper-right: Spectrally-resolved signal for this ensemble. Lower-right: Time-resolved decay of the individual transitions. Note that they have a finite intensity when ensemble emission is suppressed.*

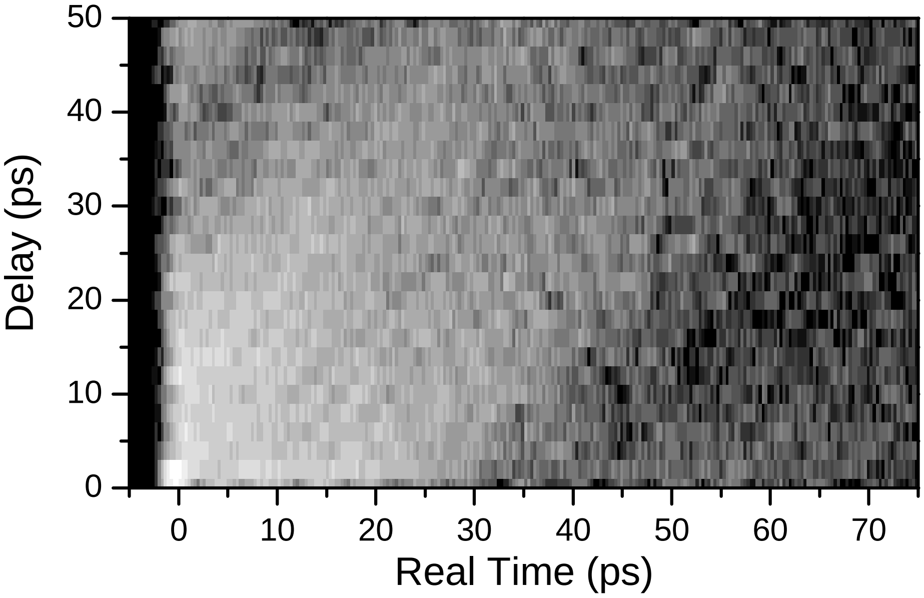

Figure 5.9: *Spectral wandering as a source of ensemble behaviour. Shown here is the delay-dependent, time-resolved signal from a single transition. Spectral wandering creates an apparent stretching of the decay with increasing delay. Logarithmic greyscale over five orders of magnitude.*

to $\phi = -\pi$ at $\phi = \pi$. The transition marked with the squares has a phase that decreases with time. Thus, we are looking for an intersection of the phase evolution of all three transitions at the echo time of $18\,ps$. This is readily apparent and a dotted line links this intersection with the echo in the time-resolved signal of the ensemble given in the lower-left plot. What is also interesting is that secondary rephasings are also observable as additional transient peaks in the time-resolved signal. These secondary peaks have been linked by dotted lines to the relevant rephasings.

So far I have assumed that the individual transitions are purely homogeneously broadened. However, as discussed in Section 3.3 trapping of carriers near to the quantum dots will induce a Stark shift in the energy of the transitions. Since this can be considered to be a random process, it will add a Gaussian broadening to the lineshape. In the time-domain we would see this as a deviation from a mono-exponential decay for individual transitions. Figure 5.4 shows that any such deviation is not readily discernible - the magnitude of any spectral wandering is thus close to, or smaller than, the natural linewidth of the single transitions. However, looking at the time-evolution of a single exciton as a time-ensemble equivalent to the spectral-ensemble of multiple excitonic states leads to an intuitive way to look for the presence of spectral wandering. The narrow spectral range of the wandering will transform into a wide-distribution in time and so will only be apparent when we look at the delay-dependency (for positive delays) of the single transition decay. For a transition unaffected by spectral wandering the dynamics of the decay will be unaffected by change of delay, whereas one affected by spectral wandering will have a dynamics that is the convolution of the homogeneously broadened dynamics with a Gaussian distribution corresponding to the spectral wandering:

$$I_{Wand} \propto e^{-\left(\frac{t}{T_2}\right)-\left(\frac{t-\tau}{T_{Wand}}\right)^2} \tag{5.3}$$

with the delay τ and the characteristic spectral wandering time T_{Wand} which, from the discussion on the lineshape broadening above, will be comparable to T_2. For small delays this will give a polarisation decay that deviates from the monoexponential case because of the Gaussian contribution. At larger delays the shift in the centre position of the Gaussian, given by τ, will have the transition appear to live longer; the Gaussian being sufficiently wide that, unlike with the spectral ensemble case, no discernible drop in emission followed by a rise due to the photon-echo will occur. It is only when $\tau > T_{Wand}$ that such a dip will become apparent. However, since T_{Wand} is approximately equal to T_2 even this contrast between the photon-echo and the initial decay will be washed out due to the overall polarisation decay occurring on these timescales.

Figure 5.9 shows a plot of the time-resolved signal from a single transition versus delay. In order to isolate the single transition the excitation was narrowed spectrally to $1\,meV$. This gives an effective time-resolution of $4\,ps$ and explains the rise of the signal at negative times: $t = 0$ was taken to be at the centre of the probe pulse. The plot clearly shows the 'extension' of the signal in time with increasing delay, as described above. What is also interesting is the appearance of a dip in the signal at $\tau \approx 25\,ps$. Since the dip first appears at $t = 0$ for this delay but the intensity subsequently recovers somewhat (i.e. a cut along the delay axis at $t = 0$ will show a beating effect), the dip in the time-axis for delays $> 50\,ps$ should be attributed to a beating between states with a time constant of $\approx 50\,ps$, i.e. an energy splitting of some $80\,\mu eV$. Section 5.5 discusses such beatings in more detail.

5.4 Rabi-oscillations of single excitonic states

For this section it is worth recalling the vector model of the optical Block equations described in Section 4.1.2

$$\begin{aligned}
\dot{\mathbf{R}} &= \Omega_B \times \mathbf{R} - \underbrace{(u/T_2, v/T_2, (w+1)/T_1)}_{Relaxation\ Terms} \\
\Omega_B &= (-\Omega_R, 0, \eta) \\
\mathbf{R} = (u, v, w) &= (\rho^{\Omega}_{ba} + \rho ab^{\Omega}, i(\rho^{\Omega}_{ba} - \rho^{\Omega}_{ab}), \rho_{bb} - \rho_{aa})
\end{aligned} \tag{5.4}$$

where η is the laser detuning, $\Omega_R = e(\mathbf{r}_{ba} \cdot \epsilon)E_0/\hbar$ the Rabi frequency and, for the purposes of the following section, referring to the component of the Bloch vector $\mathbf{R}$ in the (u, v) plane as the induced polarisation p and the w-component as the population inversion n. Applying an external electric field will thus see the Bloch vector precess about the vector Ω_B. When the field is switched off the vector then relaxes back to the ground state of the system according the relaxation terms given above. Consider an incident field in resonance with the transition ($\eta = 0$ in this case), the Bloch vector

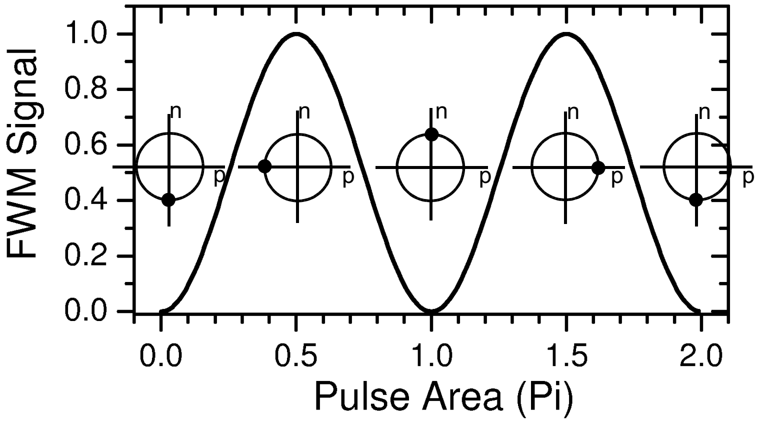

Figure 5.10: *The evolution of the Bloch vector with increasing pulse area. Also shown is the FWM signal, given by the first order polarisation of the system induced by the pump.*

will precess about the u axis by an angle given by the *pulse-area*

$$\Theta(t) = e(\mathbf{r}_{ba} \cdot \epsilon)/\hbar \int_{-\infty}^{t} E(t')dt' \tag{5.5}$$

with this equation it is readily apparent why the quantity Ω_R is termed the Rabi frequency; increasing this term will increase the angle through which the Bloch vector precesses in a given time. It can also be seen that to increase the Rabi frequency it is necessary to either increase the amplitude of the driving field or, should such a thing be possible for a given set of experiments, choose a system with a higher dipole moment, $\mu = e\mathbf{r}_{ba}$. A point that is worth noting here is that when working with light pulses it is almost invariably the intensity, I, that lends itself to measurement. Thus, the pulse area is $\propto \sqrt{I}$.

Figure 5.10 shows both the evolution of the Bloch vector with increasing pulse area and the corresponding FWM signal, proportional to the first order polarisation induced by the pump and thus $\propto \sin^2(\Theta)$, assuming a choice of probe area that is small enough to correspond to a negligible additional precession of the Bloch vector. This is not necessarily always the most interesting case, however it serves to introduce the key phenomena of FWM Rabi oscillations within the two-level model. The system begins in the ground state with $\Theta = 0$ and, upon application of the external field precesses to $\Theta = \pi/2$ where the Bloch vector lies in the polarisation-plane and the FWM signal is maximised. By $\Theta = \pi$ the system is fully inverted, however the projection of the Bloch vector onto the equatorial plane is zero - there is no FWM signal. At $\Theta = 3\pi/2$ the signal is once more maximised and drops to zero again as the system is driven back to its initial state by $\Theta = 2\pi$. It is worth noting that experiments that also examine Rabi oscillations but that measure the population inversion[SLS$^+$01] will measure a signal $\propto \sin^2(\Theta/2)$.

In order to measure Rabi oscillations within the system under investigation here it was necessary to excite a single transtion resonantly. Figure 5.11 shows both the FWM from such a system under broadband excitation and the narrower excitation spectrum used to drive the transition. The choice of a reduction in the spectral width of the excitation to $1\,meV$ allows us to ensure that only a single excitonic state is being

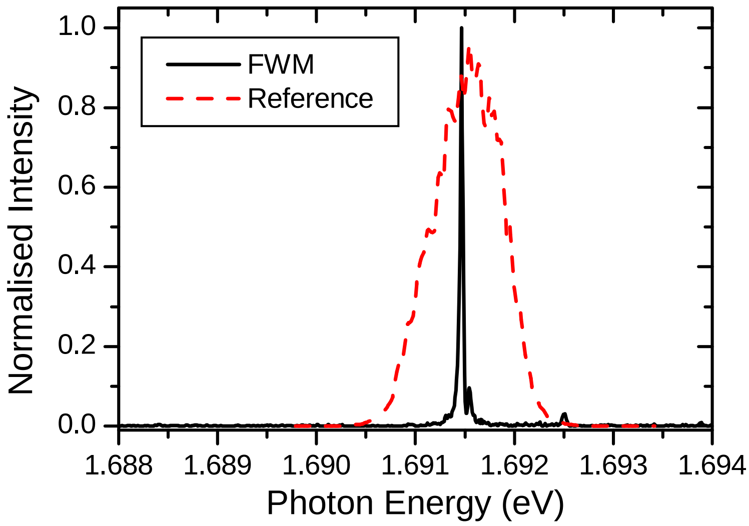

Figure 5.11: *The FWM signal from the single transition used to examine Rabi oscillations in this material system. Also shown is the excitation spectrum used to drive the Rabi oscillations. The FWM signal shown here was obtained with a broader excitation.*

excited. However, this comes at a price, as in the time-domain the excitation is of correspondingly longer duration and so decreases the time-resolution of the measurement. The measurements shown here were thus taken at a delay $\tau = 5\,ps$, close to the earliest delay where there is no longer overlap between pump and probe pulses, so avoiding zero-delay phenomena such as two-photon absorption which will complicate the signal. Since the dephasing of the state occurs on much longer timescales than this delay we can consider this greater delay requirement to be of no further import. The modulation of the intensity of the beam whose area we are scanning is done by varying the driving-power of the relevant AOM at the beam preparation stage. Thus, I will refer to the increase in power at the sample due the modulation of intensity imposed by the AOM as an increase in *pulse area*, whereas the total power impinging on the AOM will be referred to the *input intensity*. The latter cannot be changed dynamically during a pulse-area scan and so it is worth distinguishing between the two cases.

Figure 5.12 shows the Rabi oscillations resulting from a scan of the pump area. The power was $19.5\,\mu W$ in the probe at a pulse area of π. Each data point is the spectrally-integrated FWM intensity for the transition. The solid line is a sinusoidal curve to guide the eye. The response of the system shows well-behaved Rabi oscillations up to a pulse area of approximately $3\pi/2$. At this point there is a decay in the amplitude of the oscillations from the ideal case. We also noticed that increasing the input intensity so as to increase the Rabi frequency was only effective up to the input intensities corresponding to this set of data. Higher input intensities merely caused a greater divergence from expected behaviour of the ideal two-level system. Earlier work exploring Rabi oscillations in the population inversion of excitons in a similar system to the one here[SLS$^+$01] also observed a decay in the amplitude of the Rabi oscillations at high pulse areas. This was attributed to an excitation induced Coulomb scattering (also called *excitation induced dephasing*, EID); an interaction with delocalised excitonic states whose population density is proportional to the laser intensity. This interaction serves to decrease the coherence time of the confined excitonic state being probed and thus leads to the observed decay of the oscillation amplitude. Since

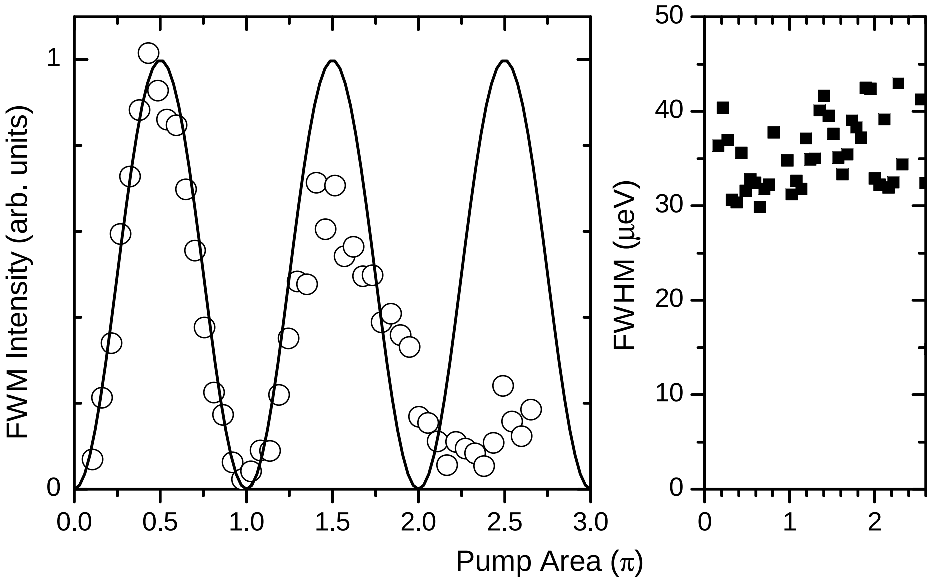

Figure 5.12: *Rabi-oscillations as a function of pump pulse area. Circles: Experiment. Solid line: $Sin^2(\Theta)$. Also shown is the FWHM of the transitions versus pulse area. Excitation induced dephasing would present as an increase in FWHM with increasing pulse area.*

we recover the spectrally-resolved FWM signal, it is possible to directly recover the dephasing dynamics at each pulse-area and so look for signs of such EID. The method chosen here to represent the dephasing is to look at the linewidth of the transition. The right hand side of Figure 5.12 shows the full-width half-maximum of the transition as a function of pulse area. In the case of EID we would expect to see an increase in the linewidth with increasing pulse area. This is not the case, so the observed damping of the oscillation magnitude remains to be explained. The derivation of the Rabi oscillation from the optical Bloch equations assumes a two level system or a system in which the upper level is well-isolated from other levels. However, in this system we have a set of states in the thinner monolayer some $6 - 8\,meV$ from the transition being investigated. Furthermore, the weak localisation within the interface fluctuations means that there could be excited states of the dot separated from the state under investigation that are at energies lower than this range. Thus, the assumption of a two-level system is no longer necessarily a good one. At population inversion it is reasonable to assume that these states become accessible to the carriers excited by the pump and an interaction occurs between the upper state and these additional states. At higher pulse areas the system has sufficient time for an appreciable interaction of these states with the state being probed and thus a reduction occurs in the oscillation amplitude as there is a population transfer to the additional states. It is to the presence of these multi-level states that we attribute the deviation of the Rabi oscillations from the expected behaviour.

In the discussion above, we assumed that the probe-pulse area was low and thus the precession of the Bloch vector was governed by the pump pulse. We have also performed experiments where the *probe area* was scanned. One particularly interesting

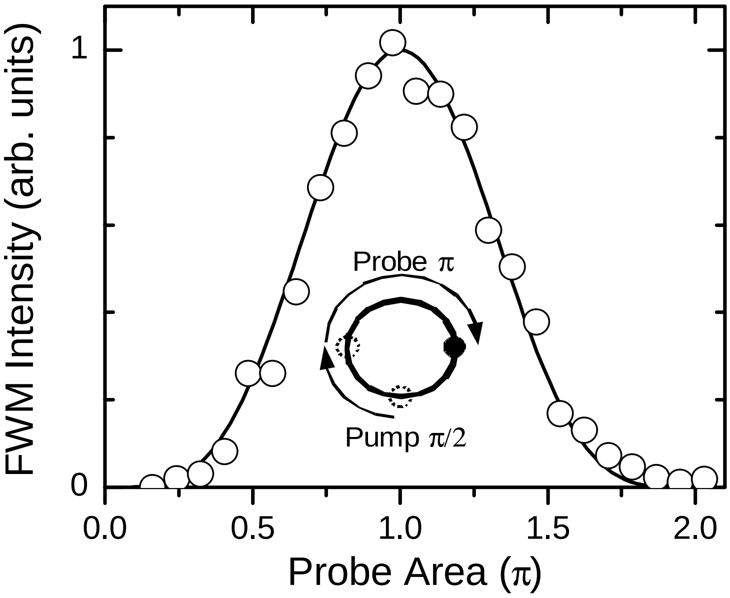

Figure 5.13: *Coherent control of the polarisation of a single excitonic state. The pump pulse-area is set to* $\Theta_{pump} = \pi/2$ *and the probe pulse area is scanned. At a probe pulse area of* $\Theta_{probe} = \pi$ *a maximum in the FWM signal is observed.*

case is shown in Figure 5.13, where the pump pulse area is set to $\Theta_{pump} = \pi/2$ and the probe pulse area is scanned. The pump pulse places the system in a state in the (u, v) plane. The pulse-area dependence will not be the same as in the case where the probe pulse provides only a small perturbation to the Bloch vector. Since we are both integrating over the signal generated by multiple pump-probe pairs and there is a frequency difference between the two pulses (it is a *heterodyne* technique), the vectors $\Omega_{B,Pump}$ and $\Omega_{B,Probe}$ will not have a fixed relationship in the Bloch sphere but will have a range of angles between them over the course the signal acquisition. Hence, there will be no single angle through which the Bloch vector precesses after the application of both pulses but rather a range of positions at which it will end up. However, when the probe area is π, all $\Omega_{B,probe}$ will place the polarisation back in the (u, v) plane - the FWM signal will thus be a maximum at this point. This is indeed the case in Figure 5.13 and is particularly interesting because the implementation of quantum computational devices will require the ability to place a qubit in a given configuration, allow it to evolve (with the possible application of additional pulses further affect the qubit state) and then readout the results of the evolution. While this $\pi/2 - \pi$ rotation is admittedly a special case, it nevertheless gives an initial demonstration of such coherent control of excitonic states.

Until now I have been looking at the case where the excitation is resonant with the transition under investigation. If the excitation is off resonance, the vector Ω_B acquires a component in the w-axis of the Bloch sphere. The precession of the Bloch-vector will now no longer result in a full population inversion, but will reach a maximum value that will still have a polarisation component. The FWM signal that results will thus not fall to zero at a pulse area of π, but will have a residual signal at this point. To examine this off-resonance behaviour we detuned the peak of the reference from the transition energy, using both positive and negative detunings. Figure 5.14 shows the results of such measurements. The peak of reference was detuned in steps of half

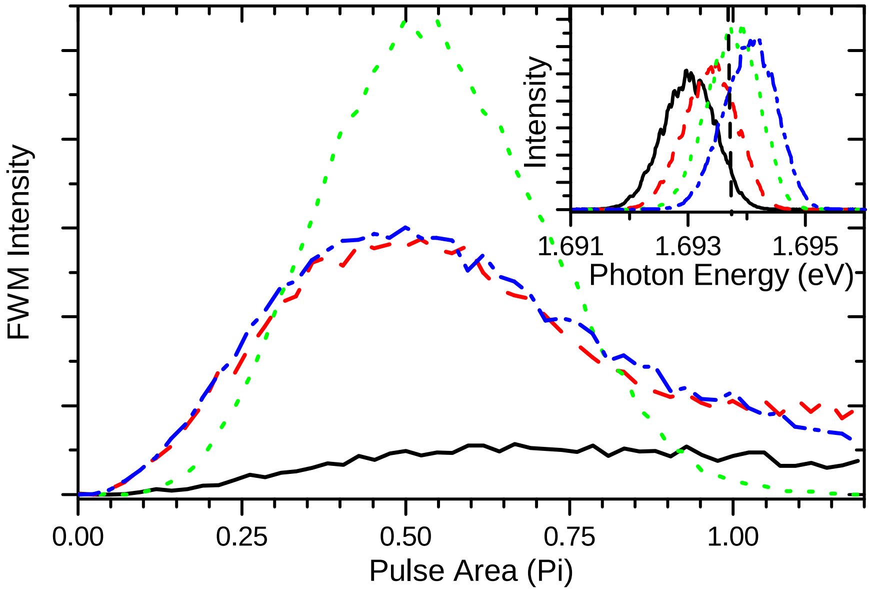

Figure 5.14: *Rabi-oscillations with an excitation offset from the transition frequency. The dashed vertical line on the inset shows the centre-frequency of the transition.*

a half-width-half-maximum (HWHM) from a red-shifted position of one FWHM to a blue-shift of one HWHM about the transition energy. The inset of Figure 5.14 shows the corresponding excitation spectra along with a dashed line showing the spectral position of the state being probed. The pulse-area dependence of the resonant excitation shows the decrease of the FWM signal to zero at $\Theta = \pi$ while, for the two cases off-resonance by half a HWHM the signal does not reach zero at $\Theta = \pi$. Note also the slight shift in the position of the maximum for the latter two cases. The signal from the exciton when excited by a pulse detuned by one FWHM shows more complex behaviour - there is no longer a clear maximum of signal at $\Theta = \pi/2$ and the behaviour at higher pulse is also not clear, it would appear that a greater range of pulse area is required in order to determine whether there is an even lower contrast between the maximum signal and the maximum population inversion or whether it is simply the case that a combination of the high pulse area and the fact that the detuning changes the vector Ω_B means that the simple picture of precession of the Bloch-vector is no longer applicable. If the latter is the case then only a numerical calculation of the third-order polarisation that includes such factors as the explicit time-dependence of the pump and probe pulses will give better insight into the dynamics of the system under such excitation. Note that the initial rise of the of the signal in the two detunings of one HWHM differs from the resonance case. This is another phenomenon that would be clarified with such calculation.

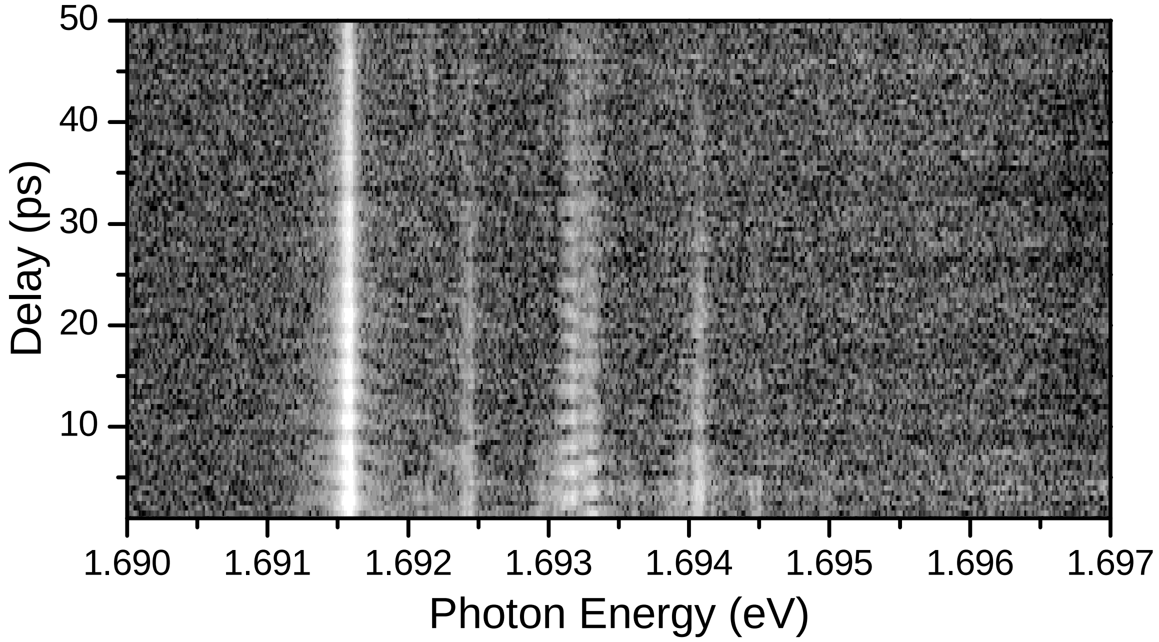

Figure 5.15: *Spectrally resolved FWM as a function of delay. Beats in the amplitude of individual transitions are visible. Plot is logarithmic greyscale over 4 orders of magnitude intensity.*

5.5 Coherent coupling between excitonic states

Examining the response of the system in the spectral domain to changes in delay, τ can reveal coherent couplings between excitonic states. This section explores the way in which the heterodyne technique allows us to recover information on such couplings. Figure 5.15 shows the spectrally resolved FWM versus delay over four orders of magnitude intensity with a logarithmic greyscale. The peak at $1.6915\,eV$ and the two peaks just above $1.693\,eV$ all show clear signs of beating with increasing delay. Such beatings are characteristic of both polarisation beating and of coherent coupling between states and can occur when the spectral width of the excitation is greater than the energetic separation between the two states. Polarisation beating, a delay-time equivalent to the photon-echo, can occur between two states that experience no interaction but that are energetically close. Their emission can thus interfere, something that appears in both the time-resolved and the delay-dependent spectra as a beating in the emission intensity. The method proposed here isolates beating occurring due to coherent coupling and allows easy identification of the states involved in the interaction. Furthermore, for a two states coupled in such a way but otherwise isolated from any other states, the period of the beat gives the energy separation of the two correlated states.

Consider two isolated, two-level systems with transition frequencies ω_1, ω_2 and corresponding transition dipole strengths μ_1, μ_2. An interaction between the two states can couple them. This interaction may be Coulombic, intraband exchange interaction or through the near field of the optical polarisation. Whichever the source, the result-

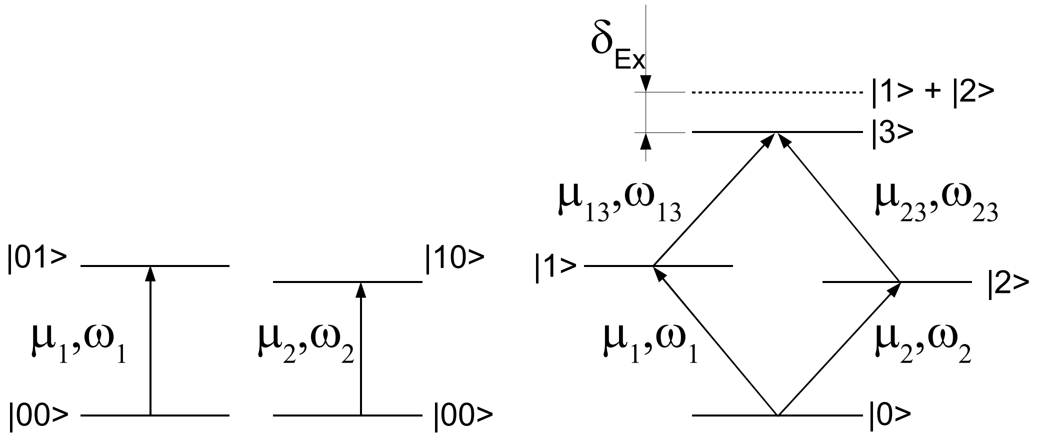

Figure 5.16: *Coherent interactions can couple two independent two-level systems(left). The result can be considered a single, four-level system. An energy renormalisation, δ_{Ex}, for the coherently coupled state is also shown.*

ing coupled system can be considered as a single, four-level system. Figure 5.17 shows such a transformation. In general, the dipole strengths of the first- and third-order resonances are not necessarily identical and any given third order state may be driven by more than one first-order state (i.e. it is possible to have multiply coupled states). To extract the coupling we take advantage of the fact that our measurements return both the amplitude and phase of the third-order signal. Thus, the signal versus delay time is another valid coordinate in which to perform a Fourier transform. Since the beating frequency gives the energy separation, a Fourier transform of the delay-behaviour of the FWM of a single transition will recover all such beating frequencies and hence reveal all states coupled to the one whose delay-dependence we have transformed. One problem with such an approach to recovering information on the coupling is that, unlike the case when transforming the time-resolved FWM data into the frequency domain and vice-versa, there is no fixed phase relationship between subsequent delay times in our data. Instead, we impose a phase relationship onto the data by taking a single peak in the spectral domain and setting the phase at this position to zero for all delays. By applying this phase shift to the full spectrum and not merely to cuts around the peak of interest, we offset all other first-order frequencies versus delay time of all resonances by this first-order frequency. Using the notation $\omega^{(1)}(\omega^{(3)})$ to refer to the transition frequency of first(third)-order, the third order polarisation can be written as

$$P^{(3)}(t>0,\omega) \propto \sum_i exp(i\omega_i^{(1)}\tau) \sum_{ij} A_{ij} exp(i\omega_j^{(3)}\tau) \tag{5.6}$$

where A_{ij} describes the coupling between the first- and third-order states i, j. Fourier transforming $\tau \longrightarrow \Omega$ gives the polarisation as

$$P^{(3)}(\Omega,\omega) \propto \sum_i \delta(\Omega-\omega_i^{(1)}) \sum_{ij} A_{ij} \delta(\omega-\omega_j^{(3)}) \tag{5.7}$$

that is, we recover two-dimensional data set in which uncoupled two-level systems create a line of peaks along $\omega = \Omega$ while coupled states create off-diagonal peaks.

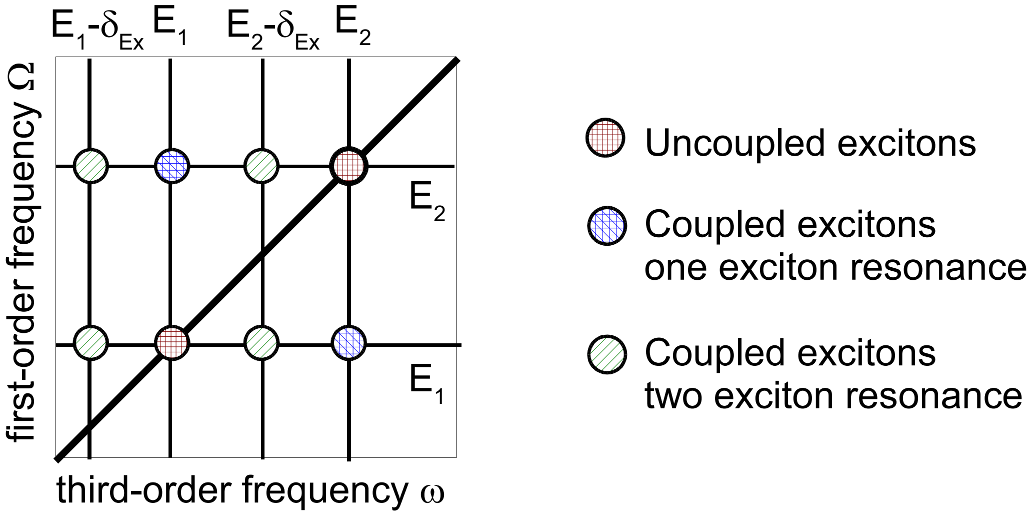

Figure 5.17: *Phase correcting the spectrally-resolved, delay-dependent data and then Fourier transforming along the delay axis recovers coupling between excitonic systems. The relationship between the position of peaks on the resulting 2D-plot and the type of coupling involved is shown here.*

Figure 5.18 shows a schematic of what such a grid would look like with uncoupled excitons appearing along the marked diagonal. The additional peaks along the *vertical* lines E_1 and E_2 appear when there is coupling between the states $|1\rangle$ and $|2\rangle$ involving only a single exciton. The third set of peaks correspond to coupling through the state $|3\rangle$ in Figure 5.16. Note that the renormalisation δ_{Ex} will also appear in the positional information. The actual spectral width of the peaks will be given by their dephasing dynamics, that is, they will not consist of the true delta-functions given in Equation (5.7). Furthermore, while the state contributing to the coupling are clearly identified and while it may be possible after future theoretical work to extract the coupling strength through the intensity of these peaks, the technique appears to give no direct information on the mechanism behind the coupling and so we cannot state whether these are excitonic states within the same dot or whether they are excitons in different dots (so-called quantum dot molecules). Shown in Figure 5.18 are the results of applying this technique to the delay-time plot of Figure 5.15. The peak chosen for the reference phase is that at 1.6916 eV and all energies are calculated as an offset-value from this position. To aid the eye, a line along $\omega = \Omega$ is given, as is a box whose vertices link the reference peak with one of the states to which it is coupled. Note that this reference is also coupled to the state immediately below the one linked by the box. Also of interest is a state at $(\omega = 3.6, \Omega = 0.5)$ which does not correspond to any first-order polarisation and so is a purely third-order state.

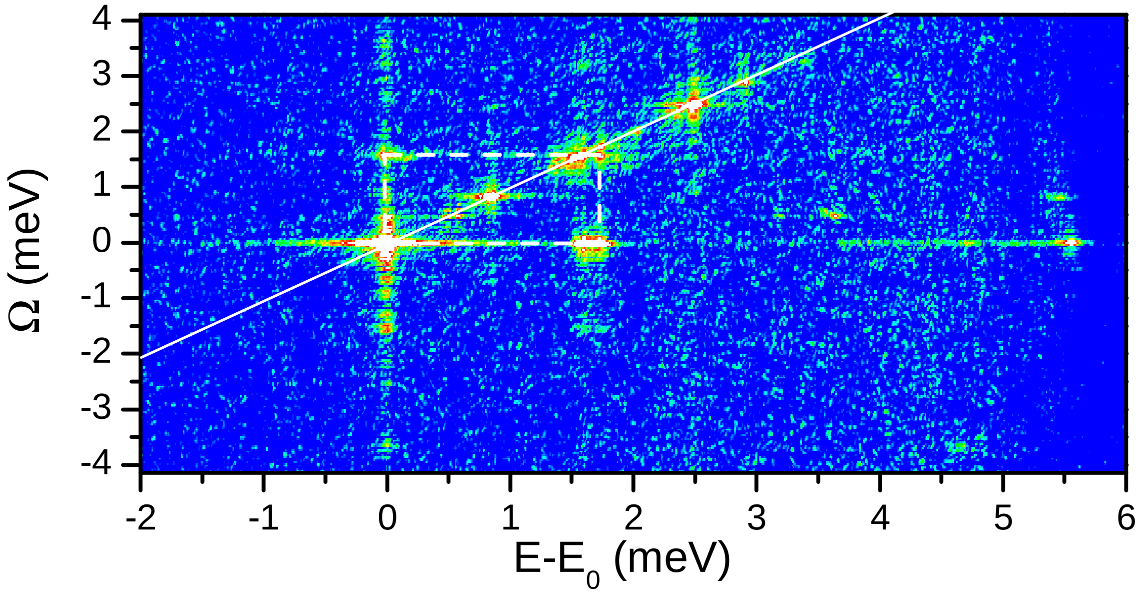

Figure 5.18: *Coherent coupling in a small ensemble of excitonic states. Box links states that are correlated, the diagonal line shows the expected relationship for uncoupled peaks. Also visible are peaks with no corresponding first-order polarisation.*

Part IV

Conclusions

Chapter 6

Summary

Quantum-confined excitonic systems provide a rich source of interesting physics and, due to some of their properties, are also of interest at a more practical level for devices such as lasers, optical amplifiers and, on a longer time-scale, components in quantum information processing. A key area of investigation is the dephasing and depopulation of optically excited carriers. Techniques from both incoherent and coherent spectroscopy were applied to II-VI and III-V samples containing zero-dimensional structures which trapped excitons.

The non-coherent spectroscopy, in which a non-resonant excitation creates a population of carriers which are trapped in the quantum dots and subsequently recombine, was performed with both time- and spectrally-resolved methods on a CdSe/ZnSe quantum dot system. A method for rapidly identifying transitions belonging to a single dot in the presence of emission from multiple dots was developed. This allowed for a rapid characterisation of the sample. The emission was also examined in terms of the excitation-intensity dependence and the linear polarisation of the emitted light in order to identify the nature of the excitonic states contributing to the spectra. Furthermore, the nature of the fine-structure splitting, related to the degree of anisotropy in the shape of the dots, could also be investigated through the linearly-polarised emission from the dots.

Along with general information on the lifetime of excitonic states, the time-resolved photoluminescence measurements gave two very interesting results. Firstly, the observation of the Pauli blocking of the relaxation of the trion to the ground state and hence the lifetime of the spin-flip process as being a rate-limiting step in the overall capture and relaxation to dot ground state was unexpected, if somewhat obvious in hindsight. Secondly, the temperature-dependence of the time-resolved PL for the exciton allowed a measurement of the dark-bright state splitting in this system. While other measurements, such as measuring the PL in a magnetic field, allow optical access to the dark states, it was gratifying to be able to extract this information directly from the refilling from the dark state of the bright exciton state.

In transient FWM experiments, performed here in Dortmund by Borri *et al.*[BLS$^+$01] on III-V materials, a non-Lorentzian lineshape has been reported. Consisting of a spectrally sharp zero-phonon line and a broader background from acoustic-phonon assisted recombination, it led to much theoretical work on the origins of such lineshapes[KAK02, ZR02, FWDK03, ZM04, MZ04]. The use of a high-resolution spectrometer meant that this lineshape was also observed in the CdSe/ZnSe sample under investigation here. By using a model and software developed by *Prof. Roland Zimmermann* we were able to fit the lineshape to good approximation using the material parameters for bulk ZnSe. Furthermore, an estimation of the ratio of the size of the dot in the growth direction to the perpendicular radial dimension was also possible.

The development of a transient four-wave mixing technique which allowed measurement on single dots was the major undertaking of the second half of my PhD. The stability of the resulting system is exemplary; with the inclusion of the phase-correction technique described in Section 4.2.7 we achieved phase stability of the measured signal to within the observed shot noise limit over acquisition times of greater than an hour. It is widely assumed that such stability is only possible in an actively stabilised system.

From the point of view of the physics observed through these measurements, the new technique has also been successful. While the observation of the photon echo can in some sense be thought of as the canonical experiment in FWM, there was an inability to observe the buildup of the echo as a function of ensemble size. The results presented here are thus, to the best of my knowledge, unprecedented.

The ability to control the state of a quantum mechanical system is crucial to the realisation of practical quantum information processing devices. The demonstration of Rabi-oscillations, in particular the $\pi/2 - \pi$ rotation experiment, is a step along the path to incorporating excitons as the qubits in such a device. The behaviour of the oscillations when the excitation is off resonance is interesting on a more fundamental level in that it gives an indication of the limitations of approximating the system as being two-level.

Likewise, any useful quantum processor will require more than one qubit, along with a way to link the qubits so that there is an interaction between their wavefunctions. Extracting information on the coherent coupling between different excitonic states is thus a useful prerequisite to control of the coupling itself.

Chapter 7

Outlook

Perhaps the most important result to come out of this work is the fact that it is possible to do transient FWM on a single quantum dot with a good signal to noise ratio. This opens up a host of possibilities for future studies. Measurements on II-VI materials should allow for a better determination of the effect of spectral wandering on the signal. As was shown in Section 3.3, these materials typically exhibit greater sensitivity to the quantum-confined Stark effect. Since there is also a greater oscillator strength of the material, we are optimistic that experiments on such systems will also be successful.

Of much interest in recent times is the possibility of using the spins of the charge carriers to form devices with novel properties. Dubbed 'spintronics', this field is particularly interesting from an optics point of view, since the optical selection rules for semiconductors with a zinc-blende structure allow direct selection of the spin of the exciton through appropriate choice of the circular polarisation of the excitation laser.

With regard to the technique, an extension to a non-degenerate method whereby the pump and probe beams are no longer the same wavelength (ignoring the AOM offset) will allow exploration of the effect on states non-resonant to the pump. Additionally, a third beam may be added, changing the configuration from the $P^{(3)} \propto E_2 E_2 E1^*$ described here to $P^{(3)} \propto E_3 E_2 E1^*$. A good discussion of the consequences of such a change may be found in Reference [Sha96].

Finally, as has been often mentioned in this work, the attempt to develop a quantum computer is exercising the minds of many researchers throughout the globe. While the payout, should the device be achieved, will be enormous, what is also often overlooked is the fact that *en route* many useful techniques will need to be developed and deployed that will doubtless find many other applications. The fact that the HFWM described here provided both physical insights into the processes at work in the material systems and may also be thought of as providing coherent control over a rudimentary qubit is but one example of such a dichotomy. These are interesting times to be an experimental physicist.

Appendix

Published Papers and Conference Submissions

Note: In the case of conferences, the author in **boldface** presented the work.

1. *Trion, biexciton and exciton dynamics in single self-assembled CdSe quantum dots* B. Patton, W. Langbein, U. Woggon Phys. Rev. B **68**, 12 5316 (2003)
2. *Heterodyne Four-Wave Mixing on Single Excitonic States* **B. Patton**, W. Langbein, and U. Woggon, EQUONT-3, Cambridge, UK, 2004
3. *Transient four-wave mixing of single exciton states: Exciton-exciton interaction and Rabi oscillations* B. Patton, **W. Langbein**, and U. Woggon, ICPS-27, Flagstaff, USA, 2004
4. *Trion and exciton dynamics in epitaxially grown CdSe/ZnSe quantum dots* **B. Patton**, W. Langbein, and U. Woggon, MRS Fall Meeting, Boston, USA, 2003
5. *Excitonic complexes in II-VI quantum dots: Population dynamics and homogeneous line broadening* B. Patton, W. Langbein, and **U. Woggon**, NOEKS, Karlsruhe, Germany, 2003
6. *Non-Lorentzian lineshapes in the emission spectra of single self-assembled CdSe/ ZnSe quantum dots* **B. Patton**, W. Langbein, and U. Woggon, DPG Spring Meeting, Dresden, Germany, 2003
7. *Dynamics of excitons, multiexcitons and trion states in II-VI quantum dots* **B. Patton**, W. Langbein, and U. Woggon, ICPS-26 Proceedings 2002
8. *Time-resolved spectroscopy on single CdSe/ZnSe self-assembled quantum dots* **B. Patton**, W. Langbein, and U. Woggon, DPG Spring Meeting, Regensburg, Germany, 2002
9. Participant: 275 WE-Heraeus Seminar Hardware Concepts for Quantum Computing Bad Honnef, Germany, 2002

Bibliography

[AE87] Leslie C. Allen and Joseph H. Eberly, *Optical resonance and two-level atoms*, Dover Publications, 1987.

[BCG+98] N. H. Bonadeo, Gang Chen, D. Gammon, D. S. Katzer, D. Park, and D. G. Steel, *Nonlinear nano-optics: Probing one exciton at a time*, Phys. Rev. Lett. **81** (1998), 2759.

[BF73] P. J. Brown and J. B. Forsyth, *The crystal structure of solids*, Edward Arnold, 1973.

[BF02] M. Bayer and A. Forchel, *Temperature dependence of the exciton homogeneous linewidth in* $In_{0.60}Ga_{0.40}As/GaAs$ *self-assembled quantum dots*, Phys. Rev. B **65** (2002), 041308(R).

[BGL99] D. Bimberg, M. Grundmann, and N. N. Ledentsov, *Quantum dot heterostructures*, John Wiley and Sons, Chichester, 1999.

[Bha97] Rameshwar Bhargave (ed.), *Properties of wide-bandgap II-VI semiconductors*, INSPEC, 1997.

[BKM00] L. Besombes, K. Kheng, and D. Martrou, *Exciton and biexciton fine structure in single elongated islands grown on a vicinal surface*, Phys. Rev. Lett. **85** (2000), 425–428.

[BKMM01] L. Besombes, K. Kheng, L. Marsal, and H. Mariette, *Acoustic phonon broadening mechanism in single quantum dot emission*, Phys. Rev. B **63** (2001), 155307.

[BKMM02] L. Besombes, K. Kheng, L. Marsal, and H. Mariette, *Few-particle effects in single CdTe quantum dots*, Phys. Rev. B **65** (2002), 121314(R).

[BLS+01] P. Borri, W. Langbein, S. Schneider, U. Woggon, R. L. Sellin, D. Ouyang, and D. Bimberg, *Ultralong dephasing time in InGaAs quantum dots*, Phys. Rev. Lett. **87** (2001), 157401.

[BOS+02] M. Bayer, G. Ortner, O. Stern, A. Kuther, A.A. Gorbunov, A. Forchel, P. Hawrylak, S. Fafard, K. Hinzer, T.L. Reinecke, S.N. Walck, J.P. Reithmaier, F. Klopf, and F. Schäfer, *Fine structure of neutral and charged* *excitons in self-assembled In(Ga)As/(Al)GaAs quantum dots*, Phys. Rev. B **65** (2002), 195315.

[BWS$^+$99] G. Bacher, R. Weigand, J. Seufert, V. D. Kulakovskii, N. A. Gippius, A. Forchel, K. Leonardi, and D. Hommel, *Biexciton versus exciton lifetime in a single semiconductor quantum dot*, Phys. Rev. Lett. **83** (1999), 4417–4420.

[CC76] J.R. Chelikowsky and M.L. Cohen, *Nonlocal pseudopotential calculations for the electronic structure of eleven diamond and zinc-blende semiconductors*, Phys. Rev. B **14** (1976), 556–582.

[CGL$^+$96] M. Chamarro, C. Gourdon, P. Lavallard, O. Lublinskaya, and A.I. Ekimov, *Enhancement of electron-hole interaction in CdSe nanocrystals: A quantum confinement effect*, Phys. Rev. B **53** (1996), 1336–1342.

[DBLJ00] C. Dorrer, N. Belabas, J.-P. Likforman, and M. Joffre, *Spectral resolution and sampling issues in fourier-transform spectral interferometry*, J. Opt. Soc. Am. B **17** (2000), 1795–1802.

[Ein05] Albert Einstein, *On a heuristic point of view concerning the production and transformation of light*, Annalen der Physik **17** (1905), no. 132.

[ENG96] S. A. Empedocles, D. J. Norris, and Bawendi M. G., *Photoluminescence spectroscopy of single CdSe nanocrystallite quantum dots*, Phys. Rev. Lett. **77** (1996), no. 18, 3873–3876.

[FCF$^+$03] I. Favero, G. Cassabois, R. Ferreira, D. Darson, C. Voisin, J. Tignon, C. Delalande, G. Bastard, Ph. Roussignol, and J. M. Gérard, *Acoustic phonon sidebands in the emission line of single InAs/GaAs quantum dots*, Phys. Rev. B **68** (2003), 233301.

[Fey82] Richard P. Feynman, *Simulating physics with computers*, Int. J. Th. Phys. **21** (1982), no. 6/7.

[FP03] A. Franceschetti and S. T. Pantelides, *Excited-state relaxations and Franck-Condon shift in Si quantum dots*, Phys. Rev. B **68** (2003), 33313.

[FVH57] R. P. Feynman, F. L. Vernon, and R. W. Hellwarth, *Geometrical representation of the Schrödinger equation for solving maser problems*, J. App. Phys. **28** (1957), no. 1, 49–52.

[FWDK03] J. Förstner, C. Weber, J. Danckwerts, and A. Knorr, *Phonon-assisted damping of Rabi oscillations in semiconductor quantum dots*, Phys. Rev. Lett. **91** (2003), 127401.

[FWFZ98] A. Franceschetti, L. W. Wang, H. Fu, and A. Zunger, *Short-range versus long-range electron-hole exchange interactions in semiconductor quantum dots*, Phys. Rev. B **58** (1998), R13 367–370.

[FZ00] A. Franceschetti and A. Zunger, *Pseudopotential calculations of electron and hole addition spectra of InAs, InP, and Si quantum dots*, Phys. Rev. B **62** (2000), 2614–2623.

[GHLW99] F. Gindele, K. Hild, W. Langbein, and U. Woggon, *Phonon interaction of single excitons and biexcitons*, Phys. Rev. B **60** (1999), R2157–R2160.

[GMW$^+$98] F. Gindele, C. Märkle, U. Woggon, W. Langbein, J. M. Hvam, K. Leonardi, K. Ohkawa, and D. Hommel, *Exciton localisation in CdSe islands buried in a quantum well of* $Zn_{1-x}Cd_xSe$, Journal of Crystal Growth (1998), no. 184/185, 306–310.

[GP02] D. T. Gies and Ting-Chung P., *Measurements of acoustic radiation pattern in an acousto-optic modulator*, IEEE Conference, 2002.

[GR] N. C. Greenham and D. R. Richards, *Lecture notes on optoelectronics*, Part III Physics, Cambridge University.

[GSS$^+$96] D. Gammon, E. S. Snow, B. V. Shanabrook, D. S. Katzer, and D. Park, *Fine structure splitting in the optical spectra of single GaAs quantum dots*, Phys. Rev. Lett. **76** (1996), 3005–3008.

[GVG$^+$97] R. Grousson, V. Voliotis, N. Grandjean, J. Massies, M. Leroux, and C. Deparis, *Microroughness and exciton localization in (Al,Ga)As/GaAs quantum wells*, Phys. Rev. B **55** (1997), 5253–5258.

[GWL$^+$99] F. Gindele, U. Woggon, W. Langbein, J. M. Hvam, K. Leonardi, D. Hommel, and H. Selke, *Excitons, biexcitons, and phonons in ultrathin CdSe/ZnSe quantum structures*, Phys. Rev. B **60** (1999), 8773–8782.

[HLIR92] K. L. Hall, G. Lenz, E. P. Ippen, and G. Raybon, *Heterodyne pump–probe technique for time domain studies of optical nonlinearities in waveguides*, Opt. Lett. **17** (1992), 874–876.

[IBK$^+$95] M. Illing, G. Bacher, T. Kümmell, A. Forchel, T. G. Andersson, D. Hommel, B. Jobst, and G. Landwehr, *Lateral quantization effects in lithographically defined CdZnSe/ZnSe quantum dots and quantum wires*, App. Phys. Lett. **67** (1995), 124–126.

[IM96] M. Ikezawa and Y. Masumoto, *Stochastic treatment of the dynamics of excitons and excitonic molecules in CuCl nanocrystals*, Phys. Rev. B **53** (1996), 13694.

[Jon03] Fredrik Jonsson, *Lecture notes on nonlinear optics*, Royal Institute of Technology, Stockholm, Sweden, 2003.

[KAK02] B. Krummheuer, V. M. Axt, and T. Kuhn, *Theory of pure dephasing and the resulting absorption line shape in semiconductor quantum dots*, Phys. Rev. B **65** (2002), 195313.

[KBW+99] V. D. Kulakovskii, G. Bacher, R. Weigand, T. Kümmel, A. Forchel, E. Borovitskaya, K. Leonardi, and D. Hommel, *Fine structure of biexciton emission in symmetric and asymmetric CdSe/ZnSe single quantum dots*, Phys. Rev. Lett. **82** (1999), 1780–1783.

[KKR+94] Y. D. Kim, M. V. Klein, S. F. Ren, Y. C. Chang, H. Luo, N. Samarth, and J. K. Furdyna, *Optical properties of zinc-blende CdSe and* $Zn_xCd_{1-x}Se$ *films grown on GaAs*, Phys. Rev. B **49** (1994), 7262–7270.

[Koc03] G. Kocherscheidt, *Speckle analysis and spectral interferometry on gallium arsenide single quantum wells*, Ph.D. thesis, Universität Dortmund, 2003.

[KSH+93] R. F. Kopf, E. F. Schubert, T. D. Harris, R. S. Becker, and G. H. Gilmer, *Modification of GaAs/AlGaAs growth-interrupted interfaces through changes in ambient conditions during growth.*, J. Appl. Phys. **74** (1993), 6139–6145.

[KSHB91] R. F. Kopf, E. F. Schubert, T. D. Harris, and R. S. Becker, *Photoluminescence of GaAs quantum wells grown by molecular beam epitaxy with growth interruptions*, Appl. Phys. Lett. **58** (1991), 631–633.

[LCJ95] L. Lepetit, G. Chériaux, and M. Joffre, *Linear techniques of phase measurement by femtosecond spectral interferometry for applications in spectroscopy*, J. Opt. Soc. Am. B **12** (1995), 2467–2474.

[LGX99] Yong-qing Li, Dorel Guzun, and Min Xiao, *Sub-shot-noise-limited optical heterodyne detection using an amplitude-squeezed local oscillator*, Phys. Rev. Lett. **82** (1999), 5225–5228.

[LHO+97] K. Leonardi, H. Heinke, K. Ohkawa, D. Hommel, H. Selke, F. Gindele, and U. Woggon, *CdSe/ZnSe quantum structures grown by migration enhanced epitaxy: Structural and optical investigations*, Appl. Phys. Lett. **71** (1997), 1510.

[LJLH00] K. Leosson, J. R. Jensen, W. Langbein, and J. M. Hvam, *Exciton localization and interface roughness in growth-interrupted GaAs/AlAs quantum wells*, Phys. Rev. B **61** (2000), 10322.

[LS91] H. J. Lozykowski and V. K. Shastri, *Excitonic and Raman properties of* $ZnSe/Zn_{1-X}Cd_XSe$ *strained-layer quantum wells*, J. App. Phys. **69** (1991), 3235–3242.

[Man00] C. Mann, *Vierwellen-mischen an II-VI halbleiter-nanostrukturen*, Diplom-Arbeit, Universität Dortmund, Experimentelle Physik IIb, September 2000.

[MBT+02] L. Marsal, L. Besombes, F. Tinjod, K. Kheng, A. Wasiela, B. Gilles, J.-L. Rouvière, and H. Mariette, *Zero-dimensional excitons in CdTe/ZnTe nanostrutures*, J. App. Phys. **91** (2002), 4936 – 4943.

[Med82] O. Medelung (ed.), *Landolt-Börnstein*, vol. 17b, Physics of II-VI and I-VII Compunds, Semimagnetic Semiconductors, Springer-Verlag, 1982.

[MMH96] A. Mecozzi, J. Mørk, and M. Hofmann, *Transient four-wave mixing with colinear pump and probe*, Opt. Lett. **21** (1996), 1017–1019.

[Möl00] Björn Möller, *Konstruktion einer mikro-positionereinheit und eines probenverschiebetisches zum einbau in einen kryostaten*, Hauptpraktikum, Universität Dortmund, Experimentelle Physik IIb, 2000.

[MZ04] E. A. Muljarov and R. Zimmermann, *Dephasing in quantum dots: Quadratic coupling to acoustic phonons*, Phys. Rev. Lett. **Submitted** (2004).

[NNK+95] M. Nirmal, D.J. Norris, M. Kuno, M.G. Bawendi, Al.L. Efros, and M. Rosen, *Observation of the "Dark exciton" in CdSe quantum dots*, Phys. Rev. Lett **75** (1995), 3728–3731.

[PKM93] Nasser Peyghambarian, Stephan W. Koch, and Andre Mysyrowicz, *Introduction to semiconductor optics*, Prentice Hall, New Jersey, 1993.

[PRWH99] J. Puls, M. Rabe, H. J-. Wünsche, and F. Henneberger, *Magneto-optical study of the exciton fine structure in self-assembled CdSe quantum dots*, Phys. Rev. B **60** (1999), R16303–306.

[PSE96] G. Massimo Palma, Kalle-Antti Suominen, and Artur K. Ekert, *Quantum computers and dissipation*, Proc. R. Soc. Lond. A **452** (1996), 567–584.

[PTVF92] W. H. Press, S. A. Teukolsky, W. T. Vetterling, and B. P. Flannery, *Numerical recipes in c: The art of scientific computing*, second ed., Cambridge University Press, 1992.

[PWG+04] P. Palinginis, H. Wang, S. V. Goupalov, D. S. Citrin, M. Dobrowolska, and J. K. Furdyna, *Exciton dephasing in self-assembled CdSe quantum dots*, Phys. Rev. B **70** (2004), 73302.

[RRA+88] M. A. Reed, J. N. Randall, R. J. Aggarwal, R. J. Matyi, T. M. Moore, and A. E. Wetsel, *Observation of discrete electronic states in a zero-dimensional semiconductor nanostructure*, Phys. Rev. Lett. **60** (1988), 535.

[Sch00] S. Schneider, *Aufbau eines hochauflösenden abbildenden spektrometers*, Hauptpraktikum, Universität Dortmund, Experimentelle Physik IIb, 2000.

[Sha96] J. Shah, *Ultrafast spectroscopy of semiconductors and semiconductor nanostructures*, Springer, Berlin, 1996.

[SLS$^+$01] T. H. Stievater, X. Li, D. G. Steel, D. Gammon, D. S. Katzer, D. Park, C. Piermarocchi, and L. Sham, *Rabi oscillations of excitons in single quantum dots*, Phys. Rev. Lett. **87** (2001), 133603.

[SLS$^+$02] T. H. Stievater, Xiaoqin Li, D. G. Steel, D. Gammon, D. S. Katzer, and D. Park, *Transient nonlinear spectroscopy of excitons and biexcitons in single quantum dots*, Phys. Rev. B **65** (2002), 205319.

[SSPY02] C. Santori, G. S. Solomon, M. Pelton, and Y. Yamamoto, *Time-resolved spectroscopy of multiexcitonic decay in an InAs quantum dot*, Phys. Rev. B **65** (2002), 73310.

[Sug99] Mitsuru Sugawara (ed.), *Self-assembled InGaAs/GaAs quantum dots*, Academic Press, 1999.

[SWB$^+$00] J. Seufert, R. Weigand, G Bacher, T. Kümmell, A. Forchel, K. Leonardi, and D. Hommel, *Spectral diffusion of the exciton transition in a single self-organized quantum dot*, App. Phys. Lett. **76** (2000), 1872 – 1874.

[SWF$^+$02] K. T. Shimizu, W. K. Woo, B. R. Fisher, H. J. Eisler, and M. G. Bawendi, *Surface-enhanced emission from single semiconductor nanocrystals*, Phys. Rev. Lett. **89** (2002), 117401.

[TFHL$^+$01] T. T. Flissikowski, A. Hundt, M. Lowisch, M. Rabe, and F. Henneberger, *Photon beats from a single semiconductor quantum dot*, Phys. Rev. Lett. **86** (2001), 3172–3175.

[TRH$^+$01] V. Türck, S. Rodt, R. Heitz, O. Stier, M. Strassburg, U. W. Pohl, and D. Bimberg, *Charged excitons and biexcitons in self-organised cdse quantum dots*, Phys. Stat. Sol. **224** (2001), 217–221.

[TRS$^+$00] V. Türck, S. Rodt, O. Stier, R. Heitz, R. Engelhardt, U. W. Pohl, D. Bimberg, and R. Steingrüber, *Effect of random field fluctuations on excitonic transitions of individual CdSe quantum dots*, Phys. Rev. B **61** (2000), 9944–9947.

[UMK$^+$04] B. Urbaszek, E. J. McGhee, M. Krüger, R. J. Warburton, K. Karrai, T. Amand, B. D. Gerardot, P. M. Petroff, and J. M. Garcia, *Temperature-dependent linewidth of charged excitons in semiconductor quantum dots: Strongly broadened ground state transitions due to acoustic phonon scattering*, Phys. Rev. B **69** (2004), 35304.

[WGWK96] U. Woggon, F. Gindele, O. Wind, and C. Klingshirn, *Exchange interaction and phonon confinement in CdSe quantum dots*, Phys. Rev. B **54** (1996), 1506–1509.

[Wog97] Ulrike Woggon, *Optical properties of semiconductor quantum dots*, Springer Verlag, 1997.

[Yof01] A. D. Yoffe, *Semiconductor quantum dots and related systems: electronic, optical, luminescence and related properties of low dimensional systems*, Advances in Physics **50** (2001), 1–208.

[ZM04] Roland Zimmermann and Egor Muljarov, *Dephasing of optical transitions in quantum dots - where exact solutions meet sophisticated experiments*, 12th Int. Symp. “Nanostructures: Physics and Technology” St Petersburg, Russia, June 21-25 2004.

[ZR02] R. Zimmermann and E. Runge, *Dephasing in quantum dots via electron-phonon interaction*, Proceedings of the 26th International Conference on the Physics of Semiconductors (UK) (J. H. Davies and A. R. Long, eds.), Institute of Physics Publishing, 2002, p. to appear.

Symbols and abbreviations

symbol	**meaning**
a_B	exciton Bohr radius
$a_\mathbf{q}, a_\mathbf{q}^\dagger$	creation, annihilation operator for phonon with wavevector $\mathbf{q}$
AOM	acousto-optic modulator
$B_J, B_J^\dagger$	creation, annihilation operator for exciton
c	speed of light in vacuum (299 792 458 m s^{-1})
C_{ij}	correlation coefficient between states i and j
CCD	charge coupled device
CW	continuous wave (excitation)
$\delta(t)$	Dirac delta function
δ_0	bright-dark state splitting energy
δ_1	bright-state anisotropy splitting energy
δ_e	escape energy
Δ	split-off energy
Δ_{ij}	components of interaction Hamiltonian
d	distance
$D_{c,v}$	deformation potential of conduction,valence bands
$D_{nD}(E)$	density of states, n-dimensional case
$\mathcal{E}$	electric field
e	unit charge (1.602176 $\cdot 10^{-19}$ C)
ϵ	relative dielectric constant
ϵ_0	static dielectric constant
η	detuning
E_b	binding energy
E_{Ex}	excitonic energy level
E_g	gap energy
E_i	transition energy of i^{th} state
EID	excitation-induced dephasing
eV	electron volt (1.602176 $\cdot 10^{-19}$ J)

f	focal length of lens
$\mathbf{F}$	local electric field
FPD	free-polarisation decay
FWHM	full width at half maximum
FWM	four-wave mixing
fs	femtosecond
γ	(monoexponential) decay rate
γ_0	spin-relaxation rate
γ_e	escape rate
γ_r	radiative recombination rate
Γ	phenomenological decay rate
Γ_h	homogeneously broadened linewidth
H	Hamilton operator
H_0	Hamilton operator for isolated system
H_{int}	interaction Hamiltonian
H_R	relaxation Hamiltonian
$\hbar$	$h/2\pi$= 1.054571$\cdot$ 10^{-34} J s= 6.582118$\cdot$ 10^{-16} eV s
HFWM	heterodyne four-wave mixing
HWHM	half width at half maximum
I	intensity
I_0	reference (excitation) intensity
i	integer index $i = 0, 1, 2\ldots$
$\mathbf{J}$	total angular momentum
j_z	z-component of the total angular momentum
$\mathbf{k}$	momentum vector
$k^{\|\|}$	in-plane momentum
k_x, k_y	x, (y) component of the in-plane momentum $k_{\|\|}$
κ	imaginary part of the refractive index (extinction coefficient)
$\mathbf{K_i}$	reciprocal lattice vector
λ	wavelength
$\mathbf{L}$	orbital angular momentum
L_x	characteristic dimension along x
μ	effective reduced mass of exciton
$\mu-$	(prefix) micro ($\times 10^{-6}$)
μPL	micro-photoluminescence
m_0	electron mass ($9.109381 \cdot 10^{-31}$ kg)
m_e	effective electron mass
$m_h h$	effective heavy-hole mass

m_h	effective light-hole mass
m^*	effective mass
$M_{\mathbf{q}}^{lj}$	phonon mediated coupling matrix
MBE	molecular beam epitaxy
ML	monolayer
MOCVD	metal-organic chemical vapour deposition
$\widetilde{n}$	complex refractive index
n	real part of the refractive index, population of ensemble
$n_{b,d}$	population of the (bright,dark) state
N_D	volume density of dots
$N_{\mathbf{q}}$	Bose distribution of phonons
NA	numerical aperture
nm	nanometre
ns	nanosecond
ω_0	centre-frequency (of transition,laser excitation)
Ω_R	Rabi frequency
ω_{RF}	radio-frequency at which AOM is driven
p	polarisation of ensemble
$\mathbf{p_i}$	permanent dipole moment of i^{th} state
P_i	polarisibility tensor of i^{th} state, fraction of system in state i
$\mathbf{p}_{ij}$	dipole moment of states i, j
$P(t)$	polarisation
$\phi(\mathbf{r})$	radial component of wavefunction
PC	personal computer
PL	photoluminescence
ps	picosecond
$\mathbf{q}$	phonon wavevector
QCSE	quantum-confined Stark effect
QD	quantum dot
QW	quantum well
ρ	density matrix operator
$\rho_{e,h}$	charge density of electrons,holes
ρ_m	mass density
$\mathbf{R}$	Bloch vector
$\mathbf{S}$	spin angular momentum
S	Huang-Rhys factor
T	temperature
T_1	population lifetime

T_2	dephasing time
T_2'	pure dephasing time
τ	delay time
Θ	Heaviside step function, pulse area
θ_B	Bragg angle
v_P	phase velocity
v_g	group velocity
σ	standard deviation
σ_G	Gaussion width
$\mathbf{s}$	velocity of sound
T	trion (singly charged exciton)
X	exciton
XX	biexciton
ZPL	zero-phonon line

Acknowledgements

This work would not have been possible without the help of many people, and so I will try to avoid being too effusive over any one person. Prof. Dr. Ulrike Woggon, as head of the group, my supervisor, and the first referee for my examination provided an atmosphere uniquely conducive to productive research and I am indebted to her. Likewise, the energy and skill which Priv.-Doz. Dr. Wolfgang Langbein brought to the endeavours described here made it an honour and a privilege to experience his tutelige. His ideas and guidance were the basis for much of this work.

On both a professional and personal level, it has been a pleasure working with Priv.-Doz. Dr. Paola Borri. I wish her much success in the future. Drs. Gerrit Kocherscheidt and Stephan Schneider both eased my transition to Germany and guided me through the many culture shocks involved. I hope I can return the favour some day!

To all the other members of EIIa and EIIb, I would like to express my gratitude for making my time here fly by. It has been a memorable experience! The technical and administrative staff of the university are also thanked for their contributions.

I cordially acknowledge Prof. Dr. Dietmar Fröhlich for agreeing to referee this work. In a similar vein, I thank Prof. Dr. Manfred Bayer, Dr. Giorgio Baldassarri and Andrew Corrigan for proof-reading this text, sometimes many times over! Naturally, *mea culpa* should any mistakes remain.

Moving to another country is never easy, let alone completing a PhD, and without the support of my parents and family it would have been even more difficult. Reena Badiani was also the graceful recipient of many incredulous calls as I found my feet here. And I think that if Vera Dennes never hears the phrase “I’m writing my thesis” again it will still be one time too many.

Thank you all - I hope I’ve done you proud.